Cardiac Remodeling Of Conduction, Repolarization and Excitation-Contraction Coupling: From Animal Model to Failing Human Heart

Qing Lou
Washington University in St. Louis

Follow this and additional works at: https://openscholarship.wustl.edu/etd

WASHINGTON UNIVERSITY IN ST. LOUIS

School of Engineering and Applied Science

Department of Biomedical Engineering

Dissertation Examination Committee:
Igor R. Efimov, Chair
Martin Arthur
Philip Bayly
Jianmin Cui
Daniel Moran
Richard Schuessler
Frank Yin

Cardiac Remodeling Of Conduction, Repolarization and Excitation-Contraction Coupling:

From Animal Model to Failing Human Heart

by

Qing Lou

A dissertation presented to the
Graduate School of Arts and Sciences
of Washington University in
partial fulfillment of the
requirements for the degree
of Doctor of Philosophy

August 2011
Saint Louis, Missouri

Abstract

Heart failure is one of the leading causes of death worldwide, with rising impact with the increasing ageing population. This is in sharp contrast with the limited and non-ideal therapies available. Approximately 50% of deaths from heart failure are sudden and unexpected, and presumably the consequence of lethal ventricular arrhythmias. Despite significant reduction of mortality from sudden cardiac death achieved by ICDs and drugs such as beta-blockers, there remains a large room for improving the survivability of heart failure patients by advancing our understanding of arrhythmogenesis from molecular level to multi-cellular tissue level. Another important aspect of heart failure is abnormal excitation-contraction (EC) coupling and calcium handling, functional changes of which exert great impact on both arrhythmia vulnerability and pump failure. Advancing the understanding the remodeling of EC coupling and calcium handling might provide potential molecular and anatomical targets for clinical intervention.

In this dissertation, I first developed two optical imaging systems (both hardware and software) for quantifying the conduction, repolarization and excitation-contraction coupling. The first one is the panoramic imaging system for mapping the entire ventricular epicardium of a rabbit heart. The second one is the dual imaging system for simultaneous measurement of action potential and calcium transient.

Using the systems I developed, I conducted two rabbit studies to investigate the role electrical instability and structural heterogeneity in the induction and maintenance of arrhythmias. We first identified the importance of both dynamic instability and effective

tissue size in the spontaneous termination of arrhythmia in the normal rabbit heart. We then identified novel mechanism of how healed myocardial infarction promotes the induction of ventricular arrhythmia.

Finally, guided by the knowledge from the animal studies, I studied the failing human heart with the aim to advance our understanding of cardiac electrophysiology in human heart failure. We first demonstrated the transmural heterogeneity of EC coupling in nonfailing heart and identified potential mechanisms of electrical and mechanical dysfunction by quantifying the remodeling of EC coupling. We then studied the remodeling of conduction and repolarization with the aim to determine of the role of dispersion of repolarization and electrical instability in the induction of arrhythmia in human heart failure.

Acknowledgements

First and foremost, I want to thank my advisor Dr. Igor R. Efimov. The last five years was a bumpy journey for me, but he kept faith in me, and guided me through with a tremendous amount of patience and encouragement. His confidence in me is the backbone of this dissertation. I also benefited from his nurturing of my scientific passion and from his caring of my career development. His scientific sensitivity and vision are top-notch and I will be fortunate if I have inherited some of them to serve the rest of my scientific career.

I am lucky to have some greatest teachers in the lab. I would like to thank Dr. Crystal Ripplinger for getting me started in the lab and unreservedly teaching me how to do my first rabbit experiment. I want to thank Dr. Vadim Fedorov for implanting the rigorous mindset in me for doing experiments. I also want to thank our lab manager Dr. Aili Cai for teaching all the molecular biology skills.

I would also like to thank all my lab mates and fellow graduate students for their support and kindness in the past several years. I'd like to thank Dr. Alexey Glukhov and Dr. Deborah Janks for their irreplaceable support in so many experiments together. I want to especially thank Wenwen Li and Christina Ambrosi, who joined the lab at the same year as I did and helped me in many ways indescribable.

I would like to thank my committee members Dr. Jianmin Cui, Dr. Richard Schuessler, Dr. Philip Bayly, Dr. Daniel Moran, Dr. Martin Arthur, and Dr. Frank Yin for their valuable inputs. I want to especially thank Dr. Cui as my academic advisor for his support. I would like to acknowledge the National Institute of Health (grant HL085369, HL067322, and HL074283) for funding my thesis projects.

Finally, I would like to dedicate this dissertation to my beloved wife Ning Jin, for being strong and supportive in the long-distance relationship and being the motivation of my life, and to my parents, for their relentless and unconditional love and support no matter how far I am away from home.

Contents

Abbreviations

$[Ca^{2+}]_i$	Intracellular calcium concentration
AC	Adenylyl cyclase
AP	Action potential
APD	Action potential duration
APD80	Action potential duration at 80 repolarization
ATP	Adenosine triphosphate
BCL	Basic cycle length
BDM	2,3-butanedione monoxime
bpm	Beats per minute
CAMKII	Ca^{2+}/calmodulin-dependent protein kinase II
cAMP	Cyclic adenosine monophosphate
CaT	Calcium transient
CaTD	Calcium transient duration
CaTD80	Calcium transient duration at 80% relaxation
CICR	Calcium induced calcium release
CL	Cycle length
CRT	Cardiac resynchronization therapy
CV	Conduction velocity
DI	Diastolic interval
DMSO	Dimethylsulfoxide
EC	Excitation contraction

ENDO	Endocardium
EPI	Epicardium
FFR	Force frequency relationship
FOV	Field of view
HF	Heart failure
I-1	Phosphotase inhibitor 1
Ica	Calcium current
IK1	Inward rectifier K+ current
Ikr	Fast delayed rectifying K+ current
Iks	Slow delayed rectifying K+ current
$I$to	Transient outward K+ current
LAD	Left anterior descending coronary artery
LV	Left ventricle
LVAD	Left ventricular assist device
MAP	Monophasic action potential
MI	Myocardial infarction
MID	midmyocardium
NCX	Sodium/calcium exchanger
PDA	Photo-diode array
PDE4D	Phosphodiesterase 4D
PKA	Protein kinase A
PKC	Protein kinase C
PLN	Phospholamban

PP1	Protein Phosphotase 1
PP2A	Protein phosphotase 2A
PS	Phase singularity
RV	Right ventricle
RyR	Ryanodine receptor
SERCA	sarcoplasmic reticulum calcium ATPase
SHD	Structural heart disease
SHR	Spontaneous hypertensive rat
SR	Sarcoplasmic reticulum
T-tubule	Transerve tubule
VEP	Virtual electrode polarization
WB	Western blotting

1. Introduction

1.1 Background and Motivation

Heart failure is one of the leading causes of death worldwide. It claims over 250,000 lives annually in the United States alone (2). Despite great basic and clinical research efforts and advances, the available therapies for heart failure remain limited and not ideal. This is largely due to the complex nature of the disease and difficulties in translating the knowledge from animal studies to patients with heart failure. It is therefore important to continue advancing our understanding of the underlying mechanisms leading to electrical and mechanical dysfunction in both animal models and heart failure patients for the development of device-based and molecular therapies.

There are two important intertwined areas of research in heart failure. One area is the study of ventricular arrhythmia, which is responsible for the sudden cardiac death that accounts for approximately 50% of deaths from heart failure. Despite the significant reduction of mortality achieved by ICDs and non-antiarrhythmic drugs such as beta-blockers, it remains a big challenge to reverse the prognosis and cure the disease. A better understanding of the arrhythmic mechanism will help early diagnosis, target identification of intervention and hopefully lead to therapies that completely eliminate the trigger and substrate of the lethal ventricular arrhythmia.

Another important aspect of heart failure is the impaired excitation-contraction (EC) coupling and calcium handling, abnormal remodeling of which enhances both arrhythmia

vulnerability and pump failure. Molecular therapies targeting the key EC coupling proteins are under intensive basic and clinical investigation and might become an attractive therapeutic alternative in the near future. On the other hand, clinical translation is limited by our incomplete understanding of the molecular and functional remodeling of EC coupling in heart failure.

Basic studies of heart failure using animal models allow detailed and controlled mechanistic investigations of cardiac electrical and mechanical dysfunction. However, direct extrapolation of animal model results to patients are complicated not only by the great variations in normal cardiac electrophysiology in animal species, but also by the array of heart failure models used (including ischemic, pacing-induced, toxin-induced, genetic modification, pressure overload, and volume overload models). Therefore, any hypotheses derived from the animal models should be tested directly in human heart.

1.2 Scope and Outline of the Dissertation

In this dissertation, we aimed to first develop advanced optical imaging systems for the functional studies of cardiac electrophysiology, then to explore the role of conduction, repolarization, and EC coupling in the rabbits, and finally to test the obtained hypothesis directly in the humans with and without heart failure.

Chapter 2 will describe the development of panoramic optical imaging system. The dual optical imaging system will be briefly described in the Appendix B. Chapter 3 will present my first rabbit study exploring the mechanisms of arrhythmia maintenance and self-termination. Chapter 4 describes my second rabbit study exploring the arrhythmogenesis in the presence of healed myocardial infarction. Chapter 5 is a description of a human study to test the

hypothesis obtained from my animal studies in human heart failure. Before further experimental data are presented, Chapter 6 provides an overview of the remodeling of calcium handling in human heart failure. Afterwards, a study of EC coupling remodeling in failing human heart is presented in Chapter 7. Finally, summary and future direction are presented in Chapter 8.

2. Quantitative Panoramic Imaging of Epicardial Electrical Activity

2.1 Abstract

Fluorescent imaging with voltage- and/or calcium-sensitive dyes has revolutionized cardiac physiology research. Here we present improved panoramic imaging for optically mapping electrical activity from the entire epicardium of the Langendorff-perfused rabbit heart. Combined with reconstruction of the 3D heart surface, the functional data can be conveniently visualized on the realistic heart geometry. Methods to quantify the panoramic data set are introduced by first describing a simple approach to mesh the heart in regular grid form. The regular grid mesh provides substrate for easy translation of previously available non-linear dynamics methods for 2D array data. It also simplifies the unwrapping of curved three-dimensional surface to 2D surface for global epicardial visualization of the functional data. The translated quantification methods include activation maps (isochrones), phase maps, phase singularity and electric stimulus induced virtual electrode polarization (VEP) maps. We also adapt a method to calculate the conduction velocities on the global epicardial surface by taking the curvature of the heart surface into account.

2.2 Introduction

Transmembrane potential on the epicardial surface of the heart can be recorded optically (178). To maximize the field of view, panoramic optical imaging was introduced by Lin et al. (151) to map the entire ventricular epicardium from three different angles around the heart. Later, more efforts were devoted to this novel imaging methodology. Bray et al. (28)

proposed to reconstruct the heart geometry and texture map the optical signal onto the geometric surface for better visualization. Kay et al. (124) implemented panoramic optical mapping on swine hearts, and Rogers et al. (223, 224) applied this technology in research of ventricular fibrillation. More recently, our group (213) developed a panoramic imaging system using three photo-diode arrays (PDAs, Hamamatsu) with high temporal resolution for research on mechanisms of cardiac defibrillation. A sketch of this system is shown in Appendix A.

While panoramic imaging systems are being improved, the data analysis methods designed for panoramic data sets are still limited. One reason is that the available analysis tools do not easily lend themselves to the unstructured triangular mesh of the heart surface geometry. In this study, we employed a way to mesh the heart surface for translation of some common 2D analysis methods. Additionally, conduction velocity vector fields were estimated from the panoramic data set for the first time.

2.3 Methods

2.3.1 Optical Mapping Experiments

The panoramic optical mapping system and Langendorff-perfused rabbit heart have been described previously (213). Briefly, three photo-diode arrays facing the heart were spaced 120° apart in the perfusion chamber. Light emitting diode arrays were used as excitation light source for the voltage-sensitive dye. This system provides high temporal resolution (5000 frames/s) and sufficient spatial resolution (1.72mm without interpolation). The excitation-contraction uncoupler blebbistatin (75) was used to suppress motion artifacts during optical recording. Thirty-six images of the heart were taken every 10° as the heart was rotated a full

360° at the end of the experiments for geometric reconstruction. Optical signals were registered with and texture-mapped onto the surface of the reconstructed geometry.
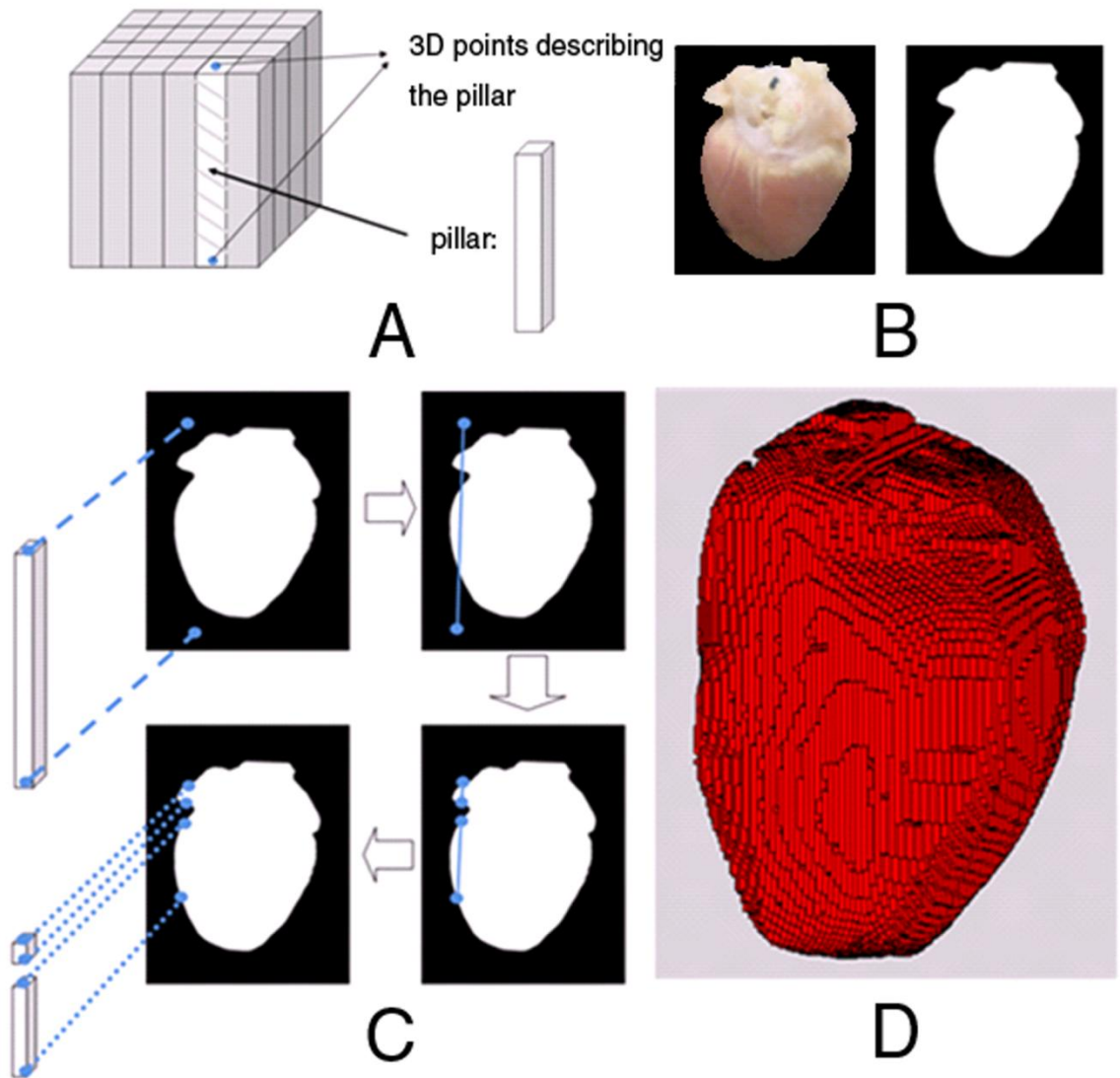
Figure 1. Reconstruction of heart geometry. (A) Pillars used as the building block for the geometry. (B) Digital image of the heart and silhouette image. (C) Refinement of the pillars using the silhouette image. First the two end points of pillars were projected onto the images. The projections were then connected by a line which might intersect with the contour of the heart. The portions outside the contour were cropped off. And the corresponding part of the pillar was also cropped off. (D) The final reconstructed geometry of one heart.

2.3.2 Geometry Reconstruction and Registration

The geometry of the rabbit heart was reconstructed through thirty-six digital images of the heart using Niem's method(192). The procedures are illustrated in Fig. 1. A volume cube composed of pillar elements (Fig. 1A) was used as the first crude model of the heart for further refinement. The individual pillar was then projected consecutively into the digital images and tested for intersections with the object silhouettes (Fig. 1C). The part whose projection was outside the object silhouettes was carved off. By refining the volume cube with all the silhouettes in digital images, the geometry of the heart is reconstructed with sufficient details (Fig. 1D).
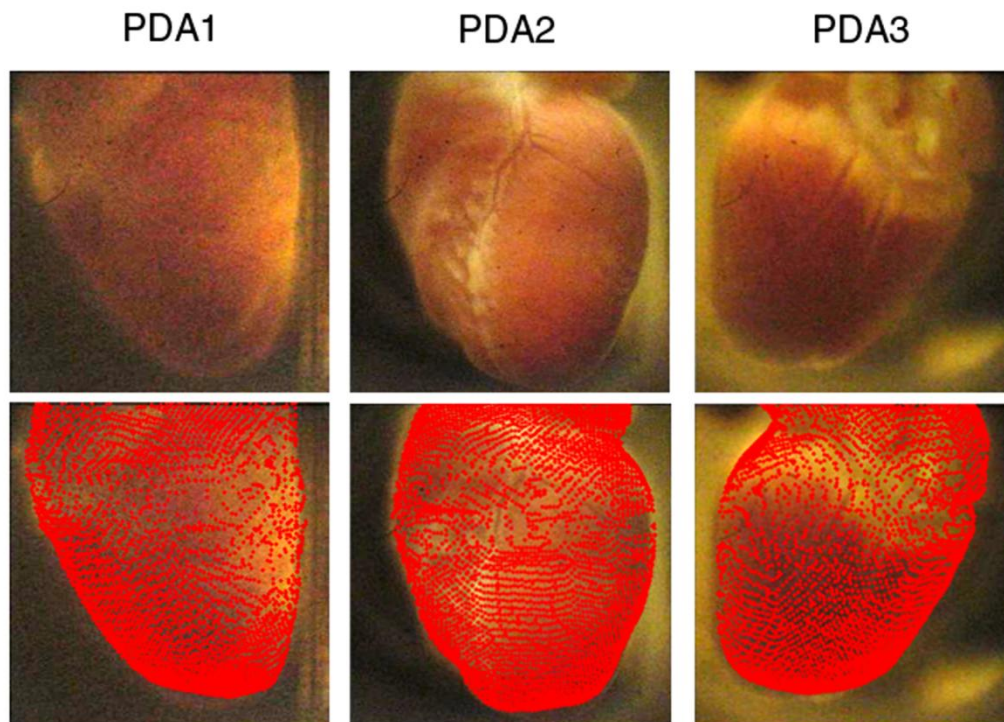
Figure 2. Registration of the recorded fluorescent signal with the reconstructed geometric surface. The images in the first row are digital images of the heart at the image plane of the PDAs. Red dots in second-row images are projections of the surface points of reconstructed geometry of the heart. Good registrations were reached when the shape of projections match and overlap the heart in the digital images.

The registration of the signal with the geometric surface is accomplished by first projecting the reconstructed geometry onto the image plane of every PDA and then matching the projection with region of the heart "seen" by every PDA. Before each optical mapping study, a frosted glass was placed in the same location of image plane of every PDA and a digital image of the frosted glass was acquired. From these images the heart region for optical mapping from individual PDA was determined. Good registration is achieved when the projection (red dots in Fig. 2) perfectly matches the heart regions in the image plane of PDAs.

2.3.3 Unwrapping Heart Surface into 2D Map

Taking an approach similar to those used in cartography, the surface of the heart was "unwrapped" into a 2D flat map. This allows (1) global visualization of the data in a flat plane and (145) the direct utilization of well-established 2D analysis methods, such as isochronal mapping, estimation of conduction velocity vectors, and phase mapping.

The starting point of the unwrapping procedure is the identification of a large number of points (Fig. 3A) lying on the surface of the heart geometry; the coordinates of these points are obtained from geometric reconstruction described in the previous section. The geometrical center of the heart is found by averaging the coordinates of all the heart surface points. Then the "longitude and latitude" of each point are calculated by transforming the Cartesian coordinates (x, y, z) to spherical coordinates (θ, φ, r), where θ, φ are the counterparts of longitude and latitude in the case of earth, and r is the distance between that point and the geometric center of the heart. The magnitude of r is represented by color in Fig. 3B. By redrawing every point in the θ - φ plane, we unwrap the heart surface into a two-dimensional "map". Again, the color of each point in Fig. 3C represents the magnitude of r.

8
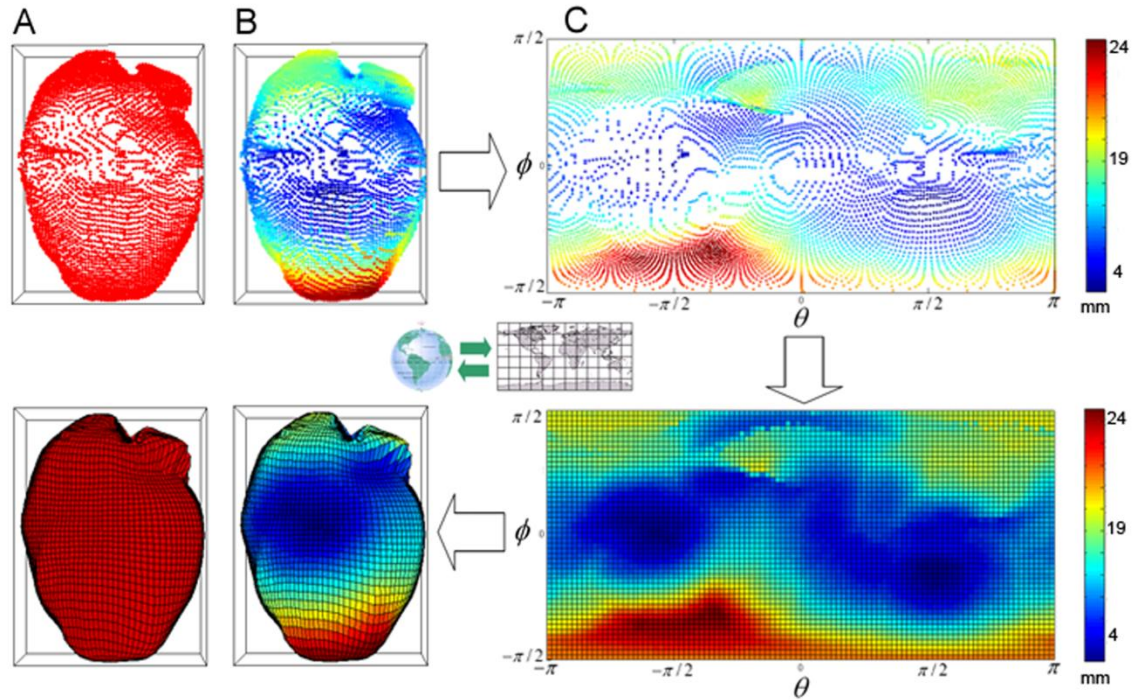
Figure 3. Meshing the heart surface. (A) Surface points obtained from geometric 3D reconstruction from multiple views. (B) Surface points coded with color which represents the distance to the geometric center of the heart. (C) Surface points unwrapped onto the (θ, φ) plane. (D) Linear interpolation of surface points into an evenly spaced (θ, φ) grid. (E) Meshed surface wrapped from interpolated grid. (F) Completed meshed surface.

We then define an evenly spaced (θ, φ) grid, and interpolate **r** on this grid (Fig. 3D). Each grid element corresponds to a specific (θ, φ) pair. This procedure creates a 2D-grid representation of the heart surface which is compatible with many available data analysis tools. By connecting points with the same θ, and also points with the same φ in 3D space, we can generate a mesh (Figs. 3E&F) with lines mimicking the longitudes and latitudes in the Earth globe.

The resultant (θ, φ) plane is the 2D representation of the originally curved and topologically closed 3D surface. While it is a distorted representation of the curved heart surface, it provides an alternative way to visualize the epicardial activation, especially for

9

global visualization without the necessity of rotating the heart. More importantly, it transforms the data structure into grid form so that common 2D analysis methods can be easily applied. Furthermore, if correlation between electrical activity and anatomical features is essential, we can also texture-map the anatomy onto the (θ, φ) plane.

2.3.4 Translate Data Analysis Methods

A variety of techniques to visualize and analyze the data were implemented, including maps of transmembrane voltage (V), dV/dt, phase, phase singularities, activation times, conduction velocity, and electric stimulus induced VEP. Fluorescent signals were recorded from the PDAs. The signals were first normalized and then interpolated before being texture-mapped onto the surface.

Phase map is a unique tool for arrhythmic activity. It is based on phase plane analysis and facilitates visualization of wave fronts and wave breaks. Phase can be obtained using the method proposed by Bray et al. (29). Briefly, the phase $\psi(\theta,\varphi,t)$ is obtained by

$$\psi(\theta,\varphi,t) = \arctan \frac{V'(\theta,\varphi,t)}{H[V'(\theta,\varphi,t)]} \ ,$$

where $V'(\theta,\varphi,t)$ is the transmembrane voltage processed by the proper orthogonal decomposition, and $H[V'(\theta,\varphi,t)]$ is the Hilbert transform of $V'(\theta,\varphi,t)$ and represents a signal with a $\pi/2$ phase lag relative to $V'(\theta,\varphi,t)$.

Rotors or wave breaks during cardiac fibrillation correspond to the phase singularities in the phase map. The calculation of phase singularity was implemented based on the method

described by Bray et al. (31). Briefly, the gradient of phase was first calculated along two dimensions of the θ - φ grid,

$$\nabla \psi_\theta[m,n] = \psi[m+1,n] - \psi[m,n];$$
$$\nabla \psi_\varphi[m,n] = \psi[m,n+1] - \psi[m,n];$$

Topological charge is then calculated using convolution between the gradients and 3×3 kernel which mimic the line integral of phase gradients along a closed curve surrounding a point. That is,

$$\nabla \psi_\theta \otimes \nabla_\theta + \nabla \psi_\varphi \otimes \nabla_\varphi \text{ where } \nabla_\theta = \begin{bmatrix} 0 & 0 & 0 \\ -1 & 0 & 1 \\ -1 & 0 & 1 \end{bmatrix}, \nabla_\varphi = \begin{bmatrix} 0 & 1 & 1 \\ 0 & 0 & 0 \\ 0 & -1 & -1 \end{bmatrix}. \text{ A point is recognized}$$

as a phase singularity if its topological charge is 2π or -2π.

Activation time was obtained using $\left(dV(\theta,\varphi,t)/dt \right)_{max}$, from which the isochrones were generated.

All the methods described in this section can be first implemented in the (θ, φ) plane, and then wrapped back onto the 3D heart surface. It should be noted that we cannot directly apply this procedure to calculate the conduction velocity because distance is distorted in the (θ, φ) plane.

2.3.5 Conduction Velocity on the 3D Surface

Conduction velocity is an important parameter in determining the heart's susceptibility to arrhythmia. With the knowledge of the epicardial geometry, we are able to quantify conduction velocity on the whole heart surface.

One approach to calculate the conduction velocity in a 2D (*x-y*) plane has been proposed

by Bayly et al. (11) Since the heart surface is essentially three dimensional, this method

cannot be directly applied. We adapted this method and extended its usage in our panoramic

data set. First, we define the activation time *t* as a function of θ and φ like

$t(\theta,\varphi) = a\theta^2 + b\varphi^2 + c\theta\varphi + d\theta + e\varphi + f$, where θ and φ are spherical coordinates and has

been calculated when we mesh the heart. Coefficients *a,b,…,f* are obtained by polynomial

fitting using (*t, θ, φ*) in the pre-defined time and space windows. $\partial t/\partial\theta$ and $\partial t/\partial\varphi$ can then be

calculated. The gradient of *t* is determined using $\nabla t = \frac{1}{r\sin\varphi}\hat{\theta}\frac{\partial t}{\partial\theta} + \frac{1}{r}\hat{\varphi}\frac{\partial t}{\partial\varphi} + \hat{r}\frac{\partial t}{\partial r}$. Since

∇ *t* is zero along the direction normal to the surface, its projection on the direction normal

to the surface should be equal to zero, that is,

$$\left(\frac{1}{r\sin\varphi}\hat{\theta}\frac{\partial t}{\partial\theta} + \frac{1}{r}\hat{\varphi}\frac{\partial t}{\partial\varphi} + \hat{r}\frac{\partial t}{\partial r}\right)\cdot\hat{e}_n = 0 \ldots\ldots\ldots\ldots(1)$$

where $\hat{e}_n$ is the unit vector normal to the surface, and $\hat{\theta}$ $\hat{\varphi}$ $\hat{r}$ are unit vectors in

spherical coordinates. Since we know $\partial t/\partial\theta$ and $\partial t/\partial\varphi$, we can get $\partial t/\partial r$ by solving equation

(1).

We then define two orthogonal axes, x and y, which are tangent to the surface; and

calculate $\partial t/\partial x$ and $\partial t/\partial y$ by $\frac{\partial t}{\partial r}\frac{\partial r}{\partial x}$ and $\frac{\partial t}{\partial r}\frac{\partial r}{\partial y}$. $\partial t/\partial x$ and $\partial t/\partial y$ fully represent ∇ *t* because

∇ *t* is tangent to the surface. Finally we can calculate the conduction velocity (CV) using

$$CV = \left[\frac{dx}{dt}, \frac{dy}{dt}\right] = \left[\frac{t_x}{t_x^2 + t_y^2}, \frac{t_y}{t_x^2 + t_y^2}\right], \text{ where } t_x = \frac{\partial t}{\partial x} \text{ and } t_y = \frac{\partial t}{\partial y}.$$

Simulations were performed to test the accuracy of this method on a meshed sphere which mimics the geometry of the heart. The mesh density of the sphere is set to be close to that of the reconstructed heart surface. A propagating wave is initiated from one surface point of the sphere, and radially propagates out on the surface at constant speed (Fig. 4A). The propagating wave with square cross sections was generated by the function

$f(x,y,z,t) = sign(\sin(wt - k_r r))$, where r is the surface distance away from the wave initiation site. The surface distance is the shortest distance between two points on the surface. The exact speed of propagation is w/k_r. The performance of this method was tested by calculating the deviation of the estimated from the exact propagation speed.
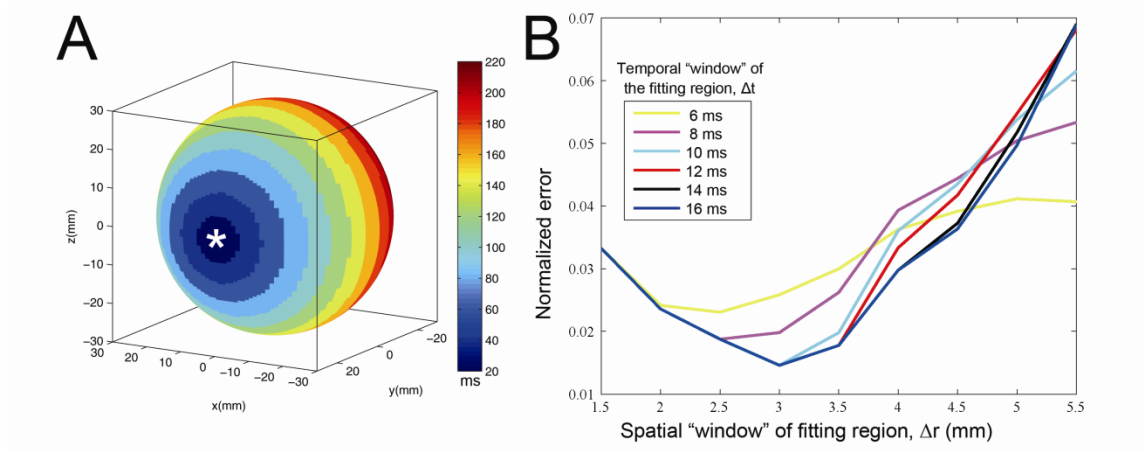
Figure 4. Simulation of pacing in a spherical surface. (A) Activation map in the sphere surface by point stimulation at the location noted by an asterisk. The wave propagates radially in a constant speed on the surface. (B) Dependence of the error of conduction velocity on the spatial and temporal "windows" of the fitting region. Suppose one active point, named as center point, is active at Ta. Other active points, which are active at Ti, are included in fitting if their distance from the center point is less than ⊿r, and |Ti-Ta| < ⊿t.

2.4 Results

2.4.1 Function Together with Anatomy

Figure 5 shows the unwrapped anatomy, transmembrane voltage (V), dV/dt, phase map, and phase singularity in the (θ, φ) plane. Figure 5A is the anatomy map, which is obtained by first texture mapping the digital images of anatomy onto the reconstructed geometric surface and then unwrapping it into a flat plane. This unwrapped anatomy provides a unique way to correlate the functional data to the anatomy. Figure 5B is a snapshot of transmembrane voltage 230ms after initiation of ventricular fibrillation. The value is normalized into - 85~15mV from the recorded fluorescent signal. Figure 5C is a snapshot of normalized dV/dt, where the largest values correspond to the wave fronts. Figure 5D is the phase map, with phase zero corresponding to the wave front. Figure 5E shows the distribution of phase singularities. Blue dots are the rotors of clockwise rotation of wavefront, while red dots are the rotors of counterclockwise rotation.

While the unwrapped view provides a global sense of wave propagation on the epicardium, data visualization on the reconstructed heart geometry provide an undistorted image of the electrical activation. It also allows for easy registration with the anatomy in the digital images at different angles. Figure 6 includes all the data presentations on the reconstructed geometry.

By mapping the whole ventricle, we are able to globally track the positions of phase singularities, which reveal the dynamics of the ventricular arrhythmia. The first image of Figure 7 shows the combined image of anatomy and trajectories of phase singularities during

a certain time period of self-terminated arrhythmia. The phase singularity starts from point A,

then travels to points B, C, D, and finally hits the AV boundary and terminates. The
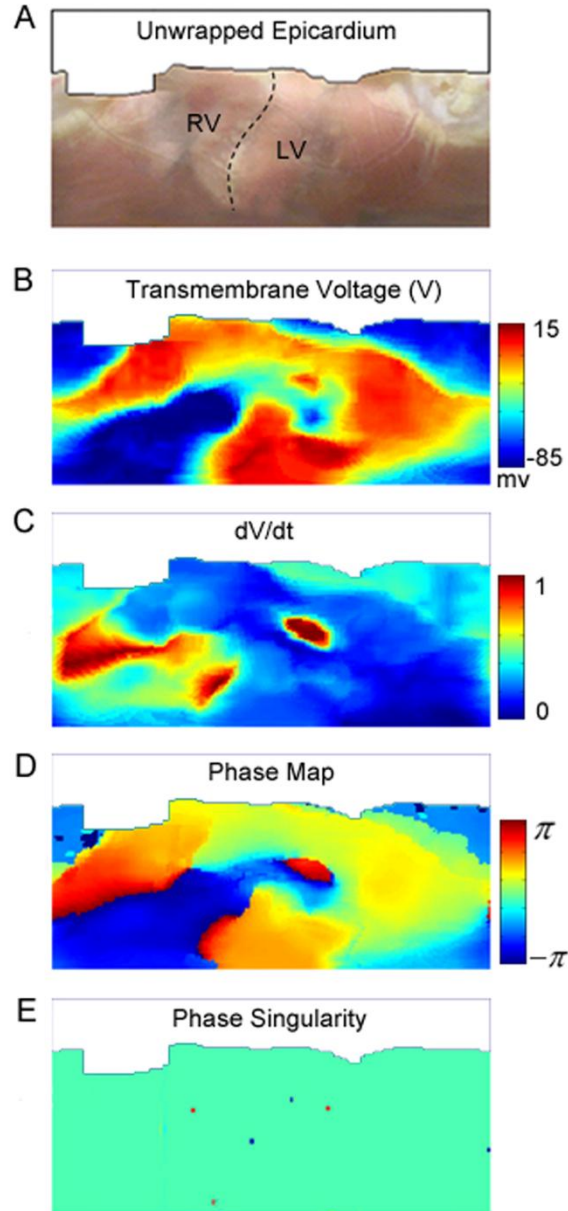
Figure 5. Unwrapped presentations. (A) Unwrapped epicardium obtained from digital photographs of the heart. The dashed line represents the septum. (B) Unwrapped epicardial transmembrane voltage (V) during ventricular fibrillation. The data is transformed to -85mV to 15mV range from normalized fluorescent signal. (C) Unwrapped dV/dt map with value normalized to 0~1. (D) Unwrapped phase map. (E) Phase singularities. Blue dots represent clockwise rotation while red dots represent counterclockwise rotation.
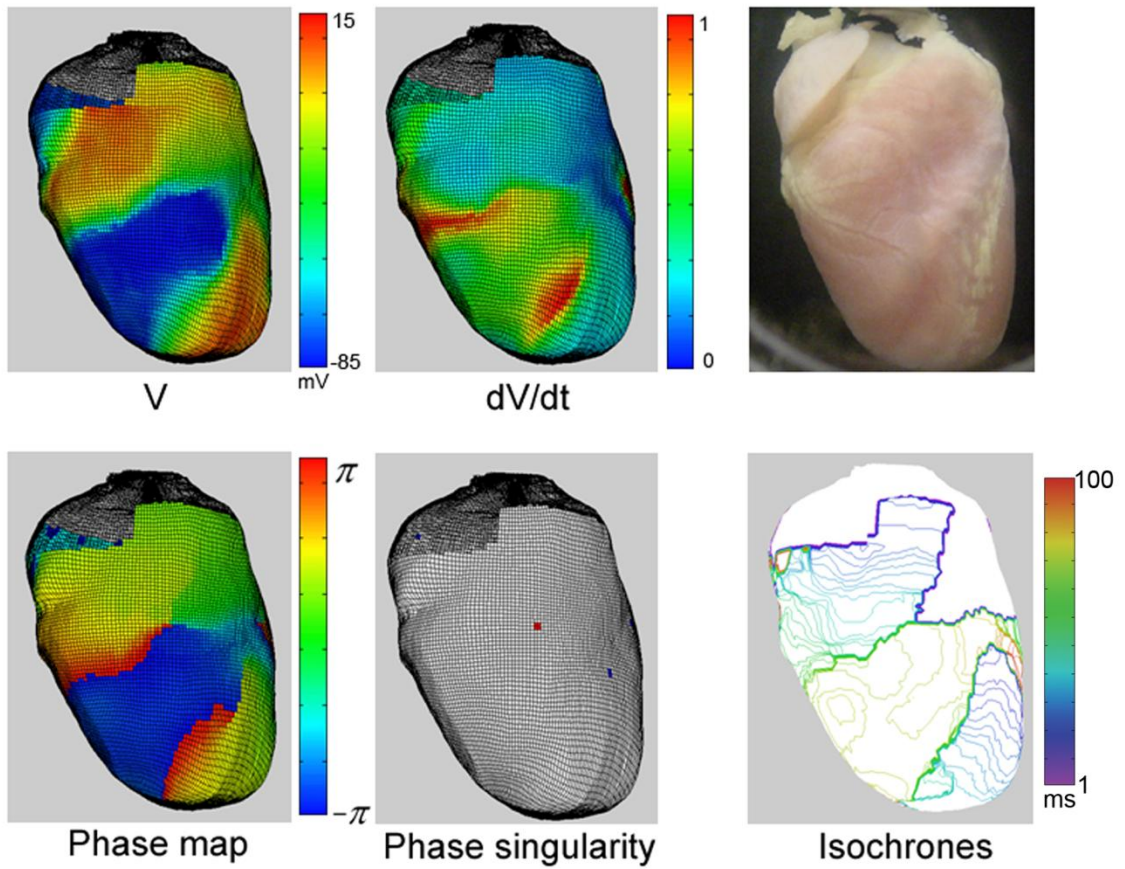
Figure 6. Wrapped presentations. Specific notations are present in the figure. The time interval of isochrones is 2ms.
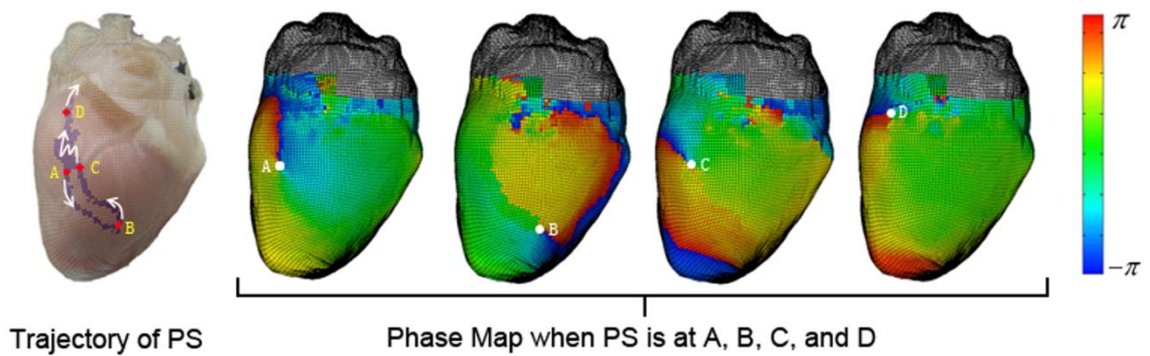
Figure 7. Trajectories of phase singularity (PS). The left-most panel is the trajectories of phase singularities on the anatomy. The phase maps corresponding to four phase singularities (A, B, C and D) are also shown.

16

remaining images of Fig. 7 show the corresponding phase map when the phase singularity is at individual point A, B, C and D. Overall, the ability of global visualization of phase singularities allows the investigation of the nonlinear dynamics of the ventricular arrhythmia especially when the phase singularity is meandering. Furthermore, the ability to correlate phase singularity with anatomy provides the potentials to investigate the relationship between phase singularity and structural heterogeneities.
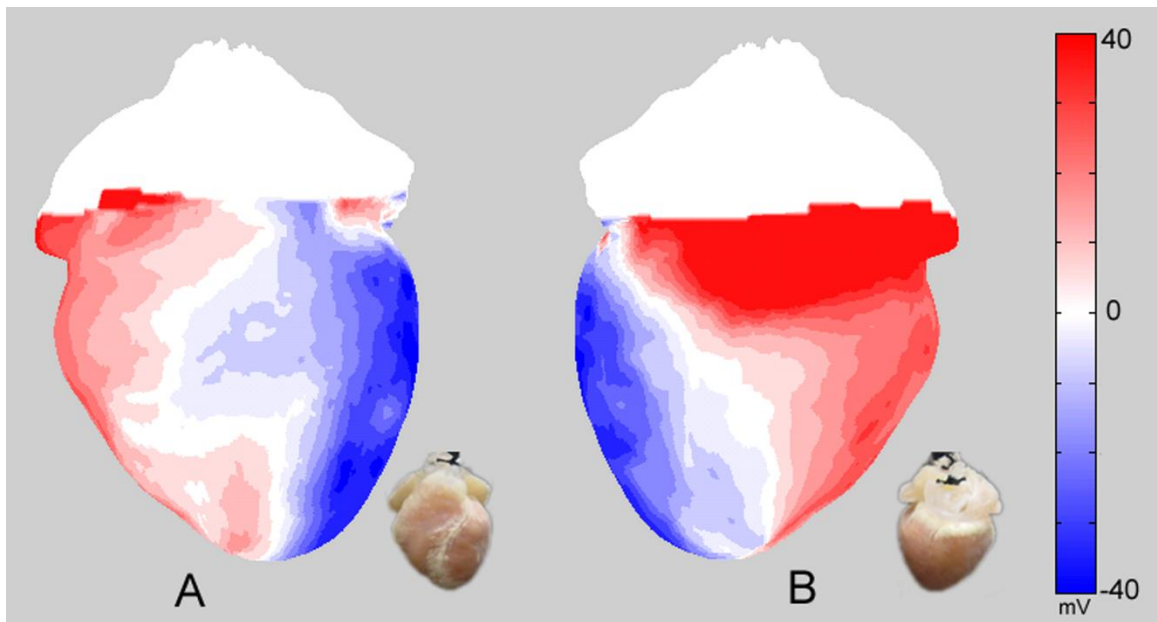
Figure 8. Shock-induced virtual electrode (VEP) map. (A) Anterior view. (B) Posterior view.

Shock-induced VEP is an important mechanism for success and failure of defibrillations (40, 64, 66). Figure 8 shows the VEP induced by far field shock at approximately 85% of APD_{80}. It is already known (64) that shock-induced VEP could generate higher VEP gradient at both base and apex than region in between from anterior view (Fig. 8A), thus creating condition for reentry. With the panoramic setup, not only is the anterior VEP

pattern visible, but also the posterior (Fig. 8B). In Fig. 8B, the posterior view shows higher

gradient in the base and apex also, similar to what we saw from the anterior. Overall there

are four phase singularities created, two in the anterior and two in the posterior. This creates

a condition for quatrefoil reentry. Since reentry is unstable in a young normal rabbit heart,

the arrhythmia self-terminates after one rotation.

2.4.2 Conduction Velocity in Simulations and Epicardial Pacing

In the simulation, radially propagating waves were constructed on a meshed sphere to mimic

epicardial pacing in the heart surface. We optimized the velocity estimation method and

tested its validity while changing the size of the spatiotemporal region (the "time window"

and "space window") used for polynomial fitting.

We found that estimates of conduction velocity depend weakly on analysis parameters,

such as the extents in space and time of the local polynomial fit. Results from simulations

with resolution and surface parameters similar to experiment, were used to choose

parameters for analysis of experimental data. In the simulation, deviations from exact speed

can be tracked. The deviations first decrease, and then increase as the spatial extent of fitting

region increases. Figure 4B shows the normalized error of conduction velocity at different

spatial and temporal extent of the fitting region. Values for the space and time windows that

correspond to the lowest error in simulation were chosen. Note that this non-ideal

dependence of velocity estimates on fitting parameters would be reduced if temporal and

spatial resolution of activation times were increased significantly. In summary, we found the

values of time window and space window that produced the lowest errors in our simulations,

and used them for our experimental data set.

18

The accuracy of the conduction velocity estimation depends on the polynomial fitting of activation time $t(\theta,\varphi)$. Polynomial fitting eliminates the inaccuracy due to the noise or insufficient resolution by its smoothing effect. This explains why the normalized error initially decreases when the space window increases in Figure 4B. On the other hand, the error increases when $t(\theta,\varphi)$ is not well fitted. This happens when large space window and/or time window are chosen. This is evident from Figure 4B that the normalized error starts to increase monotonically as space window becomes larger than certain value.
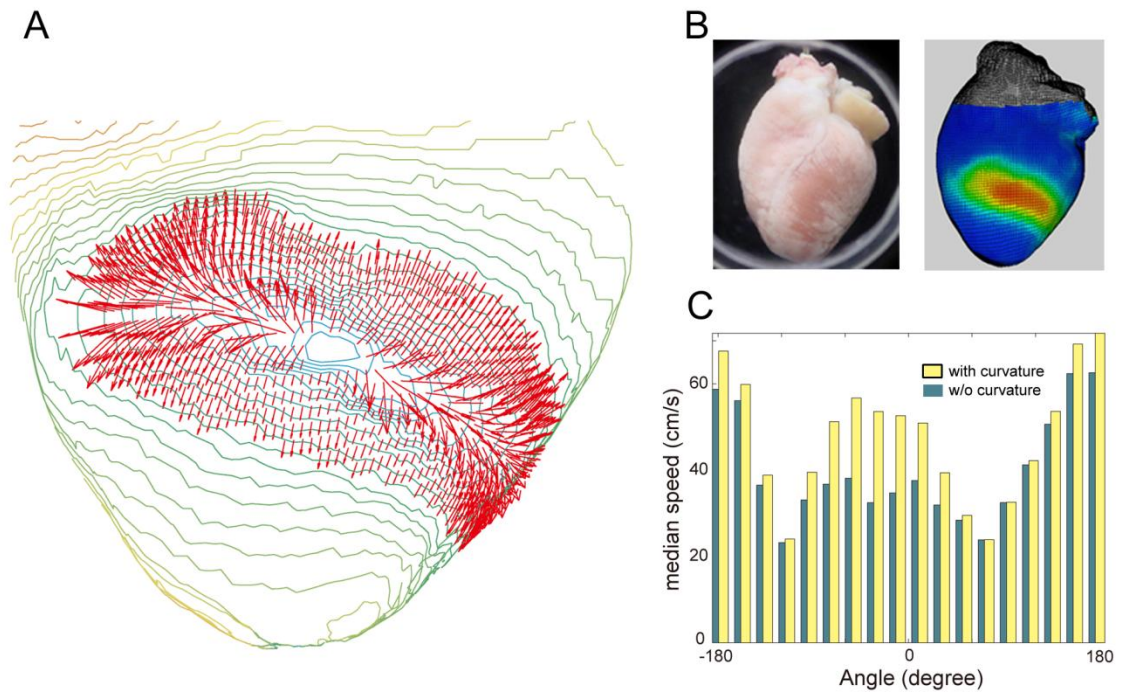
Figure 9. Conduction velocity in epicardium during pacing. (A) Conduction velocity vectors after epicardial pacing. The activation isochrones has an interval of 2ms. (B) Anatomy and snapshot of transmembrane voltage. (C) Conduction velocity versus angles of conduction velocity. The angle of zero corresponds to the direction pointing to right. Angle increases in the counterclockwise manner. The yellow bar represents the condition when curvature of the surface is accounted for during the calculation of conduction velocity, while green bar is the opposite case.

Figure 9A shows result of application of our method during epicardial pacing. The isochrones and conduction velocity vectors (red arrows) are shown. A snapshot of transmembrane voltage and anatomy are in Fig. 9B. Because of anisotropic conductance, the conduction velocity distribution over various angles has a sinusoidal shape (yellow bars in Fig. 9C). The peak value corresponds to the conduction velocity parallel to fibers; and the minimum value corresponds to the conduction velocity perpendicular to the fiber direction.

Figure 9C also shows the effect of surface curvature on the conduction velocity. If we simplify the calculation by assuming that all signals come from a focal plane, the resultant conduction velocity distribution will be like that in green bars. The green bars are generally shorter than the yellow bar, especially at the peaks. This means that the conduction velocity is underestimated when the velocity component normal to the plane is ignored. Since peak conduction velocity appears more on the edges of the field of view, where surface curves away, the deviations of peak conduction velocity is usually more significant. We quantified the effects of curvature in four hearts on the ratio of conduction velocity along longitudinal and transverse direction. The ratio is 2.45 ± 0.78 when no curvature is considered, different from the ratio 2.98 ± 0.84 when curvature is considered. The ratio is underestimated approximately by 17.8% if the curvature is not considered.

This method can also be applied to reentrant activity during arrhythmia, i.e. ventricular tachycardia, when the conduction is mostly parallel to the epicardium. Figure 10 shows the conduction velocity vectors during stable reentrant spiral waves around a line of block.
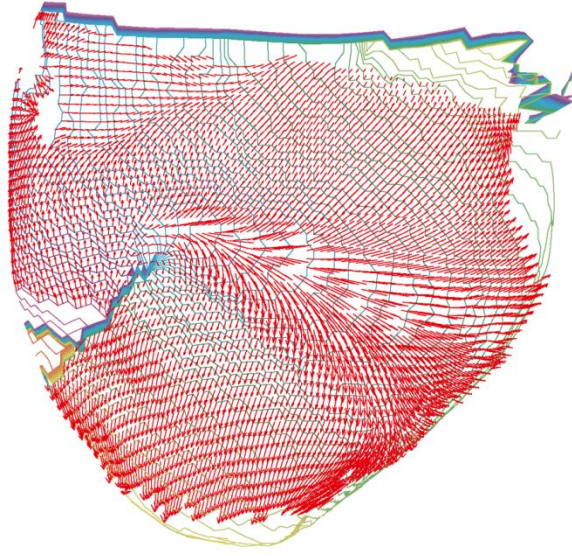
Figure 10. Epicardial conduction velocity during reentry. Wave propagates around a line of block which is represented by clustered isochrones. The interval of activation isochrones is 2ms.

2.5 Discussion

In this paper, we presented methods to quantify the panoramic imaging data sets which have not been systematically presented before. We first transformed the mapping data from three PDAs into one 2D array, and then implemented quantitative analysis including dV/dt map, phase map, activation map and electric stimulus induced VEP map. We also adapted the method of Bayly et al. (11) for conduction velocity to the panoramic data sets. This method is tested on simulated, radially-propagating waves on a spherical surface.

Rogers (223) introduced anther framework for analysis of panoramic data sets by allowing locating phase singularity in an unstructured triangular mesh. This method is more general and works on the complex geometry. Our method, on the other hand, takes advantage of

simple geometry of the ventricles and simplicity of grid data set. It is simpler to implement and computationally less expensive.

All the methods mentioned in this paper can be implemented within a reasonable time period during experiment. Once silhouette images are obtained, a low resolution (e.g. 2mm) heart surface geometry can be obtained in about 20 seconds on a Windows PC (Pentium (R) 4, 3.19 GHz CPU, 1.99 GB of RAM) using Matlab 7.0.1 (The Mathworks, Natick, MA). Higher resolution (e.g. 1mm) reconstruction takes about 75 seconds. The user must manually register the heart surface to each PDA field of view, which takes approximately 5~10 minutes. Then, the heart geometry can be saved and used for texture mapping. This fast and convenient method allows us to reconstruct and analyze every heart mapped in a reasonable amount of time.

The panoramic imaging setup optically mapped almost all the regions of the ventricles and parts of the atria. It should be noted that the spatial resolution at the tip of the apex can be low since the bottom curves away from every PDA. For the same reason, the spatial resolution is low at the edges of the field of view of every PDA. However, signals generated by these side regions are always simultaneously captured by two PDAs. As a result, sufficient resolution and signal to noise ratio can be restored from signals recorded from two PDAs (213).

Epicardial conduction velocities can be quantified on nearly the entire ventricular epicardium. However, caution needs to be taken to interpret the conduction velocity because conduction is three-dimensional in nature. The apparent epicardial conduction velocity is an

accurate representation of actual conduction velocity only when the wavefront propagates nearly parallel to the epicardial surface.

The analysis of panoramic mapping data introduced here enhances our ability to investigate the electrophysiology and non-linear dynamics of the heart. This provides an improved global perspective from which to investigate the cardiac conduction in normal and diseased conditions.

3. The Role Of Dynamic Instability And Wavelength In Arrhythmia Maintenance Revealed By Panoramic Optical Imaging With Blebbistatin Versus 2,3-Butanedione Monoxime

3.1 Abstract

Unlike other excitation-contraction uncouplers, blebbistatin has few electrophysiological side effects, and has gained increasing acceptance as an excitation-contraction uncoupler in optical mapping experiments. However, the possible role of blebbistatin in ventricular arrhythmia has hitherto been unknown. Furthermore, experiments with blebbistatin and 2,3-butanedione monoxime (BDM) offer an opportunity to assess the contribution of dynamic instability and wavelength of impulse propagation to the induction and maintenance of ventricular arrhythmia.

Recordings of monophasic action potentials were used to assess effects of blebbistatin in Langendorff-perfused rabbit hearts (n = 5). Additionally, panoramic optical mapping experiments were conducted in rabbit hearts (n = 7) which were sequentially perfused with BDM, then washed out, and subsequently perfused with blebbistatin. The susceptibility to arrhythmia was investigated using shock-on-T protocol. We found that (i) application of blebbistatin did not change action potential duration (APD) restitution; (ii) in contrast to blebbistatin, BDM flattened APD restitution curve and reduced the wavelength; (iii) incidence of sustained arrhythmia was much lower under blebbistatin than under BDM (2/123 vs. 23/99). While arrhythmias under BDM were able to stabilize, the arrhythmias under blebbistatin were unstable and terminated spontaneously.

In conclusion, the lower susceptibility to arrhythmia under blebbistatin than under BDM indicates that blebbistatin has less effects on arrhythmia dynamics. A steep restitution slope under blebbistatin is associated with higher dynamic instability, manifested by the higher incidence of not only wave breaks but also wave extinctions. This relatively high dynamic instability leads to the self-termination of arrhythmia, because of the sufficiently long wavelength under blebbistatin.

3.2 Introduction

Optical imaging techniques have been widely used to study the cardiac electrophysiology in species ranging from embryonic zebrafish to human beings (68, 89, 126). Optical mapping offers several important advantages over alternative mapping techniques: easily adjustable high spatial resolution, no physical contact with the tissue, absence of stimulation artifacts, and the capacity to simultaneously map different physiological parameters (68). Despite these advantages, optical mapping suffers from the need to utilize excitation-contraction (EC) uncouplers in order to remove motion artifacts from the optically recorded signals. Unfortunately, most of these uncouplers have electrophysiological side effects. For example, a popular inexpensive uncoupler 2,3-butanedione monoxime (BDM) results in changes of the action potential (AP) and conduction velocity (CV) in a species-dependant manner by affecting the ion channels, Ca^{2+} handling, and gap junctional coupling (46, 158, 226, 251, 258). Another EC uncoupler, Cytochalasin D, also changes AP morphology (8, 22, 39) by affecting various ion channels (170, 188, 219, 244).

Our group has previously shown that blebbistatin could completely eliminate mechanical contraction without appreciable electrophysiological effects on AP morphology, ECG parameters, conduction, and refractoriness in the rabbit heart (76). Following this introduction of blebbistatin as an EC uncoupler (76), it has increasingly gained popularity in cardiac electrophysiological studies. As of today, it was successfully applied in optical mapping studies of the hearts from embryonic zebrafish (120), mouse (61), rabbit (76, 176, 191), dog (78, 129), horse (80), and the human beings (73, 74, 89, 159).

Both BDM and cytochalasin D were found to affect the vulnerability to ventricular arrhythmias (39) and the pattern of ventricular fibrillation (110, 143, 221). However, the effect of blebbistatin on ventricular arrhythmia is unknown. The aim of this study was to determine the vulnerability and characteristics of shock-on-T-induced arrhythmias under blebbistatin compared with BDM. Since shock-induced arrhythmia typically self-terminates in normal rabbit hearts *in vivo* (167) and *in vitro* (39) in the absence of EC uncoupler, we hypothesized that sustainability of shock-induced arrhythmia will be lower under blebbistatin versus BDM.

3.3 Methods

3.3.1 Experimental protocols

New Zealand White rabbit hearts (n = 12, 4 months old) were Langendorff-perfused with oxygenated 37 °C Tyrode's solution as previously described (161, 214). In the first set of experiments (n = 5), we recorded monophasic action potentials (MAP) using a MAP electrode (Harvard Apparatus, Holliston, MA) under control condition (i.e., no drug) and under 10μM blebbistatin. We applied the S1S2 ventricular pacing protocol consisting of an

initial train of 15 S1 stimuli with an S1-S1 interval of 300ms followed by a single S2 stimulus. We gradually decreased the S1-S2 interval from 400ms to the refractory period. Pacing current was adjusted to twice the pacing threshold. Continuous MAP recordings were maintained under both conditions. No voltage-sensitive dye was used in this part of the study.

In the second set of experiments (n = 7), the heart was stained with di-4-ANEPPS (20~40μL of 1.25mg/ml, Invitrogen, Carlsbad, CA). The heart was perfused in the following sequence: (1) Tyrode's solution with 15mM BDM (Fisher Scientific, Hampton, NH); (2) Tyrode's solution alone to wash out the BDM; (3) Tyrode's solution with 10μM blebbistatin (Tocris Bioscience, Ellisville, MO). The S1S2 pacing protocol and vulnerability grid measurement for shock-induced arrhythmia were conducted under both BDM and blebbistatin.

The same S1S2 pacing protocol used in the first experimental set was applied for the quantification of APD restitution and CV restitution. The bipolar pacing electrode was placed epicardially in the center of the anterior view of the heart to allow the measurement of the CV in both longitudinal and transverse directions of the fiber orientation, as described earlier (162, 214).

The vulnerability to shock-induced arrhythmia was quantified using the vulnerability grid (70, 148), in which inducibility of arrhythmia was determined for varying shock strengths (2 - 14 V/cm) and varying coupling intervals spanning the T-wave (equivalently, 70% - 140% of the averaged APD). Uniform far-field square monophasic shocks (10ms in duration) were delivered via two mesh electrodes on opposite sides of the heart (63, 148) after a train of 15

stimuli with S1-S1 interval of 300 ms and varying coupling interval between the last S1 and the shock. The arrhythmia was categorized as "nonsustained" if it lasted >6 beats but ≤1 min after the shock. The arrhythmia was defined as "sustained" if it lasted for >1 min, which always required a defibrillation shock for termination. To avoid excessive shocks applied to the heart, the vulnerability grid was tested for just one polarity configuration where the mesh electrode facing the right ventricle (RV) was the cathode and the mesh facing the left ventricle (LV) was the anode.

3.3.2 Optical imaging system

The panoramic optical imaging system could record the optical AP from almost the entire ventricular epicardium of the rabbit heart (149, 222). Details of the panoramic imaging system and corresponding data analysis methods have been described earlier (162, 214). This system, including three photo-diode arrays (PDAs), optically maps the action potentials at three different angles (120° apart). In order to combine the data from three PDAs into one unified surface, the epicardial three-dimensional surface of every experimented rabbit heart was first reconstructed from 36 silhouette images of that heart. The optical signals were then registered onto the reconstructed surface. After that, various parameters, including APD, CV, wavelength (APD × CV) and wave propagation, were quantified and can be visualized on the reconstructed surface. To characterize Winfree's "elbow room" needed for reentry to sustain, we introduce a new factor - wavelength surface area, computed as the product of longitudinal and transverse wavelengths.

3.3.3 Data analysis

The APD was measured at 80% repolarization (APD80). The longitudinal and transverse CVs were measured near the pacing site at the epicardial surface. The phase was calculated

by Bray's method (30) and was used to visualize the wavefronts and phase singularities during reentrant arrhythmias. Comparisons were made between results under blebbistatin and BDM, as well as between control and blebbistatin. The Student's paired *t*-test was used to determine the level of statistical significance. $P<0.05$ was considered statistically significant. Values were given as means $\pm$ S.D.

3.2 Results

3.2.1 Monophasic action potential with and without blebbistatin

To determine the effects of blebbistatin on the AP morphology and APD, the MAP were recorded before and after the application of blebbistatin under multiple pacing rates. We did not detect significant differences between the control and blebbistatin in the measurement of APD. Figure 11 shows representative MAP recordings (Fig.11*A*) and the statistical summary (Fig.11*B*). The overlap between the MAP recordings and ECG for the control (blue color) and blebbistatin (red color) in Fig.11*A* indicates no change of AP morphology after the application of blebbistatin. This is further demonstrated in the summary in Fig.11*B*, which showed no significant effects of blebbistatin on APD.
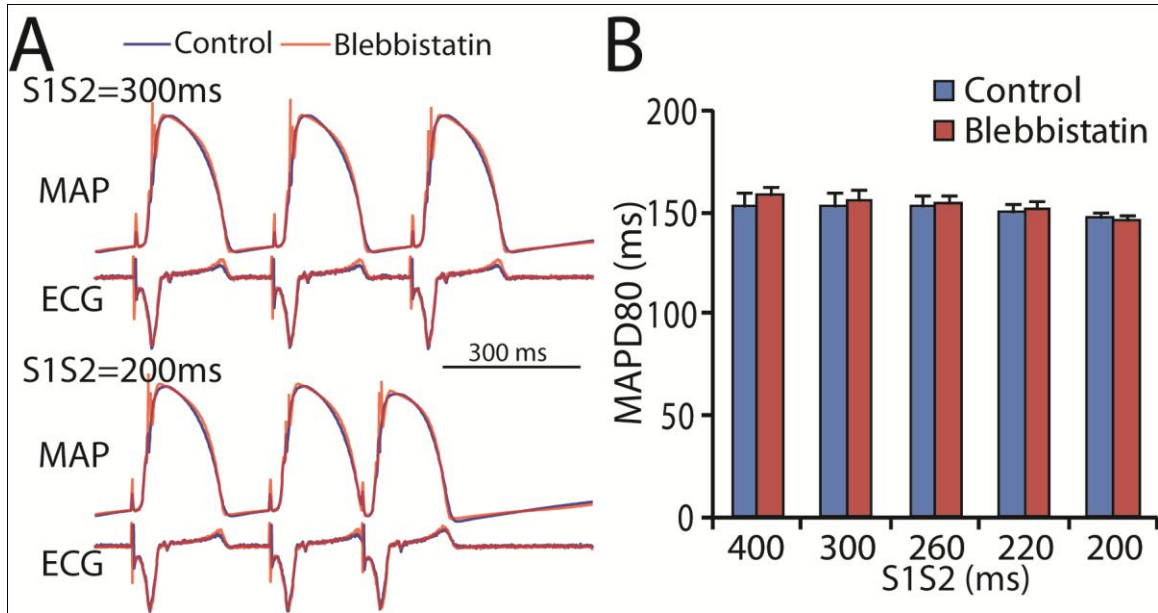
Figure 11. Monophasic action potential (MAP) recordings. (A) Representative MAP and ECG recordings for S1S2 = 300ms and 200ms. (B) Summary of MAP durations at 80% repolarization (MAPD80) at various S1S2s. MAPD80 was not significantly changed under blebbistatin.

3.2.2 Vulnerability to shock-induced ventricular tachyarrhythmia

Figure 12 shows the arrhythmic incidence at different shock strengths and various coupling intervals under BDM (Fig.12*A-Left*) and blebbistatin (Fig.12*A-Right*). In total, 99 shocks were applied under BDM and 123 shocks were applied under blebbistatin in all hearts. The overall incidence of arrhythmia (including both nonsustained and sustained arrhythmia) was 38/99 under BDM and 33/123 under blebbistation (Fig.12*A-Top row*). On average, the incidence was significantly lower under blebbistatin (27±12% under blebbistatin versus 51±20% under BDM, $p = 0.046$, Fig.12*B*). Furthermore, the total incidence of sustained arrhythmia is 23/99 under BDM and 2/123 under blebbistatin (Fig.12*A-Bottom row*). That is, the average probability of sustained arrhythmia under blebbistatin was drastically lower than under BDM (1±4% under blebbistatin versus 30±14% under BDM, $p = 0.001$, Fig.12*B*).

Figure 12. Vulnerability grid and incidence of shock-induced arrhythmia. (A) Vulnerability grid with the inducibility of arrhythmia shown for various shock strengths and coupling intervals for both BDM (left, n=7) and blebbistatin (right, n=7). The top row shows the incidence of nonsustained and sustained arrhythmia combined. The bottom row shows the incidence of sustained arrhythmia only. It can be seen that the inducibility of sustained arrhythmia is significantly lower under blebbistatin (23/99 under BDM vs. 2/123 under blebbistatin). (B) Summary of the incidence of shock-induced arrhythmia.

31

Figure 13. Induction of arrhythimia by a T-wave shock. (A) Representative action potential recordings with shock marked by the orange stripe. (B) The virtual electrode polarization pattern induced by a 10 V/cm shock at a coupling interval of 160ms. The red color indicates the positive polarity (virtual cathode); the blue color indicates the negative polarity (virtual anode). (C) Post-shock activation snapshots with the end of shock indicated by 0ms. The shock-induced wavefront initiates from the border between positive and negative virtual electrode polarization and propagates in the form of figure-of-8 reentry.

3.2.3 Induction of arrhythmia

The induction of arrhythmias was similar under both conditions and was due to a well-established mechanism termed virtual electrode-induced phase singularity (65). Figure 13 shows a representative example of arrhythmia induction (under BDM). Essentially, the far-field shocks produced spatially heterogeneous virtual electrode polarizations at different regions of the heart (Fig.13*A&B*), consisting of a virtual anode (blue) and a virtual cathode (red). Fig.13*C* shows a sequence of snapshots of activation wavefronts (dark red) over the course of arrhythmia induction, starting immediately after the shock. A wavefront of excitation arises at the boundary between the virtual cathode and the virtual anode via the break-excitation mechanism (see emerging red area in the snapshots for 10ms and 30ms at Fig.13*C*). Then it spreads to the de-excited region of the virtual anode, leading to the initiation of reentrant arrhythmia maintained by two phase singularities with opposite topological charges. Phase singularities are seen in Fig.13*C* as points where all phases, represented by different colors, converge.

3.2.4 Stabilization of arrhythmia under BDM

In the beginning of the shock-induced reentrant arrhythmia, the phase singularity (or singularities) of the reentry was (were) mostly not stable and were meandering under both BDM and blebbistatin. Differing from the arrhythmia under blebbistatin, phase singularities under BDM were much more likely to stabilize and stop meandering. This difference is indicated by the dramatic difference in the incidence of sustained arrhythmia (Fig.12). Fig.14*A* shows an example, with the snapshots of wavefronts (dark red) showing the steps of the stabilization of the reentry under BDM. In the first beat, there are multiple lines of conduction blocks, indicated by the crowded isochrones. The number of conduction blocks

is reduced to one in the 2nd beat since we know that the left side connects with the right

side in that unwrapped map. After that, this line of conduction block starts to shrink until

the reentry has stabilized (3rd to 8th beats).
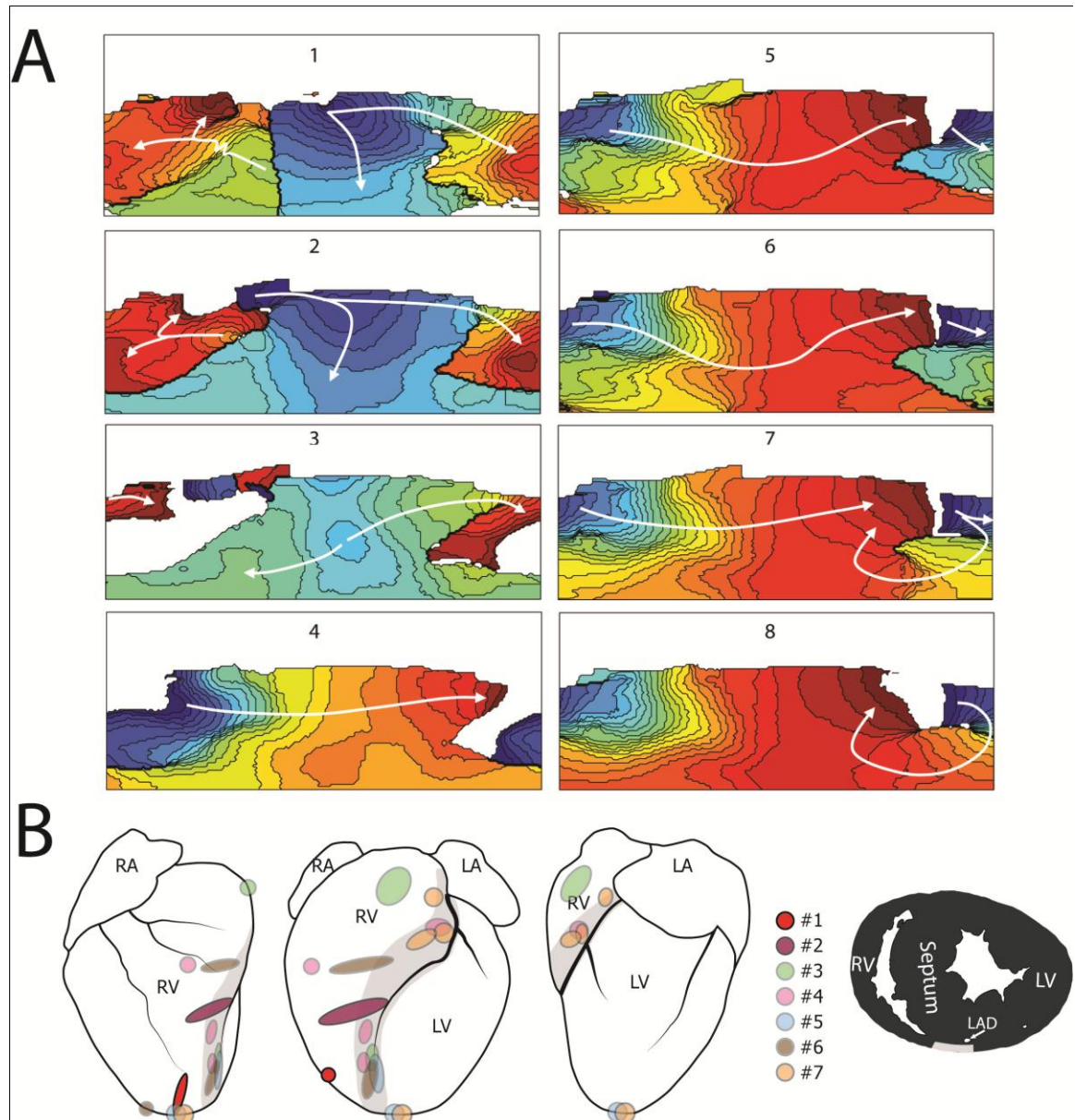
Figure 14. Stabilization and anchoring of reentry under BDM. (A) Stabilization of a meandering wave to stable reentry under BDM. Activation maps of eight consecutive beats before the stabilization of the single reentry. The activation is from blue to red with 2 ms interval between two neighboring isochrones. (B) Summery of the anchoring sites of stable reentry under BDM. Three different views from left to right: view

We observed 17 morphologies of stable reentries, with each having a single or double phase singularity (or singularities) at the epicardium under BDM. The locations of all phase singularities from seven hearts are summarized in Figure 14*B* at three different views (anterior, RV, and LV). It can be seen that the anchoring of reentry was geometrically asymmetrical, with the highest probability at the gray area in Fig.14*B*, where RV inserts into the septum and LV. Less frequently, the reentry anchored at the apex or at the RV freewall (Fig.14*B*). Interestingly, no epicardial anchoring at the LV was observed.

3.2.5 Unstable maintenance and self-termination under blebbistatin

Despite a similar mechanism of arrhythmogenesis, the dynamic maintenance of shock-induced arrhythmia was different under blebbistatin. Similar to the *in vivo* observations (167), more than 98% of the shock-induced arrhythmia self-terminated under blebbistatin within one minute. Wave breaks and wave collisions were common, and the wave propagation was unstable with beat-to-beat variations under blebbistatin. Figure 15 shows snapshots of wave propagations under BDM (Fig.15*A*) and blebbistatin (Fig.15*B*) in the same heart. It can be seen that the reentry under both conditions anchors at the apex of the heart. Despite the similarity in the anchoring site, the regularity or stability of reentry differs under these two conditions. The bottom-right plot in each panel shows the activation sequence of all the recorded epicardial sites over the course of three consecutive beats. That is, each green dot in this panel indicates the activation of a particular mesh element (y-axis) at a particular time

(x-axis). The repeatability of the activation pattern for every beat shown in Fig.15*A-Bottom right* indicates the regular and stable conduction under BDM. On the other hand, small local conduction blocks (arrows in Fig.15B) were frequent under blebbistatin. Fig.15B-*Bottom right* shows the beat-to-beat variation in propagation. The holes within the green stripes in Fig.15B-*Bottom right* indicate the local wave breaks and subsequent wave extinctions (or collisions) . While the stable reentry under BDM was terminated by a defibrillation shock, the unstable reentry under blebbistatin self-terminated during the intermission between two consecutive data acquisitions.

Figure 16 is an example of self-termination of an unstable figure-of-8 reentry under blebbistatin, which was anchored at two phase singularities (white dots). Fig. 16*A* is an AP recording over the course of pacing, shock, arrhythmia, and self-termination. Fig. 16B shows phase maps (in polar view with the apex in the center) indicating the two phase singularities with opposite topological charges induced by the shock. It is clear that the locations of phase singularities gradually changed over time. The reentry self-terminated due to the collision and annihilation of two phase singularities in the last beat. Fig.16*C-E* are several other snapshots of activation in the same recording, and shows two characteristics of reentry frequently observed under blebbistatin but not under BDM. One characteristics is the "stop-sign phenomenon", during which the wavefront appears to stop for a while and then continues from where it stopped (Fig.16C). This behavior is also evident from the temporal gaps between activations from all mapped areas on the epicardium (Fig.16D). Another characteristics is that a breakthrough often appears ahead of the wavefront (Fig.16E). Both characteristics suggest the presence of transmural activations.

A

0   1000   2000   3000 ms

Apex

0ms   25ms   50ms

π

0

-π

75ms   100ms

B

0   100   2000   3000 ms

0ms   25ms   50ms

π

0

-π

75ms   100ms

37
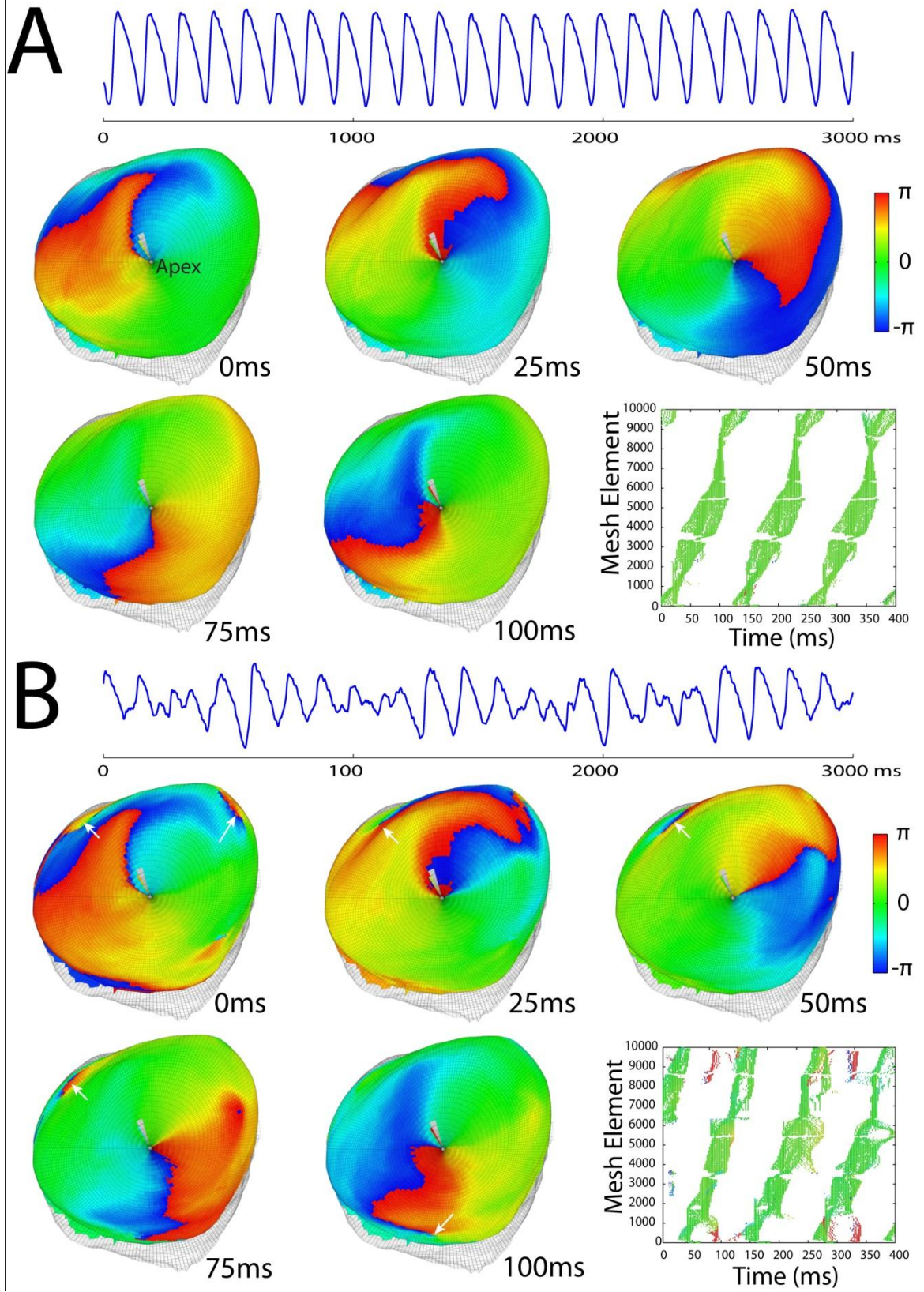
Figure 15. The stability of reentrant arrhythmia under BDM (A) and blebbistatin (B) in one heart. A representative action potential recording is shown on the top of each panel. Phase maps within a cycle of reentry are shown in each panel with the view toward the apex of the heart. The white arrows shown in the phase maps for blebbistatin point out transient conduction blocks, which were frequently observed under blebbistatin. It can be seen that both reentries anchor at the apex of the heart. While the reentry last under BDM, the reentry terminated spontaneously under blebbistatin. The activation pattern of three consecutive beats is plotted on the bottom right of each panel, with each green dot indicating an activation of every individual element of the meshed surface. The beat-to-beat variation is evident from the plot for blebbistatin.

3.2.6 APD and CV restitution and wavelength

Fig.17*A* shows representative optical AP recordings, and Fig.17*C-top* summarizes APD restitution curves under blebbistatin and BDM. Fig.17*B* shows representative activation maps, and Fig.17*C-middle* shows CV restitution curves along both longitudinal and transverse directions under blebbistatin and BDM. As expected, the APD was shorter and the APD restitution curve was flatter under BDM; the CV was slower under BDM in both directions. Wavelength was computed for longitudinal and transverse conduction and was significantly longer under blebbistatin than BDM (Fig.17*C-bottom*). At different cycle lengths, the wavelength surface area, which is a simple estimation of area needed for sustaining reentry, ranged from 19~34 cm^2 under BDM and 39~60 cm^2 under blebbistatin. The average ventricular epicardial surface area was 39.4±4.9 cm^2 (n=7), which was well above the wavelength surface area of BDM but close to or below the wavelength surface area of blebbistatin.
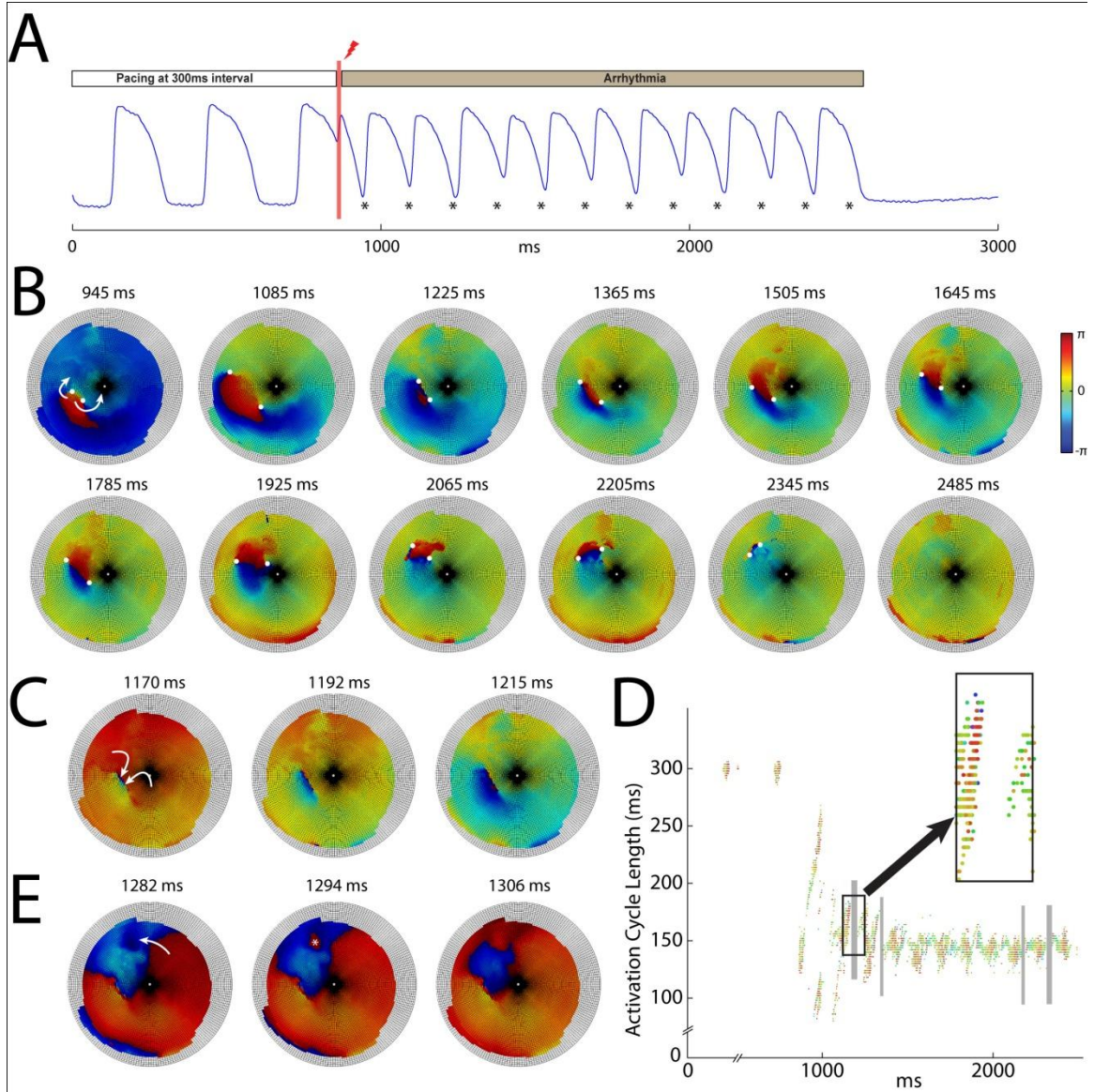
Figure 16. Self-termination of reentry under blebbistatin. (A) A representative action potential recording. Shock is indicated by the orange stripe. (B) Phase maps from 12 consecutive beats (time points indicated by the asterisks in panel A) with phase singularity indicated by white dots. The map is shown in polar form with apex in the center. It is evident that the pivots of figure-of-8 reentry meanders overtime. The collision of the two phase singularities with opposite topological charge led to the termination of arrhythmia. (C) Wave front and tail collision. Three consecutive phase maps shows that the wavefront stops for 45 ms before it continues. (D) The activation plot with each dot corresponding to an activation of one pixel. Each pixel is coded with an unique color. The y-axis is the cycle length. The gray stripes indicate the gap where no epicardial activation is observed and correspond to the wave front and tail collision seen in the panel C. (E) Breakthrough excitation ahead of the wavefront. Three consecutive phase maps are shown with the breakthrough excitation (indicated by the white asterisk) visible on the second one.
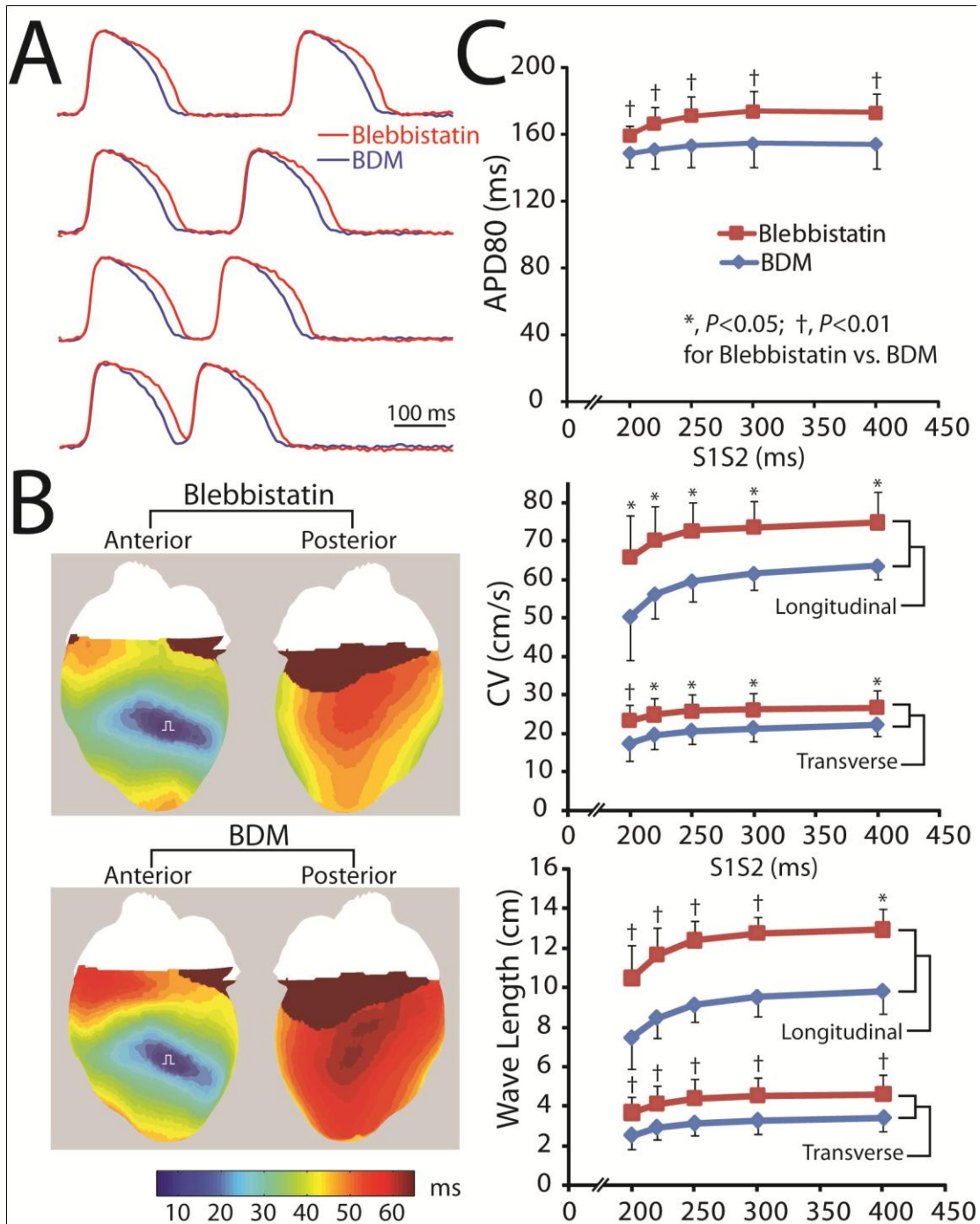
Figure 17. Comparison of action potential duration (APD) restitution, conduction velocity (CV) restitution, and wavelength (APD × CV) between blebbistatin and BDM. (A) Representative AP recordings under blebbistatin (red) and BDM (62) at various S1S2 coupling intervals. (B) Representative activation maps under BDM and blebbistatin for both anterior and posterior view of the heart. (C) .(C) APD, CV and wavelength at varying cycle lengths. CV and Wavelength are shown for both longitudinal and transverse conduction. It can be seen that BDM significantly decreases APD and flattens APD restitution, significantly reduces CV and wavelength on both longitudinal and transverse direction

3.3 Discussion

In this study, we investigated the effect of blebbistatin on the vulnerability to shock-induced ventricular arrhythmias in the normal rabbit heart. We found that (1) APD restitution under blebbistatin was not significantly different from the control condition, (2) BDM significantly reduced APD, CV, and wavelength; and flattened APD restitution, and (3) the sustainability to shock-induced arrhythmia was much lower under blebbistatin (2/123) than under BDM (23/99). These results showed that blebbistatin did not affect the vulnerability to shock-induced arrhythmia and suggested blebbistatin as a superior EC uncoupler to BDM in the arrhythmia studies using optical mapping. In addition, both dynamic instability and wavelength appear to contribute to the self-termination of arrhythmia under blebbistatin, and therefore explain the lower susceptibility to sustaining arrhythmia under blebbistatin than under BDM.

3.3.1 Effect of blebbistatin on electrophysiology

It has been previously shown that the ventricular arrhythmia in the normal rabbit heart is prone to self-termination (12, 39, 167). The resistance to sustained arrhythmia under blebbistatin observed in this study suggests the preservation of normal electrophysiology by blebbistatin. We did not observe any changes of ventricular AP morphology under blebbistatin, which is consistent with other studies in the rabbit heart (76, 125), mouse heart (61), embryonic zebrafish heart (120), and equine heart (80). Taken together, these results suggest insignificant electrophysiological side effects of blebbistatin.

While blebbistatin appears to be a "clean" drug for the normal heart, whether blebbistatin changes the electrophysiology in the diseased heart remains to be determined. Blebbistatin

inhibits myosin ATPase and thus prevents a significant amount of ATP from being consumed by mechanical contractions, making it available to electrogenic pumps. This effect could enhance the metabolic state of excitation and calcium handling in a diseased heart. Baudenbacher et al. (10) showed that Ca^{2+} desensitization of myofilaments by blebbistatin could reduce the arrhythmia in transgenic mice expressing troponin-T mutations. By inhibiting the contraction, blebbistatin could also prevent sarcolemmal rupture and cell death by reducing the mechanical stress occurring at the onset of reperfusion after ischemia (87, 116). These protective effects of blebbistatin suggest that caution should be taken in applying blebbistatin when studying diseased heart.

3.3.2 Functional reentry in the rabbit heart

Since there is no structural obstacle (such as myocardial infarction scar) in these normal rabbit hearts, the anchoring of reentry under BDM is achieved at the normal anatomical structures. This observation suggest that an abnormal structure is not necessary for sustaining the arrhythmia. The observed asymmetrical distribution of anchoring points of stable reentrant arrhythmia (Fig.14*B*) indicates that the anterior RV insertion area (gray area in Fig.14*B*) is the most favorable area for anchoring. A computer simulation study by Park et al. (199) also identified the anterior RV insertion area as a distinct substrate for arrhythmia. In their whole rabbit ventricular model with global reduction of Na^+ currents (199), they found that the RV insertion area was more susceptible to arrhythmia because of a source-sink mismatch in the RV insertion area (199).

These results suggest that global electrical remodeling does not necessarily lead to a spatially homogeneous increase in the arrhythmia susceptibility. Washout of BDM and application of blebbistatin in our study almost completely abolished the maintenance of

ventricular arrhythmia, suggesting that idiopathic ventricular tachycardia with normal heart structure might respond well with pharmacological intervention, despite the presence of several preferential anchoring points of reentry.

3.3.3 Dynamic instability under blebbistatin

According to the computer simulations, steep APD restitution is associated with enhanced dynamic instability (36, 193, 216, 218). This association could partially explain the more unstable wave dynamics under blebbistatin than under BDM. The instability of wave propagation under blebbistatin was reflected by frequent wave breaks and wave extinctions. The dynamic instability is further reflected by the frequent occurrence of breakthrough excitation ahead of the reentrant wavefront under blebbistatin (Fig.16E). This type of breakthrough excitation on the surface of 3D tissue has been previously observed in an elegant computer simulation study of scroll wave dynamics by Qu et al. (216), who demonstrated correlation between the breakthrough activity with the strong dynamic instability. In a 3D tissue like the rabbit heart in this study, a scroll wave faces excitable tissue not only in its own layer but also in the neighboring layers. According to the simulation (216), the strong dynamic instability and fiber orientations could result in different speed of spiral waves at different layers of the tissue. When the spiral wave at a depth (or intramural conduction) is faster than the spiral wave on the surface, an upward propagation towards the epicardial surface could occur and thus produce the breakthrough excitation on the epicardial surface. The "first stop, and then continue" wavefront (Fig.16C) observed under blebbistatin also suggests the presence of intramural conduction connecting the epicardial activation gaps (Fig.16D).

3.3.4 Dynamic instability and self-termination of arrhythmia

Dynamic instability alone is not sufficient to prevent the maintenance of arrhythmias. Mines (175) and Garrey (88) postulated that the wavelength in comparison to tissue size is the major determinant of reentry maintenance. Numerous studies confirmed Mines and Garrey's theory. For example, Qu et al.'s simulation indicated that whether dynamic instability promotes or prevents the maintenance of arrhythmia depends on the effective tissue size, which is determined by the wavelength and the actual tissue size (215). This is supported by the experimental findings by Harada et al. (102). Compared with the control, severe hypothermia did not change the incidence of sustained arrhythmia despite a dramatic increase of dynamic instability, because severe hypothermia decreased the wavelength (102). On the other hand, mild hypothermia did not alter the wavelength while it increased the dynamic instability, resulting in a significant reduction in the incidence of sustained arrhythmia (102). The limited tissue size versus longer wavelength under blebbistatin was evident from the wavefront and waveback collisions (Fig.16).

It is difficult to quantify the individual contribution of dynamic instability and wavelength in the maintenance of arrhythmia, because the experimental approach does not have the luxury to finely tweak the dynamic instability and effective tissue size in three dimensions as the computer simulations so elegantly do. Nevertheless, our results indicate the beneficial role of dynamic instability and wavelength combined in preventing the maintenance of arrhythmia.

3.4 Limitation

There are limitations in this study. First, we could not measure the true wavelength during the arrhythmia, because the apparent epicardial CV might not reflect the true CV and the baseline (minimum of the signal) might not represent the resting state. Nevertheless, the wavelength surface area, which was calculated from wavelengths during pacing, works surprisingly well in predicting the sustainability of arrhythmia in this study. The second limitation is that reentry dynamics are only studied in the normal heart in this study. Caution is needed to extrapolate the results to diseased hearts. Third, the vulnerability of the heart to arrhythmia between the control condition and under blebbistatin are not compared in this study. However, low arrhythmia vulnerability is expected in the normal heart and has been demonstrated previously both *in vivo* and *ex vivo* (39, 167). Finally, we cannot exclude the effects of edema, which might develop in the mechanically silent preparations.

  In conclusion, the low incidence of sustained arrhythmia and the preserved APD resitution under blebbistatin suggest blebbistatin as a superior EC uncoupler to BDM. The combination of dynamic instability and wavelength facilitates the spontaneous termination of arrhythmia.

4. The Susceptibility to Alternans is Enhanced in a Rabbit Model of Chronic Myocardial Infarction

4.1 Abstract

Repolarization alternans plays an important role in the genesis of deadly arrhythmia, especially in patients with chronic myocardial infarction. It remains elusive how the healed myocardial infarct contribute to the repolarization alternans and dispersion of repolarization.

In this study, we studied inducibility and dynamics of action potential duration (APD) alternans using optical mapping in a rabbit model of healed myocardial infarction (>3months, n=9) and control rabbit hearts (n=9). We observed that (1) spatially concordant APD alternans occurred at a significantly slower heart rate in infarcted heart with control hearts (294 ± 27 bpm vs. 369 ± 25 bpm, $P < 0.001$), (2) the pacing rate threshold for spatially discordant alternans also significantly decreased in the infarcted heart compared with control heart (366 ± 47 bpm vs. 458 ± 53 bpm, $P = 0.014$), (3) increased alternans susceptibility is closely associated with the infarct border zone, (4) dynamic APD restitution curve could not predict and always overestimate the pacing rate at the onset of APD alternans in the infarcted heart, (5) conduction velocity alternans proceeded the occurrence of spatially discordant alternans in the infarcted heart, and (6) there existed a distinct pattern spatially discordant alternans in the form of small islands in the infarct border zone.

In conclusions, healed myocardial infarction promotes repolarization alternans especially in the infarct border zone. The subsequent increase of dispersion of repolarization could provide the substrate for the induction of ventricular arrhythmia.

4.2 Introduction

Sudden cardiac death is a leading cause of death and is most commonly associated with ventricular arrhythmias (225). Healed myocardial infarction is present in approximately half of sudden cardiac death cases presenting ventricular fibrillation (238). Despite the prevalence of healed myocardial infarction in the cardiac arrest victims, there has been little study of arrhythmia mechanism in the setting of a healed myocardial scar. Better understanding of mechanism could facilitate the development of anti-arrhythmic therapies such as the novel gene therapy (227).

Several clinical studies have identified reentry as the main mechanism for the ventricular tachycardia in the chronic phase of myocardial infarction (51, 261, 262). Using optical imaging technique, we have previously found that the maintenance of shock-induced ventricular tachycardia is closely associated the anchoring of mother rotors at the scar (148, 149). Ohara et al. showed that increased dynamic instability in the healed infarct border zone lead to a higher wavelet density which sustained the ventricular fibrillation (196). Compared with the knowledge of arrhythmia maintenance in the heart with healed myocardial infarction, the induction of arrhythmia is less known.

T-wave alternans, reflecting the beat-to-beat repolarization alternation, was found clinically to be a predictive marker for sudden cardiac death in patients with healed myocardial infarction (115, 189). Narayan et al. (189) found that T-wave alternans was spatially correlated with the scar in those patients, suggesting infarct border zone as the substrate of the repolarization alternans. Optical mapping technique has greatly enhanced the mechanistic understanding of T-wave alternans (or repolarization alternans) and its

linkage to the induction of arrhythmia (44, 176, 200, 201, 212, 265). Pastore et al. (200) nicely demonstrated that close correspondence between T-wave alternans and alternans of action potentials duration (APD) in normal rabbit heart. They also showed that spatially discordant alternans (APD alternans being out of phase between neighboring cells) lead to conduction block against steep gradient of repolarization and thus the initiation of reentrant arrhythmia (200).

In this study, we aimed to use optical mapping technique to explore the susceptibility to repolarization alternans in a rabbit model of healed myocardial infarction (>3 months), to determine the spatial correlation between alternans-susceptible regions and the scar, and to examine the contribution of APD restitution and conduction velocity alternans in the APD alternans in producing the APD alternans.

4.3 Methods

The experimental protocol was approved by the Institutional Animal Care and Use Committee of Washington University in St. Louis. New Zealand White rabbits (n=18) of either sex were used in this study. Half of the rabbits (n=9) underwent in vivo survival surgery as previously described (148, 149) to create chronic MI via ligation of a descending branch of the left circumflex artery. These rabbits were allowed to heal for at least 3 months before optical mapping experiments. The other half of the rabbits (n=9) were not subject to the surgery and were used as controls.

Rabbits were injected intravenously with sodium pentobarbital (50 mg/kg) and 1000-2000 U heparin. Hearts were quickly excised, and then Langendorff-perfused with 37°C Tyrodes' solution (in mmol/l: 128.2 mM NaCl, 4.7 mM KCl, 1.19 NaH_2PO_4, 1.05 mM $MgCl_2$, 1.3 mM

CaCl$_2$, 20.0 mM NaHCO$_3$, and 11.1 mM glucose, and gassed with 95% O$_2$-5% CO$_2$; pH=7.35±0.05) at an arterial pressure of 60–70 mmHg. The excitation-contraction uncoupler blebbistatin (10μM; TOCRIS) was added to the perfusate to suppress motion artifacts in optical recordings (76). The heart was stained with voltage sensitive dye RH237 (Invitrogen, CA) for optical action potential (AP) measurement. Fluorescent signals were recorded by CMOS camera (SciMedia, CA).

Dynamic restitution protocol was conducted starting at a basic cycle length (BCL) of 300ms. The heart was paced at the apical side of the right ventricle and optically mapped from the anterior surface. The pacing interval was gradually decreased until the heart cannot be paced or arrhythmia was induced. APD was quantified at the 80% repolarization (APD80) at each pixel of the camera. Dynamic APD restitution curves were constructed by plotting APD80 against the preceding diastolic interval (DI) for each pacing rate. DI was measured by the time from the 80% repolarization to the upstroke of next AP. The restitution curve was constructed by fitting the measurement using a single exponential (i.e., $APD = a - b * \exp(-DI/c)$, where a, b and c were coefficients and obtained by nonlinear least-square fits) or using a biexponential function (i.e., $APD = a - b1 * \exp(-DI/c1) - b2 * \exp(-DI/c2)$, where $a, b1, b2, c1,$ and $c2$ were coefficients and obtained by nonlinear least-square fits).

APD alternans was measured by ΔAPD (i.e, the difference in APD80 between two consecutive beats). The threshold of APD alternans was defined as the lowest pacing rate at which at least 10% of mapped region has APD alternans (i.e., $\Delta APD \geq 4ms$). The spatial organization of APD alternans will be presented by alternans maps with positive values

color-coded by red, negative values color-coded by blue, and zero by white. Sometimes APD80 of certain region cannot be quantified during alternans if the upstroke occurs before the decline of the previous action potential to 80% repolarization. In such cases, this region was color-coded by the saturated colors (deep red or blue) in the alternans map. Activation cycle length (CL) is measured based on the time duration between two consecutive AP upstrokes at each pixel. Activation CL alternans was also measured to reveal the conduction alternans. It should be noted that activation CL is different from the BCL.

Comparison was made between infarction group and control group. Levels of significance were determined by a Student's paired or unpaired t-test, where $p<0.05$ was considered statistically significant. Values were given as means ± S.D.

4.4 Result

4.4.1 Pacing Rate Threshold for APD alternans

To quantify the susceptibility to the repolarization alternnas, the pacing rate threshold for spatially concordant APD alternans and spatially discordant APD alternans were quantified. The threshold for the concordant alternans was significantly decreased in the infarction group relative to control (294 ± 27 bpm vs. 369 ± 25 bpm, $P < 0.001$). Similarly, the threshold for discordant alternans was also significantly decreased in the infarction group (366 ± 47 bpm vs. 458 ± 53 bpm, $P = 0.014$). Figure 18A shows APD alternans maps of an infracted heart (top row) and a control heart (bottom row) at multiple BCLs. Note that APD alternans starts to appear at a much slower BCL in the infarcted heart (210 ms or 286 bpm) compared with the control heart (150 ms or 400 bpm, at which more arrhythmogenic spatially discordant alternans started to occur in the infarcted heart). Figure 18B shows

50

sample optical AP traces from these two hearts at the BCL of 150 ms, where the APD

alternans was much more evident in the recording from infarcted heart compared with the
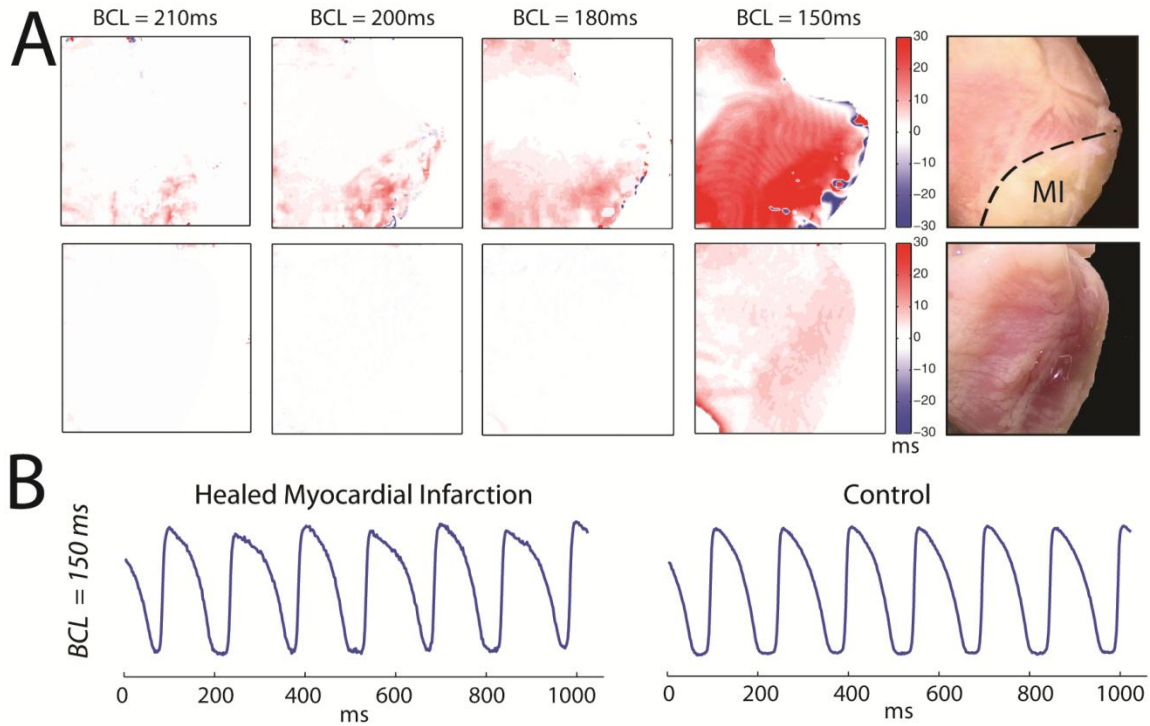
control.

Figure 18. *APD alternans maps and traces in control and in a heart with healed myocardial infarction. (A) APD alternans maps at basic cycle length (BCL) of 210 ms, 200 ms, 180 ms and 150 ms in a heart with healed myocardial infarction (top row) and in control heart (bottom row). The myocardial infarct (MI) is indicated in the a phtograph of the heart. The color indicates ⊿APD of two consecutive beats. (B) Sample action potential recordings from these two hearts at the BCL of 150 ms. It is evident that the alternans of action potential duration is much stronger in the recording from the infarcted heart (left) compared to the control (right).*

The susceptibility to repolarization alternans was not spatially homogeneous in both

infarction and control group. In the control hearts, the APD alternans consistently appeared

first in the left ventricle (Figure 19-top row with the solid black line indicating the location

of left anterior descending coronary artery). In comparison, in the hearts with healed

myocardial infarction, APD alternans appeared first in the infarct adjacent area or infarct

border zone (Figure 19-bottom row), suggesting myocytes close to the scar were more susceptible to repolarization alternans.
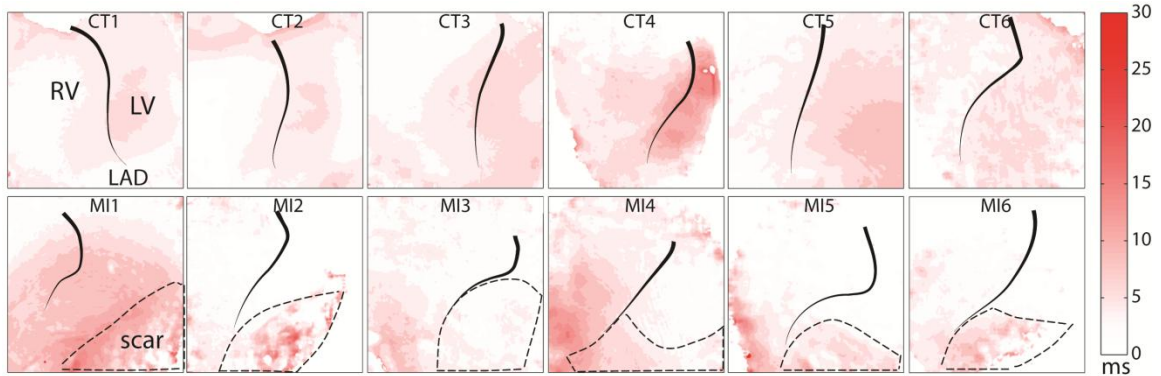
Figure 19. APD alternans map at the onset of alternans in 6 control hearts (CT1-CT6, top row) and 6 infarcted hearts (MI1-MI6, bottom row). The left anterior descending coronary artery (LAD) is indicated in every map. The scar area is circled by the dashed line.

4.4.2 Dynamic APD restitution and APD alternans

APD alternans occurs when the pacing rate is faster than a critical pacing rate. According to the restitution hypothesis, APD restitution curve determines the dynamic instability and predicts the critical pacing rate for APD alternans when its slope is equal to one. To test whether the APD restitution curve could precisely predict the actual critical pacing rate, we compared the predicted value with the measured value.

We found that the predicted pacing rate threshold for APD alternans was always higher than the actual pacing rate threshold for APD alternans, especially in the infarcted heart. Figure 20A is a representative plot with measurement of APDs and DIs of two consecutive beats (circles and squares) at multiple pacing rates from an infarcted heart. The circle and square are connected by a green line if they were neighboring beats from the same recording.

The increased APD alternans at increasing pacing rate is evident by the gradual separation of

the paired circle and square toward the bottom left corner of the plot. A close examination

of the plot revealed that the separation of paired circle and square (or the incidence of APD

alternans) starts at the cycle length of 230 ms (261 bpm).
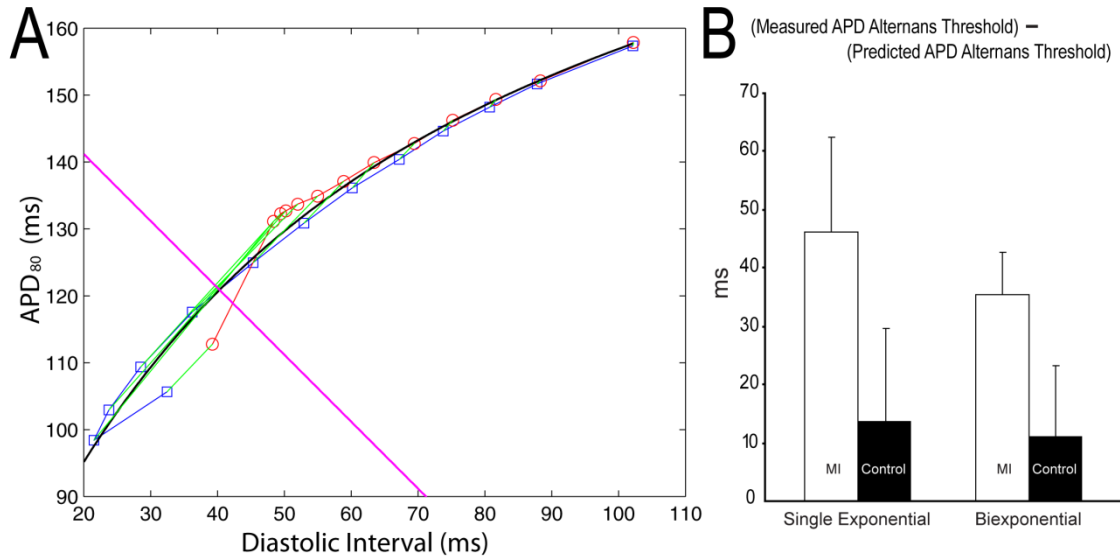
Figure 20. Inaccurate prediction of action potential duration (APD) alternans by dynamic APD restitution curve. (A) Dynamic APD restitution curve reconstructed from action potential recordings from one pixel of an infarcted heart. Measurement of APD and diastolic interval of two consecutive beats (red circle and blue square connected by a green line in the plot) at 13 different cycle lengths are plotted. The black line is the APD restitution curve reconstructed by a biexponential fitting. The purple line of slope -1 intersect with the APD restitution curve (black line) at a point where the slope is 1, and predict the alternans to occur beyond the cycle length of ~162ms. This prediction is much lower than the maximum of measured cycle length for APD alternans where the paired circle and square are not overlapped in the plot (230ms). (B) Summery of the measured APD alternans cycle length threshold minus predicted threshold from APD restitution curves reconstructed by a single exponential function (left) and a biexponential function.

Dynamic APD restitution curve (black line in Fig. 20A) was reconstructed by fitting the

measurements (circles and squares) using a biexponential function in Fig. 20A. The slope of

this dynamic restitution curve is equal to one at the crossing of the black line and the pink

line (slope of -1) in Fig. 20A, which is supposed to predict the onset of APD alternans at the

cycle length of 162 ms (370 bpm) according to the restitution hypothesis. Compared with

the measured threshold for APD alternans at 261 bpm, the predicted pacing rate threshold

for the onset of APD alternans is much higher than the actual value, suggesting APD

restitution alone does not predict the APD alternans. And this is especially true in the

infarction group (Fig. 20B).

4.4.3 Spatially Discordant Alternans
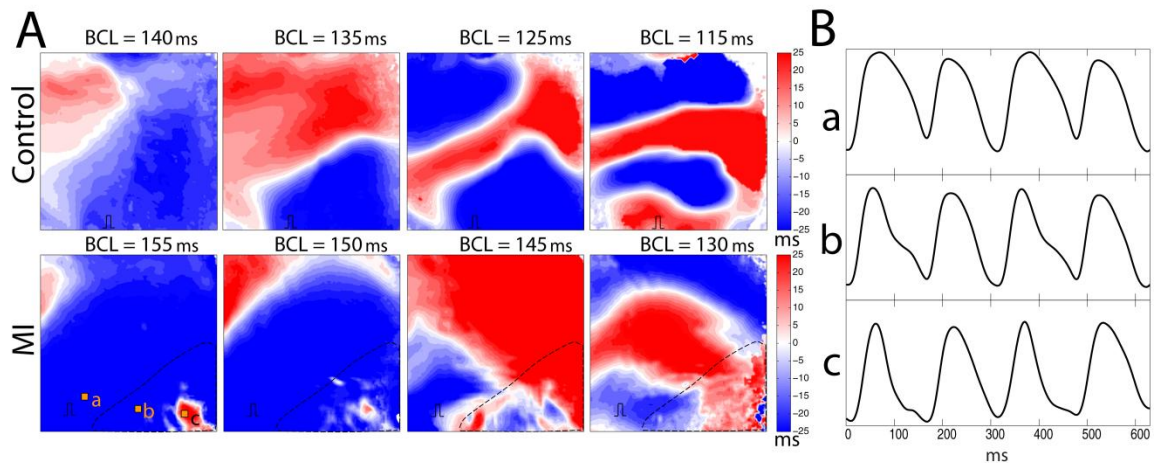
Figure 21. Dynamics of spatially discordant alternans. (A) APD alternans maps at multiple basic cycle lengths from a control heart (top row) and a heart with healed myocardial infarction (MI, bottom row). Pacing sites are indicated by a pulse square in each map. The myocardial infarct is circled by a black dashed line. The white nodal line (without APD alternans) separates regions of opposite sequence of APD alternans. (B) Representative action potential recordings from three locations a, b and c (indicated in the bottom-left map in panel A) from the infarcted heart.

Since dynamics of the nodal lines were shown to reflect the underlying mechanism of the

formation of spatially discordant alternans (111), we quantified the movement of nodal lines

in both control and infarcted heart. The top row in Figure 21A is a representative example

of the control heart. The nodal lines correspond to the white region in the APD alternans

maps. The first nodal line appeared close to the base of the right ventricle (i.e., the top-left

side of the map), and a second nodal line was later formed at a distal end from the pacing site. Both nodal lines gradually moved toward the apex as the pacing rate was increased. We consistently observed the movement of nodal lines towards the pacing site at increasing pacing rate, suggesting that engagement of CV restitution in the creation of spatially discordant alternans in the control heart (111, 176).

The bottom row of Figure 21A is a representative example of the infarcted heart. The myocardial infarct is circled by a dashed line. In the non-infarcted area, the behavior of the nodal line moves towards the pacing site and is very similar to the control heart. On the other hand, the dynamics of nodal lines appears to be different within the infarct border zone. Small islands with opposite sequence of alternans within the infarct border zone were observed (Fig. 21A-bottom row). These islands are small in size compared to that in non-infarcted area or in control heart. AP recordings within the island (site c), close to the island (site b), and far from the island (site a) are shown in Figure 21B. Close examination reveals that the odd beats are morphologically very different at these three sites while even beats are similar, indicating a different type of spatially discordant alternans compared with the those observed in control and noninfarcted region. In addition, close examination of these recordings suggests that the difference in the odd beats appears to result from the depression of the AP plateau in the infarct border zone (site c). As shown in the bottom row of Figure 21A, the island with out-of-phase alternans remained pinned in the same position as pacing rate increases, and gradually shrank and then disappeared. This unique island within the myocardial infarct region was observed in 3 out of 9 infracted hearts.

To further demonstrate the role of CV alternans in the induction of spatially discordant alternans, we quantified the activation CL alternans (representing the CV alternans) and

examined its temporal relation to the appearance of spatially discordant APD alternans in 2 infarcted hearts. We found that the alternans of activation CL preceded the alternans of SDA in these two hearts (Fig. 22). Top row in Figure 22 shows the maps of activation CL alternans and the bottom row of Figure 22 shows maps of APD alternans. Left column in Figure 22A&B are the maps created from data recorded immediately after increasing the pacing rate (0 min), and the right column are from data recorded 2 minutes later. In both examples, the regions with significant activation CL alternans at 0 min is the same region (blue region) where regions of opposite sequence of APD alternans appears at 2 min.
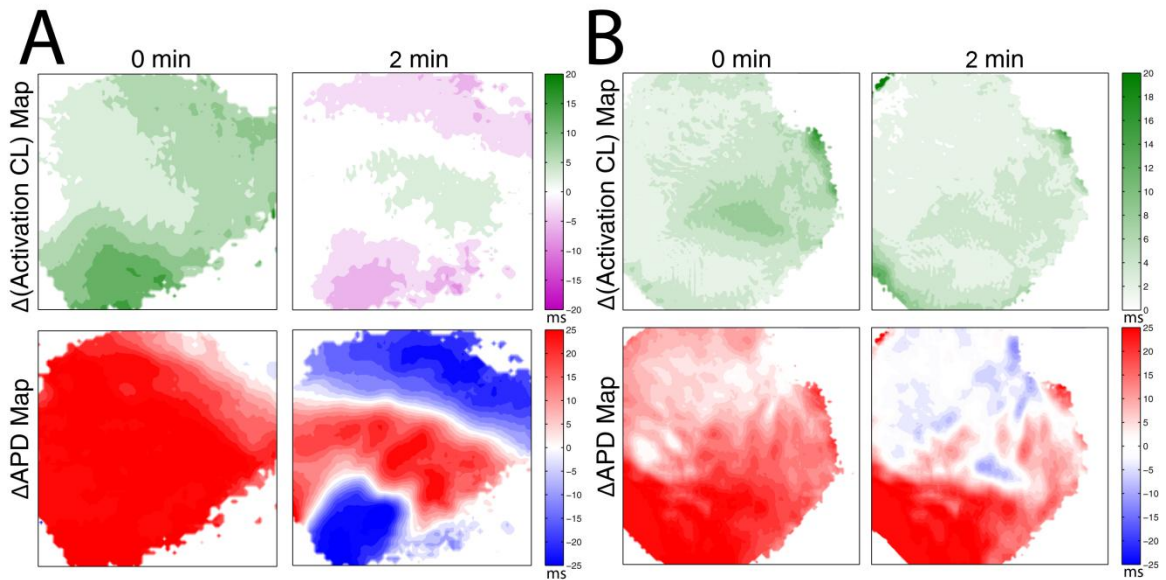
Figure 22. Activation cycle length alternans precedes the occurrence of APD alternans in the infarcted heart. (A) Activation cycle length (CL) map (top row) and APD alternans map (bottom row) immediately after the shortening of CL (0 min, left column) and 2 min after (right column). It can be seen that the region with strongest alternans in the activation CL map at 0 min (the up-left map) corresponds to the blue area in the APD alternans map at 2 min (the bottom-right map). (B) Example from another infarcted heart, which showed similar phenomenon as in panel A.

4.5 Discussion

In the present study, we quantified the susceptibility to APD alternans in a rabbit model of healed myocardial infarction. The pacing rate threshold for APD alternans was significantly decreased for both spatially concordant and discordant alternans in the infarcted heart. This enhancement was most significant in the infarct border zone. Dynamic APD restitution could not predict the increased dynamic instability in the infarcted heart. Conduction velocity alternans plays an important role in producing spatially discordant alternans in both control and infarction group, while some unknown mechanism is responsible for a distinct pattern of spatially discordant alternans within the infarct border zone.

4.5.1 Mechanism of APD Alternans

Steep APD restitution was hypothesized to produce APD alteranns (193). If APD is solely dependent on the preceding DI, APD alternans should start at the cycle length at which the APD restitution slope is equal to one. APD restitution has been quantified in canine heart with healed myocardial infarction (196) and patient with structural heart disease (SHD) (128), 45% of which had old myocardial infarction. Ohara et al. (196) found that the DI range over which the dynamic restitution slope > 1 is significantly increased in the endocardial infarction border zone in the infarction group compared to the control group. Koller et al. (128) found a significantly earlier onset of alternans of monophasic APs in patients with SHD compared with patients without SHD.

   This hypothesis is not confirmed in the present study because APD alternans occurred at a much slower heart rate than that predicted by the APD restitution, especially in the infarction group. This incapability of APD restitution in predicting APD alternans was also

observed in other studies (121, 212, 242), suggesting other mechanisms responsible for the induction of APD alternans. In isolated rabbit myocyte, Chudin et al. showed that the calcium transient alternans was not affected by the clamping the voltage with AP of fixed duration (43), suggesting the calcium transient alternans as the driving force for APD alternans via calcium-dependent ionic currents. The key role of calcium handling in alternans has been implicated in other experimental studies (91, 137, 212).

The remodeling of calcium handling in the presence of healed myocardial infarction has been described in several studies. Litwin et al. showed that (155) the rising time and declining time were significantly prolonged in the rats 6 weeks post myocardial infarction. Mackiewicz (165) showed moderate decrease of decay rate of calcium transient in rats with 3 months post myocardial infarction, which suggest moderate functional change of sarcoplasmic reticulum calcium ATPase (SERCA) and sodium/calcium exchanger (NCX). However, Andriy et al. (13) did not observe any change on the calcium uptake by SERCA and calcium transport by NCX in the myocytes from dog with more than 4 weeks myocaridal infarct. They found that pacing rate threshold of APD alternans and calcium transient alternans was significantly reduced, and they attributed the decreased alternans threshold to leaky ryanodine receptors due to steeper dependence of sarcoplasmic reticulum (SR) calcium release on the SR calcium content.

4.5.2 Mechanism of Spatially Discordant Alternans

Spatially discordant alternans describes the presence of out-of-phase APD in neighboring regions and a large APD gradient across the nodal lines. Spatially discordant alternans increases the dispersion of repolarization and was observed to precede the induction of ventricular arrhythmias (130, 200). Computer simulations (216, 257) and an experimental

study (53) have shown that spatially discordant alternans could be induced in spatially homogeneous tissue through the interactions of APD restitution and CV restitution. In addition, it was suggested that functional heterogeneity (111, 257) and structural heterogeneity (59, 201) might facilitate the formation of spatially discordant alternans. it was not unclear whether dynamic or functional/structural heterogeneity is the dominant mechanism for the formation of spatially discordant alternans in the presence of healed myocardial infarction.

We showed that the pacing rate threshold for the spatially discordant alternans was decreased in the rabbit heart with healed myocardial infarction. This is in line with the decreased alternans threshold in the rabbit heart with structural barriers created by laser epicardial lesions (201), suggesting the cellular uncoupling as one of the underlying mechanisms for spatially discordant alternans. The tissue discontinuities caused by the cellular uncoupling were known to produce abnormal conduction velocity restitution (59), which could underlie the induction of spatially discordant alternans as shown in computer simulations (216). The dynamics of the nodal lines in the noninfarct region in our study indicated the CV alternans as the cause of the spatially discordant alternans. The underlying mechanism of the distinct island of spatially discordant alternans within the infarct border zone remains to be investigated. It might be explained by fibrolast-myocyte coupling which was shown to promote alternans at a slower heart rate (266) and by reduced electronic effects which was shown to facilitate alternans (41).

4.6 Limitations

Despite that the pacing rate of pacing rate threshold in the heart with healed myocardial infarction was significantly compared with control, it remains higher than the regular heart rate of the rabbit. However, this pacing rate threshold for alternans might be lower in vivo and become close to the range of regular heart rate, because denervation in ex-vivo condition could decrease the level of adrenergic stimulation and thus reduce the incidence of APD alternans (52, 101). This hypothesis remains to be tested in future.

Another limitation is that only epicardial action potential were measured in the present study. It remains unknown whether the increased cellular uncoupling in the infarct border zone could promote transmurally discordant alternans at relatively slow heart rate.

We did not test other mechanisms that might promote the induction of arrhythmia in the presence of healed myocardial infarction. It remains to be determined how important the enhanced APD alternans due to myocardial infarction contribute to the arrhythmogenesis in vivo. To avoid a lengthy protocol, only dynamic pacing protocol was used. It is possible that single or multiple premature stimuli could produce significant APD alternans that might be responsible for the arrhythmogenesis in the infarcted heart (138, 139). Furthermore, blebbistatin was used to abolish the contraction to remove the motion artifact. It remains to be determined how the stretch at the boundary between viable tissue and non-contracting scar during contraction could contribute to the alternans of repolarization.

5. Remodeling and Dispersion of Repolarization in the Right Ventricle of Failing Human Heart

5.1 Abstract

Increased dispersion of repolarization was suggested to underlie the increased arrhythmogenesis in human heart failure (HF). However, we have recently found no evidence of increase in left ventricular transmural dispersion of repolarization in the failing human heart. In this study, we sought to determine whether dispersion of repolarization was enhanced across the endocardium of the right ventricle (RV) of the failing versus non-failing human heart.

  RV free wall preparations were dissected from five failing and five nonfailing human hearts, cannulated and coronary-perfused. Optical mapping was conducted at the endocardium from a ~6.3 × 6.3 cm field of view. Action potential duration (APD), dispersion of APD, and conduction velocity (CV) were quantified for the basic cycle length ranging from the refractory period to 2000 ms. APD was significantly prolonged in the failing group as compared to the nonfailing group. Dispersion of APD was significantly increased in only three failing hearts. APD alternans was induced by rapid pacing only in these three failing hearts. CV was significantly slower in the failing group than in the nonfailing group. Arrhythmia was induced only in two failing hearts, which had an abnormally wide cycle-length range with steep CV restitution and were among the three hearts with increased dispersion of repolarization.

In conclusion, dispersion of repolarization could be enhanced due to heterogeneous prolongation of APD, enhanced APD alternans, and slower conduction in failing human heart. Arrhythmia in the failing human heart was closely associated with increased dispersion of APD, APD alternans, and abnormally steep CV restitution.

5.2 Introduction

Ventricular arrhythmia is common in patients with heart failure (HF) (83, 171). It significantly increases the risk of sudden cardiac death (171, 210), which accounts for more than half of the congestive HF-related deaths (83). Our limited understanding of mechanisms of arrhythmogenesis confined our ability to obviate the risk of sudden cardiac death of patients with HF.

Remodeling and dispersion of repolarization play important roles in arrhythmogenesis. Dispersion of repolarization represents the heterogeneous recovery of excitability in neighboring myocytes. Enhanced dispersion of repolarization increases the vulnerable window for unidirectional block by a single premature beat (217), and increases the likelihood of arrhythmia (5). Compelling experimental evidence has demonstrated the correlation between the enhanced dispersion of repolarization and increased susceptibility to arrhythmia (69, 93, 100, 134, 248). Clinical studies have also shown strong links between dispersion of QT interval (reflecting dispersion of repolarization (270)) and ventricular tachyarrhythmia in patient with HF (9, 86, 209). Since the action potential duration (APD) is mainly responsible for the repolarization, changes in APD reflect the remodeling of repolarization. An important question is how HF affects the regional differences in APD

(243). The answer to this question could help identify the origin of the increased dispersion of repolarization and the potential target for clinical intervention in HF patients.

Akar et al. demonstrated that heterogeneous prolongation of left ventricular APD caused increased dispersion of repolarization and arrhythmia in a dog model of tachypacing-induced HF (3). They found that transmural dispersion of repolarization was markedly augmented in the failing dog heart due to more pronounced prolongation of action potential (AP) at the mid-myocardial and endocardial layers. Enhanced ventricular transmural dispersion of repolarization was also observed in other animal models of heart diseases and closely associated with the development of reentrant arrhythmias (5).

Thus a number of animal models of HF provided evidence of mechanistic link between the enhanced transmural APD dispersion and increased arrhythmogenesis. Recently we used optical mapping to investigate APD dispersion in the failing human left ventricle (89). In contrast to previous findings in animal models of HF, we found no evidence of enhanced APD dispersion in the failing human left ventricle. On the contrary, we found that despite overall increase in APD, the transmural dispersion of repolarization was surprisingly reduced in the failing human heart (89). This reduction of transmural dispersion of repolarization was also observed in a mouse model of pressure-overload HF (253), in a study of a dog model of tachypacing-induced HF (146), and was confirmed in a more recent study of excitation-contraction coupling in the failing human heart (159).

It has been shown that the dispersion of endocardial repolarization of right ventricle (RV) could be enhanced in patients with sustained ventricular tachycardia (179) and in patients with long QT syndrome (26). We hypothesized that RV endocardium undergoes remodeling

during HF, which increased dispersion of repolarization, prolongs APD, and slows the conduction velocity (CV). All these three changes could contribute to increased propensity to arrhythmia. To test this hypothesis we applied optical mapping of action potentials at a large area of RV endocardium, 63 mm by 63 mm. Then we quantified the dispersion of APD, and restitution properties of both APD and CV. Arrhythmia inducibility was tested using rapid pacing.

5.3 Methods

The protocol of the study was approved by the Washington University Institutional Review Board. Failing human hearts were obtained during transplantation from Barnes-Jewish Hospital of Washington University in St. Louis, MO. Donor hearts were provided by Mid-America Transplant Service (St. Louis, MO) and used as the nonfailing group. Both failing (n = 5) and nonfailing (n = 5) human hearts were optically mapped. Patient information is shown in Table 1.

Explanted hearts were cardioplegically arrested. Details of tissue harvest, vessel ligation, and coronary perfusion can be found in our previous publications (89, 159). During dissection, entire RV free wall was isolated and cannulated at the origin of the right coronary artery. Care was taken so that the tissues were not stretched when they were pinned down onto a silicon sheet. Tissue was immobilized by 10~20 μM blebbistatin to suppress the motion artifacts in optical recordings. Optical APs were recorded from the majority of RV endocardium (63 ± 7 mm by 63 ± 7 mm). We did not map the epicardium because the entire epicardium of the failing human heart was often covered by a layer of fat which prevented the recording of optical signals.

Table 1. Patient Information

# Group	Gender	Age	Diagnosis
1 Failing	Male	53	Non-ischemic Cardiomyopathy
2 Failing	Male	55	Ischemic Cardiomyopahty
3 Failing	Female	67	Non-ischemic cardiomyopathy
4 Failing	Male	59	Non-ischemic cardiomyopathy
5 Failing	Female	53	Non-ischemic Cardiomyopathy
6 Nonfailing	Female	51	Cerebrovascular/Strock
7 Nonfailing	Male	31	Gunshot wound to the head
8 Nonfailing	Male	40	Head Trauma, Motor Vehicle Accident
9 Nonfailing	Female	59	Cerebrovascular/Stroke
10 Nonfailing	Male	76	Cerebrovascular/Stroke

In order to measure the dynamics of dispersion of repolarization at different cycle lengths, we stimulated the isolated RV using steady-state pacing. We commenced pacing at a cycle length (CL) of 2000 ms, and then gradually decreased CL until reaching refractory period or arrhythmia was induced. All the preparations were stimulated at the bottom of the field of view (close to the apex) at the voltage double the pacing threshold. Figure 23 shows a representative RV preparation and AP recordings from a nonfailing human heart. The APD was the duration from the upstroke (maximum derivative of the signal) to the 80% repolarization (APD80), and was measured at all recording sites. Global CV across the field

of view was also quantified at different cycle lengths. Dispersion of APD was quantified by the difference between 95th percentile and 5th percentile of APD80 from all the recorded sites. Dispersion of repolarization depends on both activation time difference and APD difference. Since the activation time differences during pacing and during sinus rhythm are not the same, only the dispersion of APD was quantified to study the changes in the dispersion of repolarization.

Comparison was made between failing group and nonfailing group. Levels of significance were determined by the Student's paired or unpaired t-test. Bonferroni adjustment was used to account for multiple comparisons. $P<0.05$ was considered statistically significant. Values were given as means $\pm$ S.D.
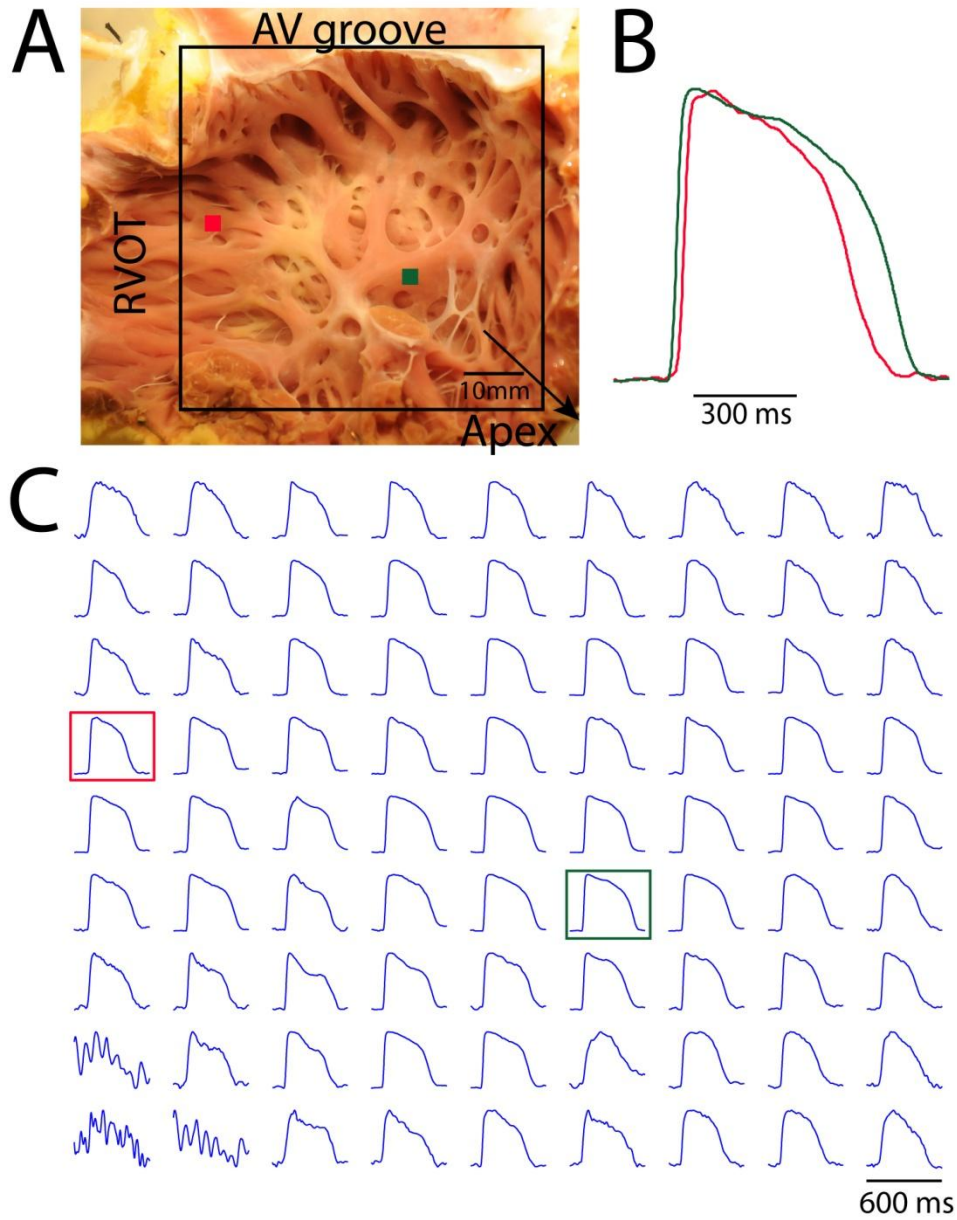
Figure 23. Representative RV free wall preparation and optical action potentials (AP). (A) RV free wall preparation and mapping field of view (FOV). (B) Close-up view of two action potential recordings. (C) Representative optical action potentials from an evenly spaced array of locations spanning the whole FOV. Red and green dots in panel A and squares in panel C correspond to recordings in panel B.

5.4 Results

5.4.1 Action Potentials in Failing Human RV

Figure 24 shows AP recordings of five failing hearts (blue traces) and five nonfailing hearts (red traces) at the basic CL of 2000 ms. Three different columns of recordings are representative maximum APD, mean APD, and minimum APD, respectively. It can be seen that APD was longer in the failing group, especially for the maximum APD. The prolongation of APD could be associated with slower repolarization of APD (e.g., maximum APD of failing heart #1), or longer plateau of AP (e.g., maximum APD of failing heart #5). Furthermore, there existed heterogeneity of APD at the RV endocardium, as evident from the different duration of APs between the left column and the right column in Figure 24.
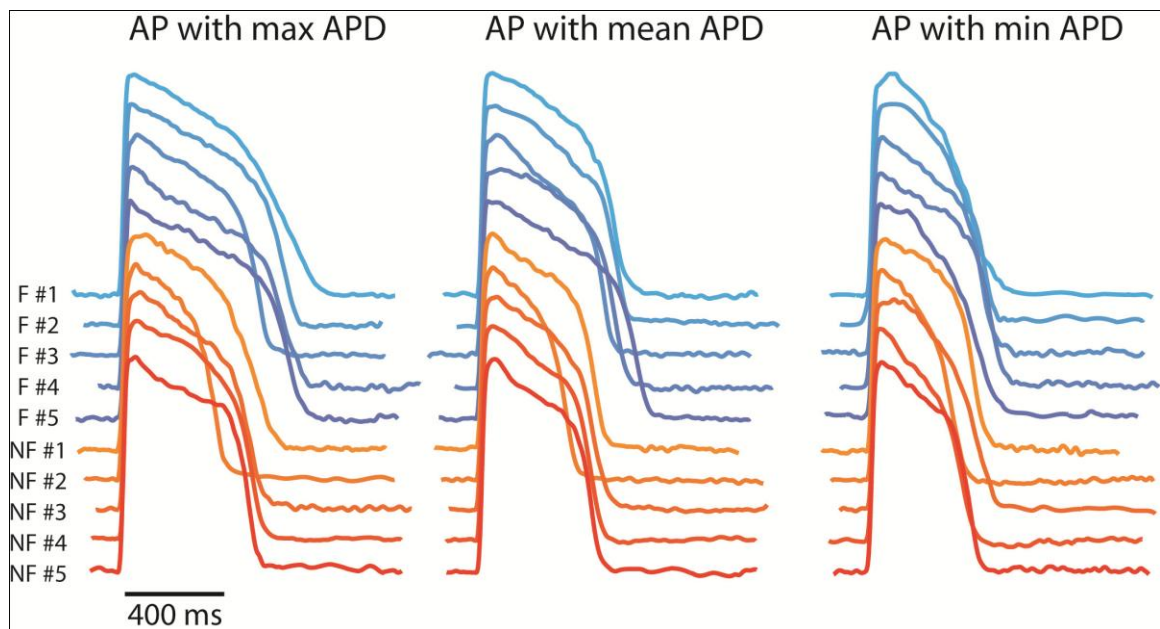
Figure 24. Representative action potential (AP) recordings from individual failing (n=5, blue traces) and nonfailing (n=5, red traces) human hearts at the pacing cycle length of 2000ms. On the left, the AP recordings with the maximum APD in the field of view (FOV). In the middle, the AP recordings with the mean APD in the FOV. On the right, the AP recordings with the minimum APD in the FOV.

68

Quantitative measurements of APD is shown in Figure 25. Figure 25-left shows APDs at

multiple CLs for all 10 hearts. Blue and red curves correspond to five failing hearts and five

nonfailing hearts respectively. The visual separation of the blue curves and red curves

indicates that APDs of the failing group were different from and significantly longer than the

nonfailing group. This difference was indeed statistically significant as shown in the Figure

25-right.
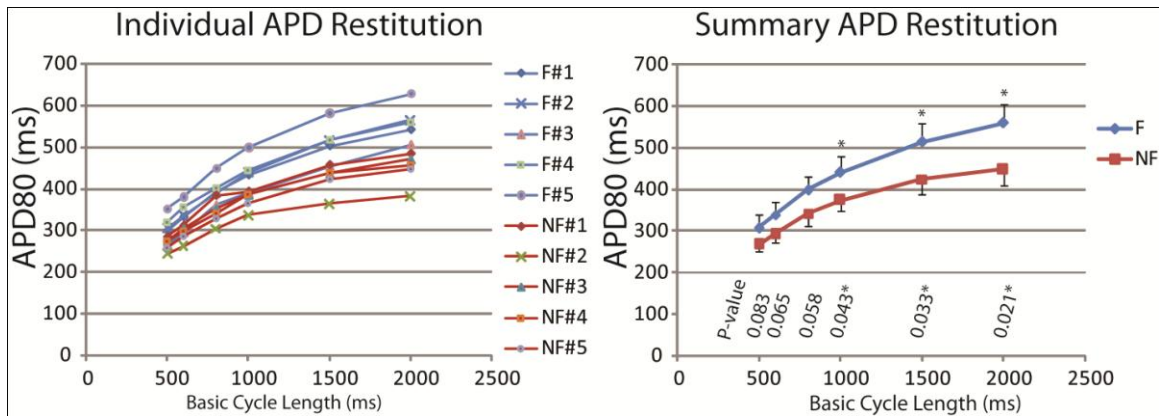
*Figure 25. Individual APD restitution and summary APD restitution. On the left, APD at 80%
repolarization (APD80) at various basic cycle lengths from 500ms to 2000ms from failing (blue lines) and
nonfailing (red lines) human hearts. On the right, averaged APD80 of failing and nonfailing hearts, and P-
values for each comparison between failing and nonfailing groups.*

5.4.2 Dispersion of Repolarization

One of the main goals of this study was to determine whether dispersion of APD was

enhanced in the RV endocardium of failing human heart. We did observe dramatically

increased dispersion of APD in the RV endocardium in three out of five failing hearts.

Figure 26 shows one example from a failing heart (Fig. 26-top row) and one example from a

nonfailing heart (Fig. 26-bottom row). Figure 26-left shows activation maps where we can

see that the waves propagated from the bottom to the top of the field of view in both

examples. Figure 26-middle is the APD map, where APDs were color-coded within the same range of color map for both preparations. The APDs in the failing heart span from 420ms to 640ms, the range of which is much larger than the range in the nonfailing heart (400ms to 530ms). There was an apparent association between the APD heterogeneity and the structures of fiber bundles and trabeculae carneae at the RV endocardium, as shown in Figure 26-right.
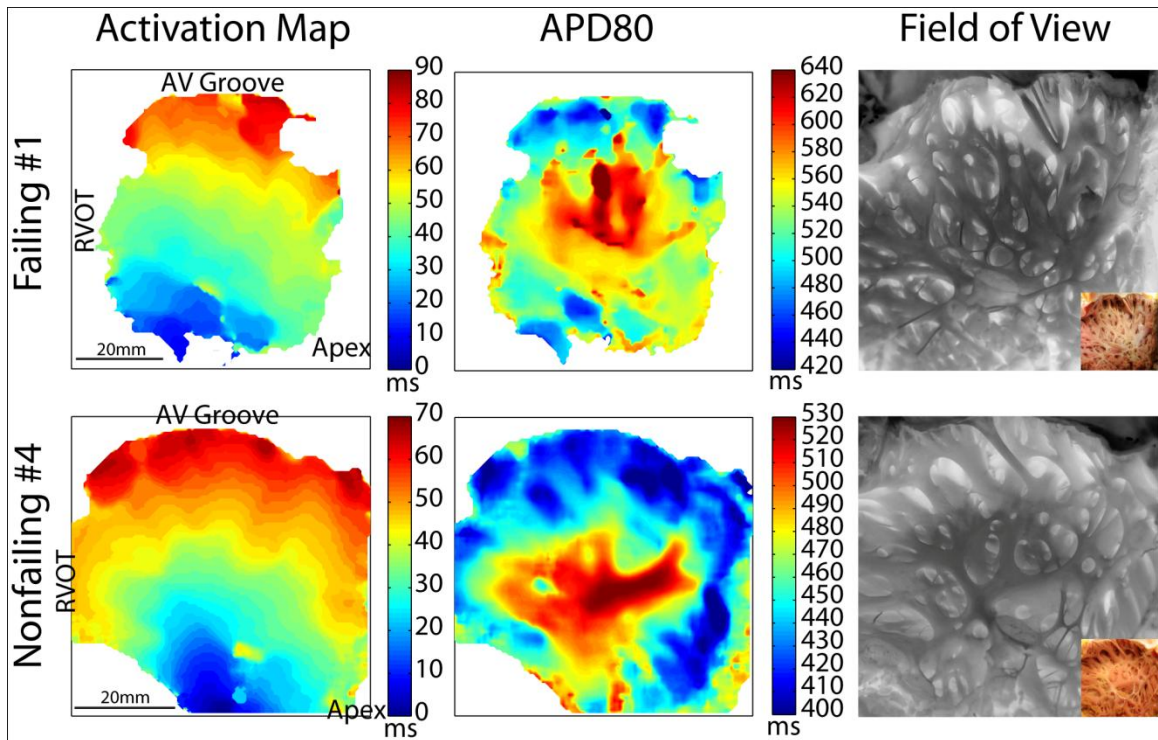
Figure 26. Representative examples of dispersion of repolarization at the endocardium of RV freewall from a failing heart and a nonfailing heart at the pacing cycle length of 2000ms. On the left, maps of activation (from blue to red) after a stimulus at the bottom of the field of view. In the middle, maps of APD80. It can be seen that the range of APD80 is much larger in the example of the failing heart (the top row) compared with that of the nonfailing heart (the bottom row). This indicates the dispersion of repolarization was enhanced in this failing heart. On the right, field of view with inverted color for better visualization of the structure.

We quantified the dispersion of APD by measuring the difference between 95th and 5th percentiles of APD in the mapped area. Figure 27-left showed dispersion of APD in all 10 hearts at multiple cycle lengths, with blue curves indicating failing hearts and red curves indicating nonfailing hearts. It can be seen that three blue curves corresponding to three failing hearts (#1, #2, #5) are separated from all the other curves, suggesting increased dispersion of APD in these three hearts. The increased dispersion of APD is due to heterogeneous prolongation of APD. The other two failing hearts did not have increased dispersion of APD, and their corresponding blue curves were clustered together with the nonfailing hearts (Figure 27-left). Due to the variations in different failing human hearts, the overall dispersion of APD in the failing group was not significantly different from the nonfailing group (Figure 27-right).
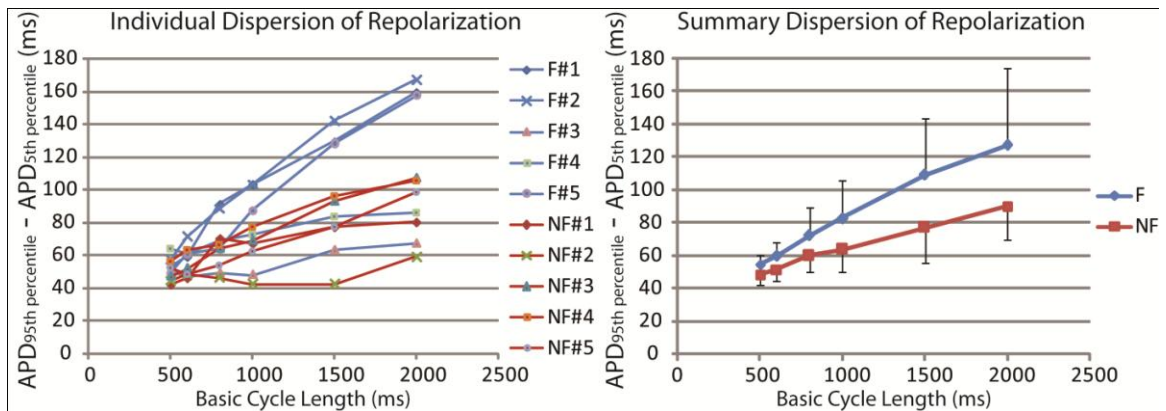
Figure 27. Dispersion of repolarization quantified by APD80 at 95th percentile minus APD80 at 5th percentile. On the left, dispersion of repolarization at various basic cycle lengths from 500ms to 2000ms from failing (blue lines) and nonfailing (red lines) human hearts. On the right, averaged dispersion of repolarization within failing and nonfailing groups. It can be seen from the left panel that three failing hearts (#1, #2, #5) stand out from the other hearts by showing significant enhancement of dispersion of repolarization.

Interestingly, APD alternans were induced by rapid pacing only in those three failing hearts with large APD dispersion (failing hearts #1, #2, #5), and occurred in regions with the maximum APD prolongation. The pacing rate at the onset of APD alternans was 164 ± 12 bpm. These APD alternans could increase the dispersion of repolarization at fast heart rate, and provide the substrate for the initiation of arrhythmia, which was induced in failing heart #2 and #5. No alternans were observed in the other 2 failing and 5 non-failing hearts.

5.4.3 Dynamics of Conduction Velocity

The CV restitution for all individual hearts was shown in Figure 28-left. CV was significantly smaller in the failing group than the nonfailing group (Figure 28-right). In all the nonfailing hearts and three failing hearts, as we gradually decreased the pacing cycle length, the CV remained constant until the basic cycle length approached the refractory period. In contrast, the CV decreased progressively, starting at a much longer basic cycle length (1000ms) in two failing human hearts (failing hearts #2 and #5, Figure 28-left). As a result, the CV restitution for these two hearts had a much wider range of pacing CL with steep CV restitution than all the other curves. It was only in these two failing hearts that arrhythmia was induced. In addition, these two hearts were among the three hearts, which had enhanced dispersion of APD.
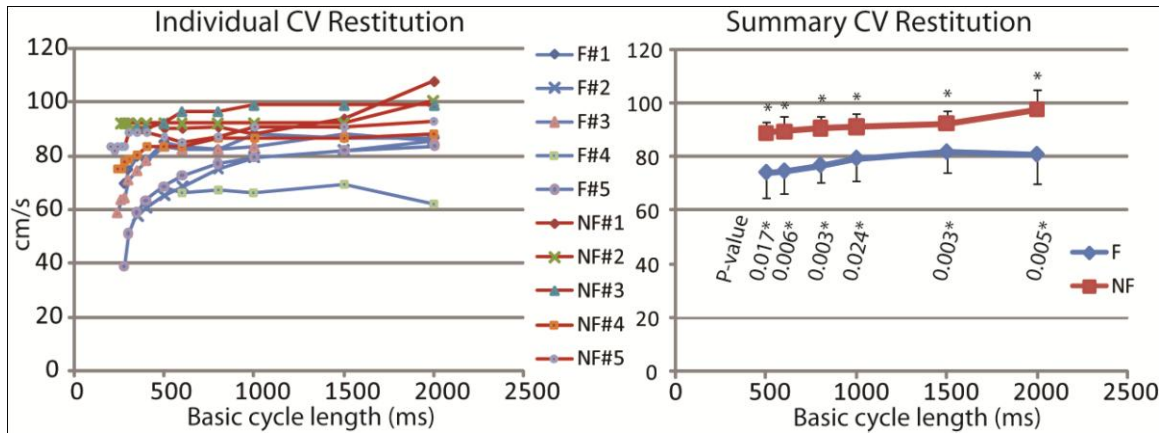
Figure 28. Conduction velocity (CV) restitution. On the left, individual CV restitution from failing (blue lines) and nonfailing (red lines) human hearts. On the right, averaged CV restitution. Since not every heart was paced faster than BCL of 500ms, CV was only averaged for BCL from 500ms to 2000ms. Note that the CV was significantly decreased in the failing hearts. Also note that CV restitutions in failing hearts #2 and #5 have nonflat slope over a much wider range of basic cycle length.

5.4.4 Induction of Arrhythmia by Rapid Pacing

How the arrhythmia was initiated by rapid pacing in a failing human heart (#2) is illustrated in Figure 29, which shows the transition from paced beats to arrhythmia. Figure 29A shows the activation maps for beats 7, 8, 10, 11 and 12 and a dominant frequency map during the arrhythmia, which was initiated at beat 12. Figure 29B are the AP recordings from 4 different sites *a*, *b*, *c* and *d*, which are marked in the top-left activation map in Figure 29A. As described in the previous section, we observed in this heart APD alternans, which is evident from sites *b*, *c* and *d*. Dispersion of repolarization is increased due to dyssynchrony of APD alternans in different regions (i.e., no APD alternans in site *a*, 2:2 APD alternans in site *b*, and 3:3 APD alternans in sites *c* and *d*). The increased dispersion of repolarization due to alternans provided the substrate for arrhythmia. There were recurrent ectopic beats at site *c* (every three beats as marked by * in Figure 29B), which provided triggers for the induction

of arrhythmia. Arrhythmia was induced at beat 12 (marked by # in Figure 29B) due to an

early arrival of an ectopic beats at site *c*.
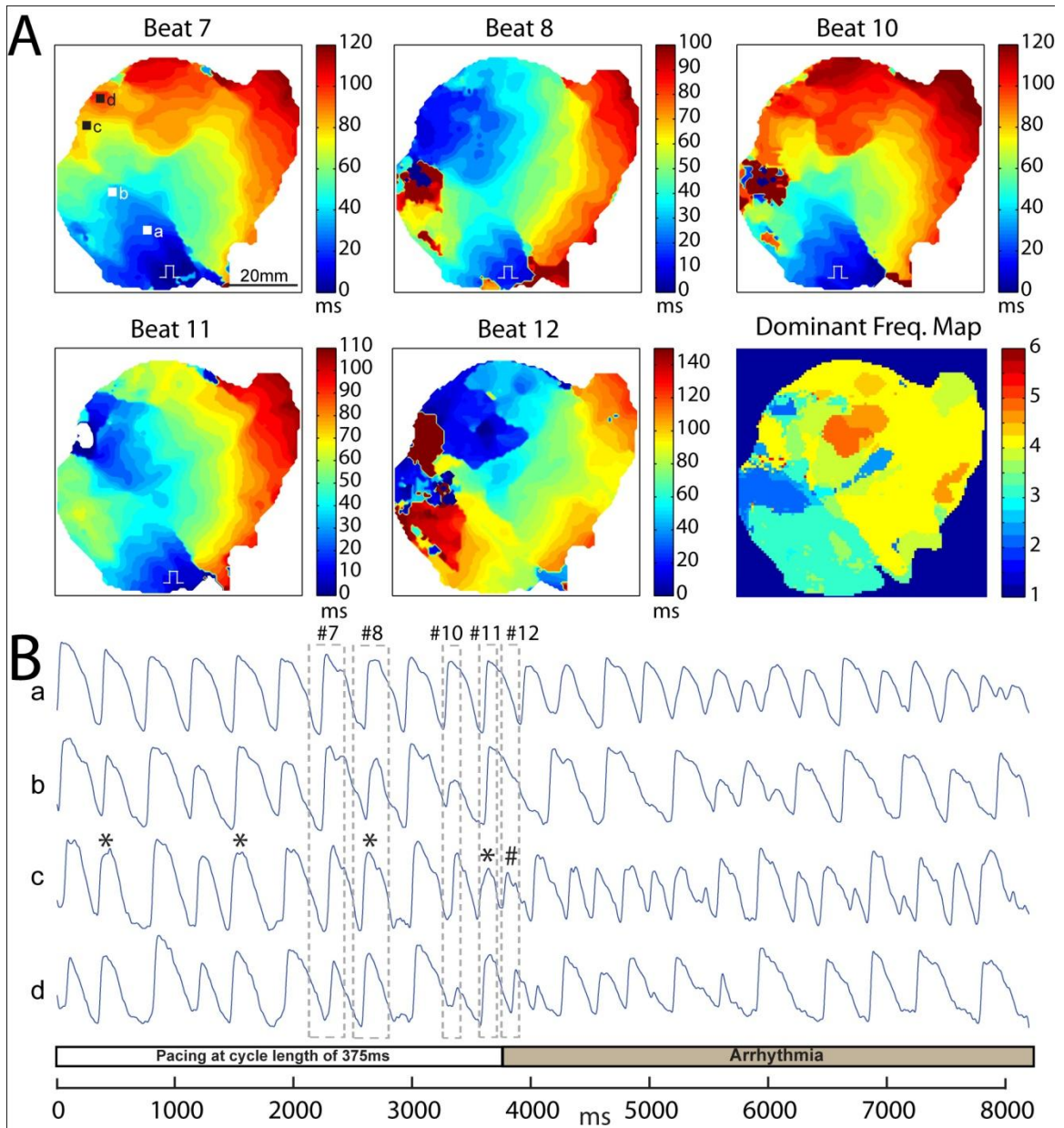
Figure 29. Arrhythmia induced by rapid pacing in failing heart #2. (A) The induction of arrhythmia is showed by sequential activation maps of beat 7 to beat 12. The dominant frequency map of the first 5 seconds of the arrhythmia is also shown. (B) Action potential recordings from four sites a, b, c and d. Asterisks (*) indicate activation were initiated by both the stimulus (square wave) at the bottom and a foci at the site c (See beat 8 and 10 in panel A). Arrhythmia is induced by a early activation at site c at Beat 12(marked by #). Large dispersion of repolarization resulted from APD alternans, which are obvious in traces b, c and d.

5.5 Discussion

In this study, we examined the remodeling and dispersion of repolarization in the RV endocardium using optical mapping of APs in a relatively large field of view. The major findings in this study include that (i) APD was significantly increased in the RV endocardium of the failing group compared to the nonfailing group, (ii) dispersion of APD was significantly enhanced in three out of five failing hearts, (iii) APD alternans was induced in those same three failing hearts with enhanced dispersion of APD, but not in the other two failing hearts, (iv) endocardial CV was significantly reduced in the failing group compared with the nonfailing group, and (v) ventricular arrhythmias were induced in failing hearts (#2 and #5), which had enhanced dispersion of APD, APD alternans, and abnormal CV restitution.

5.5.1 Prolongation of APD in Human Heart Failure

APD prolongation has been consistently observed in various animal models of heart failure in both isolated cells and tissues, and has been reviewed previously (243). Compared with animal models of HF, human studies of APD remodeling in heart failure are rather limited and mostly in the isolated cells (19, 21, 131, 147) or isolated small-sized RV trabeculae (94, 250), where spatial heterogeneity was not studied. We have recently explored transmural heterogeneity in the human LV wedge preparations and found that prolongation of APD was only observed at the epicardium but not the endocardium and midmyocardium (89). In contrast to the absence of APD prolongation in the LV endocardium (89), prolongation of APD was a consistent phenomenon in the RV endocardium in this study. It should be noted that this prolongation was heterogeneous in three failing hearts, leading to increased dispersion of APD. This spatial heterogeneity in APD prolongation suggests that the

location of tissue biopsy should be an independent variable in interpreting and comparing data from studies of isolated cells from the RV endocardium. It is likely that this spatial heterogeneity might also exist across RV epicardium, LV endocardium, and LV epicardium. This heterogeneity across the endocardium or epicardium has been implicated in several *in vivo* studies in patients and animal models of various heart diseases (26, 135, 179, 198, 248).

Based on previous studies of isolated human ventricular myocytes, the prolongation of APD could result from the down-regulation of transient outward K$^+$ current ($I$to) (19, 187, 263), down-regulation of inward rectifier K$^+$ current (I_{K1}) (131), and slow delayed rectifier K$^+$ current (I_{KS}) (256). Since most studies focused on the transmural heterogeneity, it remains to be determined why the prolongation of APD in the RV endocardium is spatially heterogeneous. Li et al. (147) provided some insights in a study of isolated cells from the RV epicardium from failing human heart. They showed that reduced $I$to, I_{K1}, and I_{KS} in the cells from tissues with fibrosis and necrosis lead to significantly longer APDs in these cells than cells from tissues without histological abnormalities (147).

Prolonged duration increases the lability of AP, and could increase the susceptibility to secondary depolarization, such as early after-depolarization (EAD) or delayed after-depolarization (DAD). No EAD was observed in failing hearts or nonfailing hearts in the present study. The only possible DAD observed in this study is the apparent ectopic beats during rapid pacing in one failing human heart, as shown in Figure 29. However, because the tissue is three dimensional, the apparent ectopic beats could also be explained as a breakthrough from a transmural conduction. The resistance to EAD and DAD even in the failing hearts is similar to the observation by Vermeulen et al. (250), who showed that when isolated RV trebeculae from failing human hearts was perfused with normal Tyrode's

76

solution, no DAD and EAD could be induced. They also showed that when the tissue was perfused with modified Tyrode's solution (mimic the extracellular milieu of patients with severe HF), DAD but not EAD was observed (250). The presence and underlying mechanism for DAD and EAD in HF patients remains to be determined in future studies.

5.5.2 Dispersion of Repolarization in Human Heart Failure

Increased QT dispersion in HF patients (9, 86, 209) suggested the existence of exaggerated dispersion of repolarization, which may predispose to ventricular arrhythmia (69, 93, 100, 134, 248). While increased transmural repolarization heterogeneity was consistently not observed in the LV of failing human heart (89, 159), we demonstrated in this study that dispersion of APD could be enhanced in the RV endocardium (Figure 27-left) in three failing hearts. Increased dispersion of APD in these failing human hearts reflected the heterogeneous prolongation of APD, and could contribute to the increased dispersion of repolarization. It is true that the enhanced dispersion in the failing hearts was most significant at nonphysiologically slow rates, and approached the nonfailing hearts at more physiological rates. However, pauses after premature beats are common in HF patients and may produce significantly large dispersion at physiological heart rates (243).

 The dispersion of repolarization could also be enhanced by the APD alternans. Pastore et al. (200) showed that spatially discordant APD alternans (i.e., out-of-phase APD alternans at different regions of the heart) resulted in a large dispersion of repolarization, which promoted initiation of arrhythmia. The presence of discordant APD alternans preceding the induction of arrhythmia in Figure 29 supports the causal relationship between APD alternans and arrhythmia. It is intriguing that enhanced dispersion of APD and APD alternans occurred in the same failing hearts in this study. This association has been

implicated in an *in vivo* patient study by Chauhan et al. (38), who showed that dispersion of activation-recovery interval was higher in patients with T-wave alternans.

5.5.3 Remodeling of Conduction Velocity and Arrhythmia

We observed significantly decreased CV in the RV endocardium of the failing human heart. Since decreased cellular coupling occurs in the ischemic and hypertrophied human heart (202) and the failing human heart (89), this reduced cell-to-cell coupling might be responsible for the reduced CV in this study. Normal intercellular coupling allows electrotonic currents, which reduced the heterogeneity of APD between neighboring cells. The reduced coupling could decrease the electrotonic effects and increase the heterogeneity of repolarization. It could also promote the incidence of APD alternans (41).

  Abnormal CV restitution has been shown to contribute to the susceptibility to arrhythmia (36, 216, 228). This correlation is consistent with our observation that arrhythmia was only induced when the CV restitution had a wide range of cycle length at which the restitution curve was steep (failing heart #2 an d #5 in Figure 28A). According to a computer simulation study by Qu et al. (216), in order to produce spatially discordant alternans and subsequent induction of arrhythmia, pacing rate needs to be fast enough to engage the steep portion of CV restitution. A wider steep portion of CV restitution allows this engagement to occur at a slower pacing rate and therefore increases the likelihood of arrhythmia. This abnormal CV restitution has been previously reported in the failing human hearts by Kawara et al. (123), and was found to be closely associated with stringy and patchy fibrosis (123). Derksen et al. (59) further showed that delayed inactivation of depolarizing currents at tissue discontinuities contributed to the abnormal CV restitution.

5.5.4 Variability in Human Heart Failure

In this study, while the RV endocardium from failing hearts shared similar functional remodeling (e.g., prolongation of APD), there clearly was significant variability. We did not observe increased dispersion of repolarization, alternans, and abnormal CV in two out of five failing hearts. Even the consistently observed prolongation of APD appears to have different mechanisms in different hearts (Figure 24), because the prolongation was due to a slow repolarization phase (phase 3) in one failing heart (#1), while it was due to a longer plateau (phase 2) in other failing hearts. Nevertheless, there was a close correlation between the functional remodeling (in repolarization and conduction) and the susceptibility to arrhythmia. Advancing the understanding of the arrhythmic mechanisms could facilitate the development of strategies to identify the HF patients who are more likely to benefit from anti-arrhythmic therapies, such as implantable cardioverter defibrillator (ICD).

5.6 Limitation

There are limitations in this study. First, the etiology of HF, its duration, and medical treatment are varied and uncontrolled, and we did not have access to clinical data due to de-identified tissue protocol. Therefore, only remodeling common to all the failing human hearts can be revealed in the study. Second, we did not study other pacing protocols, such as S1-S2-S3 protocol and short-long-short sequence of pacing, which have been shown to enhance the dispersion of repolarization (69, 93). Third, the isolated tissue preparations were mechanically unloaded due to the surgical opening of the tissue and the application of excitation-contraction uncoupler. It remains to be determined how the mechanical loading affects the electrical property in the human heart. Fourth, in isolated denervated preparations we did not use sympathetic stimulation and could not study the effects of heterogeneity of

innervation, which was shown to affect the dispersion of repolarization (168). Fifth, we did not quantify the local gradient of APD, which was a more sensitive marker for arrhythmia vulnerability than global dispersion of repolarization. We chose not to quantify it because there were many boundaries of fiber bundles and trabeculae carneae, the gradient across which was not an accurate representation of the true gradient in the same layers of myocardium. Finally, the failing human hearts in this study were all in the end stage of HF. These results might not apply to the failing human heart in earlier stages of HF.

6. Remodeling of Calcium Handling in Human Heart Failure

6.1 Abstract

Heart failure (HF) is an increasing public health problem accompanied by the rapidly aging global population. Despite considerable progress in managing the disease, the development of new therapies for effective treatment of HF remains a challenge. To identify targets for early diagnosis and therapeutic intervention, it is essential to understand the molecular and cellular basis of calcium handling and the signaling pathways governing the functional remodeling associated with HF in humans. Calcium cycling is essential mediator of cardiac contractile function. Thus, remodeling of calcium handling is thought to be one of the major factors contributing to the mechanical and electrical dysfunction in HF. Active research in this field aims to bridge the gap between basic research and effective clinical treatment of HF. This chapter reviews the most clinically relevant human studies regarding the remodeling of calcium handling. We also discuss their connections to the current and emerging clinical therapies for HF patients.

6.2 Introduction

Heart failure (HF) is a rising public health problem, with a prevalence of over 5.8 million in the USA, over 23 million worldwide, and continue to increase (33, 157). The contractile dysfunction and arrhythmogenesis associated with HF is closely related to the remodeling of calcium handling (18), which, in turn, is partially controlled by several signaling pathways in which Ca^{2+} has a prominent role (15). Deriving a mechanistic understanding of alterations in

calcium handling and calcium signaling is a critical step towards the development and improvement of physiology-based treatments for HF.

6.3 Overview of Cardiac Calcium Signaling

Ca^{2+} plays a central part in regulating excitation-contraction (EC) coupling and in modulating systolic and diastolic function in the heart as shown in Figure 30. Ca^{2+} signal transduction in the EC coupling comprises four steps (15, 107, 180). Firstly, the trigger Ca^{2+} current (I_{Ca}) is generated by the L-type Ca^{2+} channels expressed in the transverse tubules (T-tubules) following membrane depolarization. Secondly, the Ca^{2+} ions diffuse across the narrow junctional zone to activate ryanodine receptors (RyRs) and generate Ca^{2+} sparks, which is a considerable amplification of the original trigger Ca^{2+} signal. This process is known as Ca^{2+}-induced Ca^{2+} release (CICR). Thirdly, the Ca^{2+} influx from the sarcoplasmic reticulum (SR) then diffuses out to activate contraction following Ca^{2+} binding to troponin-C. Lastly, Ca^{2+} is transported back to SR by SR Ca^{2+}-ATPases (SERCA) and out of cell via Na^+/Ca^{2+} exchanger (NCX). Abnormal handling of intracellular Ca^{2+} at any of these steps can cause cardiac dysfunction in HF (122).

Intracellular Ca^{2+} homeostasis of cardiac myocytes is regulated by the phosphorylation of several key Ca^{2+}-handling proteins. One important regulatory kinase is cAMP-dependant protein kinase (PKA), which has been shown to regulate L-type Ca^{2+} channels, RyR and phospholamban (PLN). Despite the fact that global PKA activity is not changed in the failing human heart (24, 127), its local activity in the RyR macromolecular signaling complex might be locally increased (144, 169).
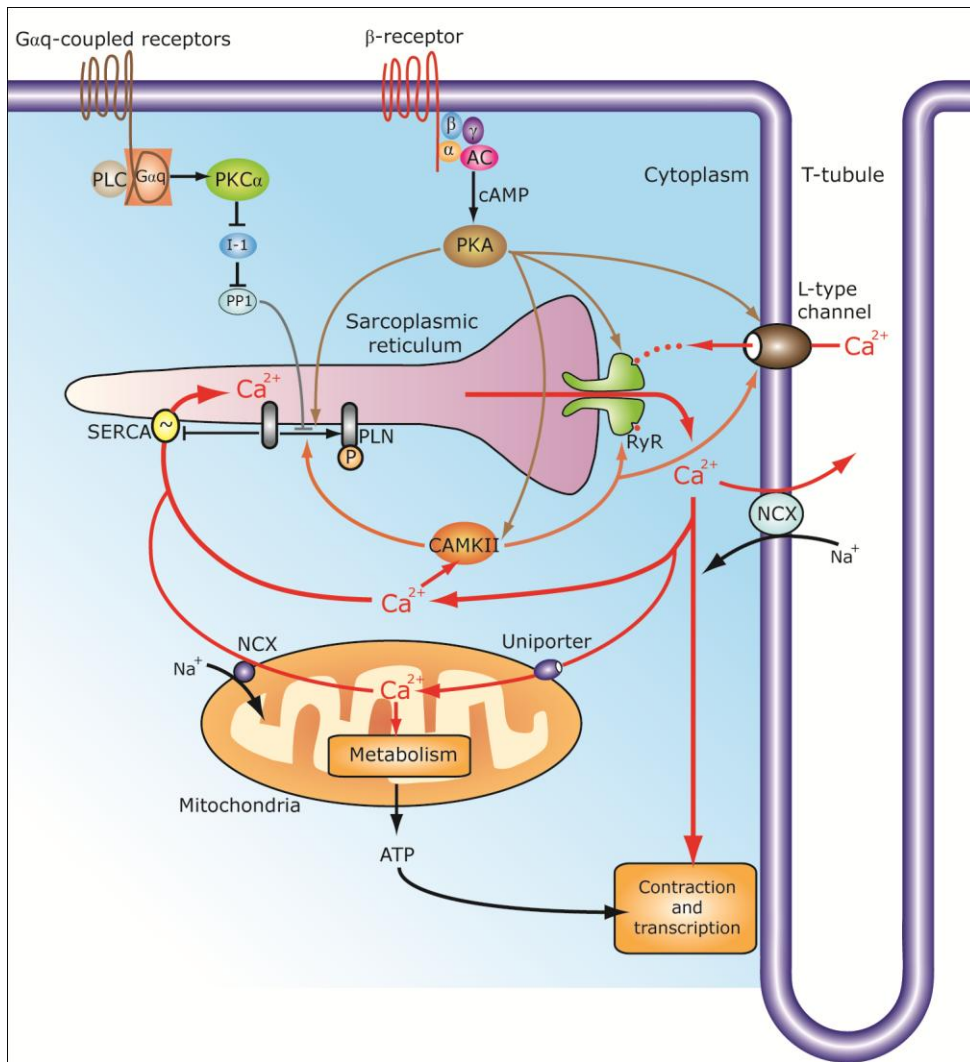
Figure 30. Intracellular Ca²⁺ cycling and regulation by signaling pathways. After the activation of sarcolemma (including T-tubules), Ca²⁺ enters cytoplasm through L-type Ca²⁺ channel. The entered Ca²⁺ then induces a much larger Ca²⁺ release from the sarcoplasmic reticulum (SR) via the ryanodine receptor (RyR). The released Ca²⁺ binds with Troponin C to activate contraction. The relaxation starts when Ca²⁺ is returned by sarcoplasmic reticulum Ca²⁺ ATPase (SERCA) back to SR and via Na⁺/Ca²⁺ exchanger (NCX) outside of the cell. Some Ca²⁺ enters mitochondria to stimulate the production of ATP which is utilized for contraction and transcription. SERCA is inhibited by the dephosphorylated phospholamban (PLN). PLN can be phosphorylated by protein kinase A (PKA) and Ca²⁺/calmodulin-dependent kinase (CAMKII), both of which can be activated by β-adrenergic stimulation. PLN can be dephosphorylated by protein phosphotase 1 (PP1), which can be activated through Gαq-coupled receptor (angiotensin II receptor, endothelin 1 receptor, or α-adrenergic receptor). A portion of Ca²⁺ enters into mitochondria to stimulate the production of ATP, which is used for contraction and transcription. α, G-protein subunit α; β, G-protein subunit β; γ, G-protein subunit γ; AC, adenylyl cyclase; cAMP, cyclic adenosine monophosphate.

Another important regulatory kinase is the Ca^{2+}/calmodulin-dependent protein kinase II (CaMKII).(166) CAMKII is a protein kinase that modulates several intracellular Ca^{2+}-handling proteins such as RyR, PLN, L-type Ca^{2+} channels as well as Na^+ channels (166). CAMKII is associated directly with the RyR and modulates the activity of RyR (48, 98, 260). Phosphorylation of PLN via CAMKII or PKA enhances the SR Ca^{2+} uptake via increased SERCA activity. Activity of CAMKII was shown to be significantly increased in the failing human heart and is correlated with the impaired ejection fraction (127, 239). Both PKA and CAMKII can be activated by β-adrenergic stimulation.

Finally, multiple isoforms of protein kinase C (PKC) might also play a role in regulating the Ca^{2+} handling. PKCα is the dominant isoform of PKC in the human heart (99) and is triggered by the activation of Gαq coupled receptors (angiotensin II receptor, endothelin-1 receptor, and the α-adrenergic receptor) (268). PKCα could phosphorylate protein phosphatase inhibitor 1 (I-1), consequently increasing the activity of protein phosphotase 1 (PP1), and then leading to enhanced phosphorylation of PLN and thus decreasing the activity of SERCA (32). The level of PKC is increased in human HF (27, 233, 252). The role of other isoforms of PKC in regulating calcium handling remains to be elucidated.

6.4 Alteration in intracellular Ca2+ and Mechanical Dysfunction in Failing Human Heart

The amount of Ca^{2+} delivered to the cytoplasm and the rate of Ca^{2+} removal from the cytoplasm are the two of the major factors determining the rate, intensity and duration of the contraction (269). Understanding of alterations in the intracellular Ca^{2+} concentration ($[Ca^{2+}]_i$) and their causal role in contractile dysfunction in the failing human heart has been greatly

advanced by the use of fluorescent $[Ca^{2+}]_i$ indicators (20, 21, 94, 96, 97, 160, 180, 204, 206, 245), which reflect changes in the free $[Ca^{2+}]_i$ necessary for the activation of contractile proteins (4, 23).

In isolated cells and tissues from failing human hearts, decreased amplitude of Ca^{2+} transient measured by the fluorescent intracellular Ca^{2+} indicators implies reduced Ca^{2+} release from SR (21, 133, 204). This is correlated with decreased peak stretch amplitude, a measure of myocardial contraction (105, 107). The reduced amplitude of Ca^{2+} transient is associated with decreased EC coupling gain (92) and decreased SR Ca^{2+} content (60, 112, 154, 204, 207, 208).

Moreover, the Ca^{2+} transient from failing human heart exhibits a reduced rate of Ca^{2+} removal (21, 94, 204). The slower rate of recovery of Ca^{2+} transient recovery is associated with a marked delay in tension relaxation in the failing human heart (94). Finally, failing human heart exhibits increased the resting intracellular Ca^{2+} level, leading to diastolic dysfunction (21, 97).

Altered $[Ca^{2+}]_i$ is frequency-dependent and most obvious at high heart rate (106). Normally, the amplitude of $[Ca^{2+}]_i$ transient is larger at higher stimulation frequencies (4). In human HF, however, the amplitude of Ca^{2+} transient was decreased at faster stimulation rates, leading to a reduced tension development at higher frequencies (97, 206). Increased resting $[Ca^{2+}]_i$ and a fusion of Ca^{2+} transient at fast frequencies may also occur, leading to an increase of end-diastolic tension and a decrease of active tension generation associated with incomplete relaxation and twitch fusion (97). The blunted or negative force frequency relationship (FFR) observed in both *in vivo* and *in vitro* studies in failing human hearts is in

contrast with the positive FFR in nonfailing human hearts (79, 97, 108, 184), and is associated with altered Ca^{2+} and Na^+ homeostasis as well as an inability to increase the SR Ca^{2+} content at increasing stimulation frequencies (207, 208).

The alteration of Ca^{2+} transient in failing human hearts is also region-dependent. We recently demonstrated the transmural heterogeneous remodeling of Ca^{2+} handing in the coronary-perfused left ventricular wedge preparations from failing and nonfailing human hearts (160). The sequence of Ca^{2+} transient relaxation is from epicardium to endocardium in both failing and nonfailing human heart at a slow heart rate (e.g., 0.67Hz/40 BPM) during endocardial pacing, because the difference of Ca^{2+} transient duration between subendocardium and subepicardium (or duration difference) is larger than the conduction time from subendocardium to subepicardium (Figure 31). Interestingly, this sequence is reversed at a fast heart rate (e.g., 1.67Hz/100 BPM) in the failing human heart due to a significant decrease of this duration difference (Figure 2C&D). In contrast, this sequence is not reversed in the nonfailing human heart because the duration difference is not significantly changed at faster frequencies (Figure 2B&D). We hypothesize that this reversed sequence of relaxation at fast heart rates could contribute to the end-systolic dysfunction (79) in the failing human heart. The maintenance of the normal relaxation sequence at slow heart rates in the failing hearts provides another mechanism for the beneficial effects of the heart-rate reduction in the patients with HF (241).

6.5 Molecular and Cellular Basis of Abnormal Calcium Handling and Signaling in Human HF

Alteration in the $[Ca^{2+}]_i$ is attributed to the abnormal calcium handling in the EC coupling process, which is operated by sarcolemma and SR, including L-type Ca^{2+} channels, RyR,

NCX, SERCA2a, etc. Changes of EC coupling in HF have been reviewed in detail elsewhere (18, 106, 268). Here we mainly focus on reviewing the results regarding the failing human heart.
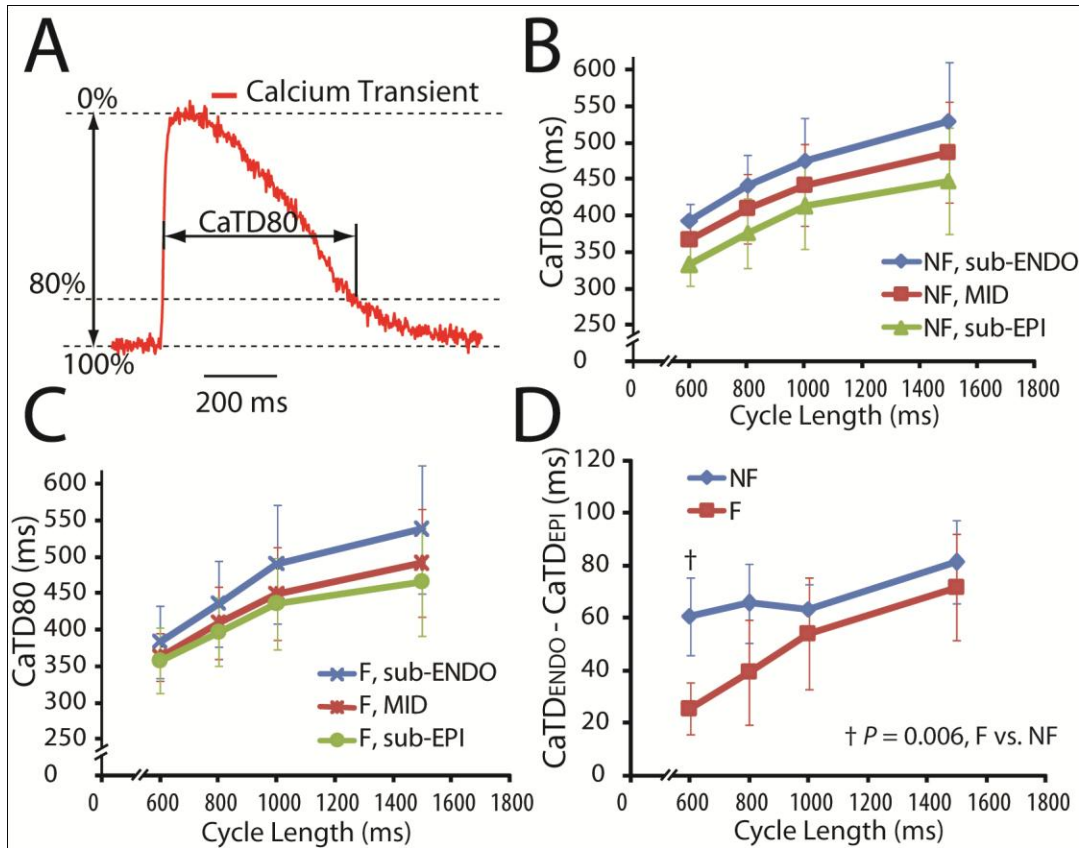
Figure 31. Region-dependent and cycle-length-dependent calcium transient duration (CaTD) in failing human heart. (A) CaTD was quantified at 80% relaxation (CaTD80). (B) CaTD80 at nonfailing human hearts (n=6) at subendocardium (sub-ENDO), midmyocardium (MID), and subepicardium (sub-EPI). (C) CaTD80 at failing human hearts (n=5). (D) The difference of CaTD80 between sub-ENDO and sub-EPI. It can be seen that this difference is significantly reduced in failing heart at faster heart rate (cycle length at 600ms).(160) These data are obtained from Ca²⁺ transient measured using Rhod-2AM from the coronary-perfused wedge preparations from both failing and nonfailing human hearts.

6.5.1 Calcium-Induced Calcium Release (CICR)

Triggering of CICR (i.e., I_{Ca}) in the failing human heart is mostly unchanged (20, 21, 172, 204), though inhibition of I_{Ca} was observed at higher frequencies (234). Thus, the smaller

Ca^{2+} transient observed in HF is mainly due to a reduced capability of I_{Ca} to trigger Ca^{2+} release from the SR (or a reduced EC coupling gain).

The reduced EC coupling gain may result from the hyperphosphorylation of RyRs in the failing human heart (169). PKA hyperphosphorylation of RyRs leads to the dissociation of the FKBP12.6 regulatory subunit, which inhibits the coupled gating of arrays of RyR channels and thus could result in a loss of EC coupling gain (169). This is supported by the reduced amplitude and changed properties of Ca^{2+} sparks measured from isolated ventricular myocytes from failing human hearts (153). More discussion of RyRs can be found in the section 6.5.2.

Rapid activation of RyRs by the I_{Ca} is facilitated by the close proximity of the L-type Ca^{2+} channels and RyRs. Reduced EC coupling gain in HF could thus also originate from the geometric disarrangement of RyRs and L-type Ca^{2+} channels, as suggested by the spontaneous hypertensive rat with HF (SHR-HF) (92). Disorganization of T-tubules and a decrease in the colocalization of L-type Ca^{2+} channels and RyRs have been demonstrated in the fixed ventricular samples from failing human hearts (47). The actual loss of T-tubules in isolated myocytes from failing human heart was reported in one study (164) but not in another (197), findings that might be explained by the large spatial variations in T-tubule remodeling in human HF (47).

The unltrastructural defects in the T-tubule system were demonstrated to cause the dyssynchronous Ca^{2+} release (or defective EC coupling) by confocal line scanning techniques in the isolated ventricular myocytes from SHR-HF, with Ca^{2+} release being delayed in certain regions of a myocyte compared to the other normally coupled areas (237). Louch et al.

showed modest dyssynchrony of Ca^{2+} release in the isolated myocytes from failing human hearts (163). While the local delayed SR Ca^{2+} release was confirmed in the whole heart level in SHR-HF (255), no study has been done so far to demonstrate the dyssynchronous Ca^{2+} release in tissue levels from the failing human heart. However, the morphological changes of Ca^{2+} transient observed in our recent left ventricular wedge preparations from failing human hearts imply the potentially important role of dyssynchronous Ca^{2+} (160). We observed two components in the rising portion of Ca^{2+} transient, with a slow rising component following an initial fast rising component (Figure 32A&B) (160). It is possible that the first fast-rising component corresponds to the normally triggered Ca^{2+} release and the second slow-rising component corresponds to the delayed Ca^{2+} release, which has been showed in SHR-HF (255). Interestingly, this morphological change of Ca^{2+} was only observed at the subendocardium in 60% of the studied failing human hearts (160). This regional difference might result from higher susceptibility to ischemia of endocardium compared with epicardium (81, 117), and suggests that the extrapolation of results from one region (e.g., epicardium) to another region (e.g., epicardium) in human studies should be done with caution. This delayed Ca^{2+} release might be also underlie the slower recovery of intracellular Ca^{2+} relative to the recovery of the action potential observed in our study (Figure 3A&C). That is, the Ca^{2+} transient outlasts the action potential at the subendocardium of the failing human heart, which might lead to phase-3 early afterdepolarization (34).

The reduced EC coupling gain could also result from decreased SR Ca^{2+} content, which has been extensively demonstrated in human HF (60, 154, 204, 207, 208). The success of molecular therapies aimed at restoring SR Ca^{2+} content further underscores the importance of SR Ca^{2+} content (118, 236). Reduced SR Ca^{2+} content in the failing human heart could

result from leaky RyRs, reduced SR Ca^{2+} uptake via SERCA2a, and increased Ca2+

extrusion via NCX, which are reviewed in the sections below (6.5.2-6.5.3).
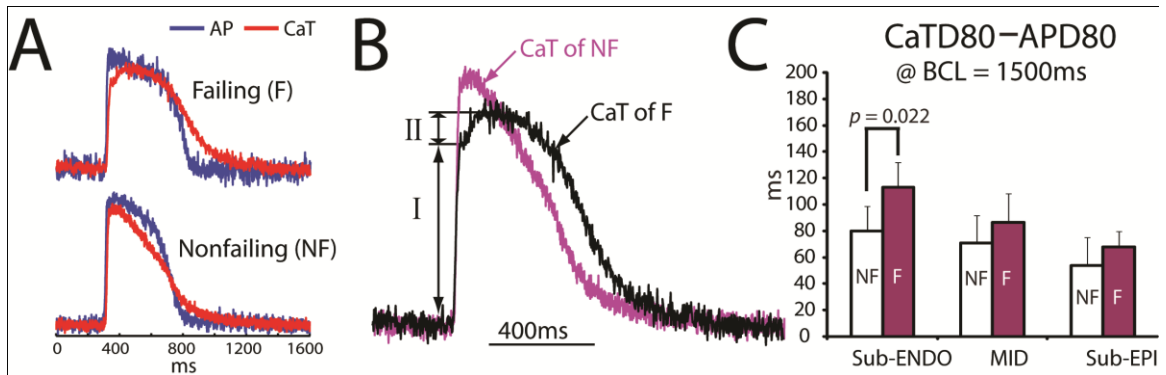
Figure 32. Morphological changes of calcium transient (CaT) and its relation to action potential (AP). (A) Simultaneous recordings of AP and CaT at one site at subendocardium from a failing human heart (F, top) and a nonfailing human heart (NF, bottom). (B) The two CaTs from panel A are overlapped for easy comparison. Compared to the CaT from NF, there is a distinct second rising component (labeled by "II") in the CaT from failing human heart. Note that this second component was only observed at the sub-endocardium in 60% of the studied failing human hearts. (C) CaT duration at 80% relaxation (CaTD80) minus AP duration at 80% (APD80). It can be seen that this duration difference is significantly longer at the subendocardium in the failing human heart compared with nonfailing human heart, which is reflected in the example shown in panel A.(160)

6.5.2 RyR

Most studies showed no change in the protein expression of RyR in human HF (18, 106).

However, the characteristics of Ca^{2+} sparks are altered in isolated myocytes from failing

human hearts (153). Furthermore, RyRs in human HF are "leaky" (169), contributing to the

reduction of SR Ca^{2+} content (132). The SR Ca^{2+} leak occurs in despite of the reduced SR

Ca^{2+} loading in a canine model of HF (132).

   Leaky RyR is thought to result from hyperphosphorylation of RyR by PKA or CAMKII.

Increased Ca^{2+} sensitivity and open probability of RyR in failing human heart was first

observed by Marx et al. (169) They concluded that the increased local PKA-phosphorylation

of RyR in HF lead to the disassociation of FKBP12.6 from RyRs, leading to higher open

probability at rest (169). They also observed decreased association of phosphatases (PP1,

protein phosphotase 2A [PP2A]) to RyR, which may exacerbate PKA-hyperphosporylation

of RyR (169). The PKA-hyperphosphoryation of RyRs could also result from the deficiency

of phosphodiesterase 4D (PDE4D), which resides in the RyR macromolecular signaling

complex and regulates the local concentration of cAMP that activate PKA (144). The

capability of PKA phosphorylation in reducing the RyR/FKBP12.6 association remains

controversial because it was not confirmed by some groups (119, 150).

Increased SR Ca^{2+} leak in isolated myocytes from failing rabbit heart was shown to relate

to the hyperphosphoryation of RyR by CAMKII (1). The Ca^{2+} leak was reduced by the

inhibition of CAMKII but not altered by PKA inhibition (1), suggesting the potential role of

CAMKII inhibition in improving the Ca^{2+} handling in HF. This hypothesis is further

supported by a recent study by Sossalla et al. (239), who showed a significant increase in the

expression the CAMKII in both left and right ventricles of the failing human heart , and that

the inhibition of CAMKII reduced the SR Ca^{2+} leak and increased the Ca^{2+} content.

Importantly, they also showed that inhibition of CAMKII improved contractility in isolated

ventricular trabeculae.(239) They reported that CAMKII inhibition restored the positive

FFR.(239) This is in sharp contrast to the study by Kushiner et al. (136), which showed that

CAMKII inhibition completely abolished the positive FFR in mouse heart. The result from

Kushiner et al.'s study is consistent with the hypothesis that CAMKII is responsible for

sensing the frequency of Ca2+ oscillation (54) as well as for causing the positive FFR via the

increase of phosphorylation of RyR and PLN at increasing frequencies (260, 271). Kushiner

et al. also showed that RyR phosphorylation by CAMKII was decreased in failing human heart in despite of the global increase of CAMKII (136), and suggested that the impaired RyR phosphorylation by CAMKII plays a role in blunted FFR in human HF. Further studies are needed to resolve the areas of controversy and clarify the molecular mechanism and the promise of CAMKII inhibition in improving the Ca^{2+} handling in human HF.

While much evidence supports altered regulation and function of the RyR leading to abnormal Ca^{2+} handling in failing human heart, there are studies indicating the opposite. Recordings of currents through the RyR from failing human hearts did not reveal any significant alterations at a single channel level (113). Jiang et al. observed neither structural nor functional change of RyRs from the failing human heart but did report a significant reduction in SERCA2a expression, suggesting that abnormal Ca^{2+} uptake may contribute more to the altered Ca^{2+} handling in human HF (119).

6.5.3 SERCA2a, PLN and NCX

SR Ca^{2+} uptake was reduced in the failing human heart (57, 108, 204, 230). This might be due to depressed protein expression of SERCA2a. Hasenfuss et al. observed downregulation of SERCA2a expression as well as a significant correlation between SERCA protein levels and SR Ca^{2+} uptake in failing human hearts (108). Overexpression of SERCA2a has shown to restore the Ca^{2+} handling and the contractile function with positive FFR in isolated failing human myocytes (56, 57). While some studies observed the downregulation of protein expression of SERCA2a in the failing human heart, others did not find any change in the protein expression of SERCA2a (85). This inconsistency might be explained by our recent findings (160). We observed down-regulation of SERCA2a expression in samples from the subendocardium of failing human hearts with ischemic cardiomyopathy but not in samples

from epicardium or from failing hearts with dilated cardiomyopathy, suggesting that the alteration of SERCA2a expression might be region-dependent as well as the HF etiology-dependent (160).

Besides the potential decrease in protein expression, the decreased activity of SERCA2a in HF might also result from altered regulation. This is supported by the findings that decreased SR Ca^{2+} uptake was observed in despite of unchanged protein levels of SERCA2a (57, 230, 231).

SERCA2a is directly regulated by PLN which is mainly phosphorylated by PKA and CAMKII (85). PLN inhibits SERCA2a activity when it is not phosphorylated, while its phosphorylated form disassociate from SERCA2a. In the failing human heart, majority of the studies indicate no change in the protein expression of PLN (85, 160), which is consistent with our recent study (160), However, phosphorylation state of PLN was decreased in the failing human heart (49, 57, 231), suggesting increased inhibition of SERCA2a by PLN in the failing human heart. PLN is mainly phosphorylated by PKA at serin-16 and by CAMKII at threonine-17. Phosphorylation at threonine-17 is decreased due to increased dephosphorylation by calcineurin in the failing human heart with dilated cardiomyopathy (186). PLN phosphorylation at serin-16 is decreased presumably due to increased level of PP1 in the failing human heart (177, 231), which might be due to an increased level of PKCα (27, 32). Interventions to attenuate the inhibitory effect of PLN on SERCA2a have been tested in animal models. Minamisawa et al. found that knockout of PLN significantly increased SR Ca^{2+} content and completely rescued the spectrum of heart-failure phenotype in a mouse model of HF (174). Decreased PLN expression via adenoviral gene transfer of antisense of PLN was shown to improve both contraction and relaxation in

isolated myocytes from failing human hearts (56). Inhibition of PKCα was shown to increase the SR Ca^{2+} load and protect the mouse from HF (32, 156). The importance of PKCα and other isoforms of PKC in the Ca^{2+} handling in human HF remains to be determined.

While protein expression of NCX was found upregulated in most animal models of HF (18), it is less consistent in the failing human heart with either increased or unchanged protein expression of NCX (106). In contrast to reduced SR Ca^{2+} uptake, the NCX current density as a function of $[Ca^{2+}]$ was not changed in the failing human heart (204). However, the contribution of NCX to the $[Ca^{2+}]_i$ relaxation was increased due to the depressed SR Ca^{2+} uptake (204). Furthermore, the preference of NCX current direction during the action potential plateau shifted from inward direction (Ca^{2+} efflux) to outward direction (Ca^{2+} influx) due to a reduced submembrane $[Ca^{2+}]_i$ and increased $[Na^+]_i$ in the failing human heart (259). The reversed-mode NCX during AP plateau could contribute to a slow decay of $[Ca^{2+}]_i$ transient (60, 259), which may facilitate contraction at slow heart rates but may also lead to diastolic dysfunction at faster heart rates (208).

6.5.4 Loss of metabolic capacity

Ca^{2+} handling and energy homeostasis are interdependent (249). Ca^{2+} homeostasis relies on efficient energy-driven ionic fluxes, i.e., through SERCA2a and Na^+-K^+ ATPase, while $[Ca^{2+}]_i$ in turn determines energy consumption through contraction and Ca^{2+} transport as well as energy production via the regulation of ATP generation in mitochondria (16, 249). Disturbance of the finely tuned balance between the two could be responsible for abnormal Ca^{2+} handling and diminished contractility that are hallmarks of HF.

HF is associated with defects in energy metabolism, with decreased energy production as well as impaired energy transfer and utilization (249). These impaired cardiac energetics may represent the thermodynamic limit for Ca^{2+} handling (55). Reduced local ATP/ADP ratio, due to a local lack of creatinine kinase, could affect the kinetic and thermodynamic efficiency of SERCA in HF (55), providing another mechanism for impaired SR Ca^{2+} uptake. Indeed, ATP was reported to protect SERCA2a from being denatured by hydroxyl radicals (267), implying that energy starvation might render SERCA2a unprotected from increased oxidative stress in human HF.

Improving the myocardial energetics has been shown to normalize the Ca^{2+} cycling in isolated failing human myocytes (103). β-blockers, which decrease the energy demand and thus ameliorate the mismatch between energy production and consumption, has been shown to normalize the function and regulation of key Ca^{2+} handling proteins in failing human hearts (220). Similarly, left ventricular assist devices (LVADs), which unload the heart and support the circulation, impart improved Ca^{2+} handling in human HF (37, 169). Finally, hemodynamic improvement by cardiac resynchronization therapy (CRT) is correlated with improved Ca^{2+} handling in the subset of HF patients who respond to this therapy (247). On the other hand, restoration of Ca^{2+} homeostasis may result in improved cardiac energetics (58).

6.6 Conclusion

It has been well recognized that abnormal Ca^{2+} handling is the key pathophysiological mechanism in human HF. On the other hand, the understanding of the underlying molecular

and cellular mechanisms for the altered calcium handling in the failing human heart remains incomplete.

The is partly due to the complexity of system, which involves the interplay between a number of signaling pathways that regulates the Ca^{2+} homeostasis at different time scales (114, 236). That is, while interrupting or augmenting one of pathways in the cascade might lead to expected beneficial therapeutic effects; it might also produce unexpected deleterious effects (236). Nevertheless, the structure of this complex system are continuingly being revealed by ongoing basic and clinical researches, which carry the hope of facilitating the development of effective diagnosis and treatment of HF. The progress is also slowed by limited data from human studies. While many mechanistic hypothesis and potential therapeutic intervention for the abnormal Ca^{2+} handling in HF are being proposed and tested in the animal models of HF, the examination of these hypothesis and therapies using functional studies of isolated cells or tissues from the failing human heart are rather limited. We believe that the basic understanding and clinical translation can be greatly facilitated by testing the hypothesis in the explanted human heart donated for research by patients and donors (67).

Gaining a clearer understanding of the causative mechanisms of abnormal Ca^{2+} handling is crucial to developing promising new therapies to treat HF. Despite our best efforts, there are currently only two major medical pharmacological approaches available to the clinician for the treatment of patients with HF: blockade of the β-adrenoreceptor and inhibition of the RAA axis. These first line agents are used to treat non-ischemic (the majority of which are idiopathic), ischemic and valvular cardiomyopathies, even though we recognize fundamental differences in the insults that cause these separate conditions. Such blanket

approaches demonstrate the limits of our current knowledge, and the need for further observation and testing before new therapies can be delivered to the patient. Moreover, it is clear that many pathways involving Ca^{2+} handling converge on and act through a few key molecules. Thus, the complex biological processes leading to HF must be further dissected with respect to specific isoforms, subcellular locations and etiology of HF. Similarly, it is important to realize that individual drugs effects must be categorized based on the species and type of animal model used. Finally, we must recognize that the road to developing a human therapeutic agent, i.e., going from the bench to the bedside, is a time consuming and expensive one, and littered with failures. These complexities may explain why after years of research, the clinical armamentarium for reversing HF remains rather limited. Despite these drawbacks, it is encouraging that many promising new therapies to ameliorate abnormal calcium handling are visible on the horizon, based on findings in animal models of HF. Increased research on functional human heart tissue would facilitate translation of these findings to clinic.

7. Transmural Heterogeneity and Remodeling of Ventricular Excitation-Contraction Coupling in Human Heart Failure

7.1 Abstract

Excitation-contraction (EC) coupling is altered in the end-stage heart failure (HF). However, spatial heterogeneity of this remodeling has not been established at the tissue level in failing human heart. The objective is to study functional remodeling of EC coupling and calcium handling in failing and nonfailing human hearts.

We simultaneously optically mapped action potentials (AP) and calcium transients (CaT) in coronary-perfused left ventricular wedge preparations from nonfailing (n = 6) and failing (n = 5) human hearts. Our major findings are: (1) CaT duration minus AP duration was longer at sub-endocardium in failing compared to nonfailing hearts during bradycardia (40 beats/min). (2) The transmural gradient of CaT duration was significantly smaller in failing hearts compared with nonfailing hearts at fast pacing rates (100 beats/min). (3) CaT in failing hearts had a flattened plateau at the midmyocardium; and exhibited a "two-component" slow rise at sub-endocardium in three failing hearts. (4) CaT relaxation was slower at sub-endocardium than that at sub-epicardium in both groups. Protein expression of sarcoplasmic reticulum Ca^{2+}-ATPase 2a (SERCA2a) was lower at sub-endocardium than that at sub-epicardium in both nonfailing and failing hearts. SERCA2a protein expression at sub-endocardium was lower in hearts with ischemic cardiomyopathy compared with nonischemic cardiomyopathy.

In conclusion, for the first time, we present direct experimental evidence of transmural heterogeneity of EC coupling and calcium handling in human hearts. End-stage HF is associated with the heterogeneous remodeling of EC coupling and calcium handling.

7.2 Introduction

Congestive heart failure (HF) is one of the leading causes of death in Western countries (7). Depressed contractility during congestive HF is associated with altered excitation-contraction (EC) coupling, in general, and calcium handling, in particular (14, 17, 203, 235).

Most experimental studies of EC coupling in human hearts were conducted in isolated cells or muscle strips (21, 95, 104, 107, 181, 182, 205, 246), where anatomical differences could not be investigated. However, the anatomical location of the region from which cells are harvested could be very important (235). Animal studies suggest that transmural heterogeneities of EC coupling and intracellular calcium exist. For example, Cordeiro et al. observed that the latency to onset of contraction was shorter, and SR Ca^{2+} content is larger in epicardial cells as compared to endocardial cells in normal canine left ventricle (45). Investigating calcium handling, Laurita et al. showed that the recovery of intracellular calcium in canine left ventricle was slower in cells near the endocardium (ENDO) compared with cells near the epicardium (EPI) (140). We have recently described spatial heterogeneity of action potential (AP) in human ventricle and its implication for the vulnerability to arrhythmias (90). However, spatial heterogeneity of EC coupling and intracellular calcium handling in human heart remains unclear.

It was suggested by a molecular study by Prestle et al. that the transmural heterogeneity of calcium handling was enhanced in the failing human hearts compared with nonfailing human

hearts (211). In failing human hearts, the protein expression of the sarcoplasmic reticulum Ca^{2+}-ATPase 2a (SERCA2a) was reduced significantly in the sub-ENDO compared to the sub-EPI,(211) which might lead to the heterogeneous uptake of intracellular calcium and facilitate the induction of ventricular arrhythmias (140, 141, 264). In spite of the molecular evidence, it remains unknown if the heterogeneity of EC coupling and calcium handling is present and how it is functionally remodeled in heart failure. Furthermore, it is unknown if this remodeling could contribute to the increased ventricular arrhythmogenesis and mechanical dysfunction associated with human HF. We hypothesize that across the intact transmural wall there exists intrinsic heterogeneities of EC coupling and calcium handling and thus the susceptibility to remodeling during HF differs in different transmural layers of the left ventricle. To test this hypothesis, dual optical mappings of AP and calcium transient (CaT) were conducted in left ventricular (LV) wedge preparations from both failing and nonfailing human hearts.

7.3 Methods

7.3.1 Experimental Protocol

The study was approved by the Washington University Institutional Review Board. Both failing (n = 5) and nonfailing (n = 6) human hearts were optically mapped in this study. For Western blot assay, we used tissue from 19 hearts. Patient information is shown in Table 2.

The isolated LV wedge preparation has been described in our previous paper (90). Briefly, a piece of LV wedge from the scar-free post-lateral LV free wall perfused by the left marginal artery (Figure 33A) was isolated and cannulated. Tissue was immobilized by blebbistatin (10~20 µM, Tocris Bioscience, Ellisville, MO) to suppress motion artifacts in

Table 2.

Patient Information

#	Group	Gender	Age	Diagnosis	Experiment
1	Nonfailing	Male	55	Death from stroke	Mapping, WB
2	Nonfailing	Female	59	Anoxic brain injury post cardiac arrest	Mapping, WB
3	Nonfailing	Male	53	Intracranial hematoma	Mapping, WB
4	Nonfailing	Male	56	Intracranial hematoma	Mapping, WB
5	Nonfailing	Female	47	Brain death due to anoxia	Mapping, WB
6	Failing	Female	65	Ischemic cardiomyopathy	Mapping, WB
7	Failing	Male	63	Ischemic cardiomyopathy	Mapping, WB
8	Failing	Male	49	Idiopathic cardiomyopathy	Mapping, WB
9	Failing	Female	54	Idiopathic cardiomyopathy	Mapping, WB
10	Failing	Female	54	Idiopathic cardiomyopathy	Mapping, WB
11	Nonfailing	Female	50	Brain death from anoxia	Mapping
12	Nonfailing	Female	66	Brain Death from hemorrhaging	WB
13	Failing	Male	61	Ischemic cardiomyopathy	WB
14	Failing	Male	64	Ischemic cardiomyopathy	WB
15	Failing	Female	49	Ischemic cardiomyopathy	WB
16	Failing	Male	50	Ischemic cardiomyopathy	WB
17	Failing	Male	47	Idiopathic dilated cardiomyopathy	WB
18	Failing	Female	44	Idiopathic cardiomyopathy	WB
19	Failing	Male	70	Idiopathic dilated cardiomyopathy	WB

Mapping indicates optical mapping experiments

WB, Western blotting assay

101

optical recordings (77). The tissue was co-stained with RH237 and Rhod-2 AM for simultaneous mapping of AP and CaT. Representative recordings of voltage and calcium collected at different layers of the LV wedge are shown in Figure 33C. The definition of quantified parameters are shown in Figure 33D. Signals from an array of pixels spanning the whole field of view are presented in the Figure 34 to demonstrate the uniform quality of recordings. Details of the dual imaging system are described in Appendix B.
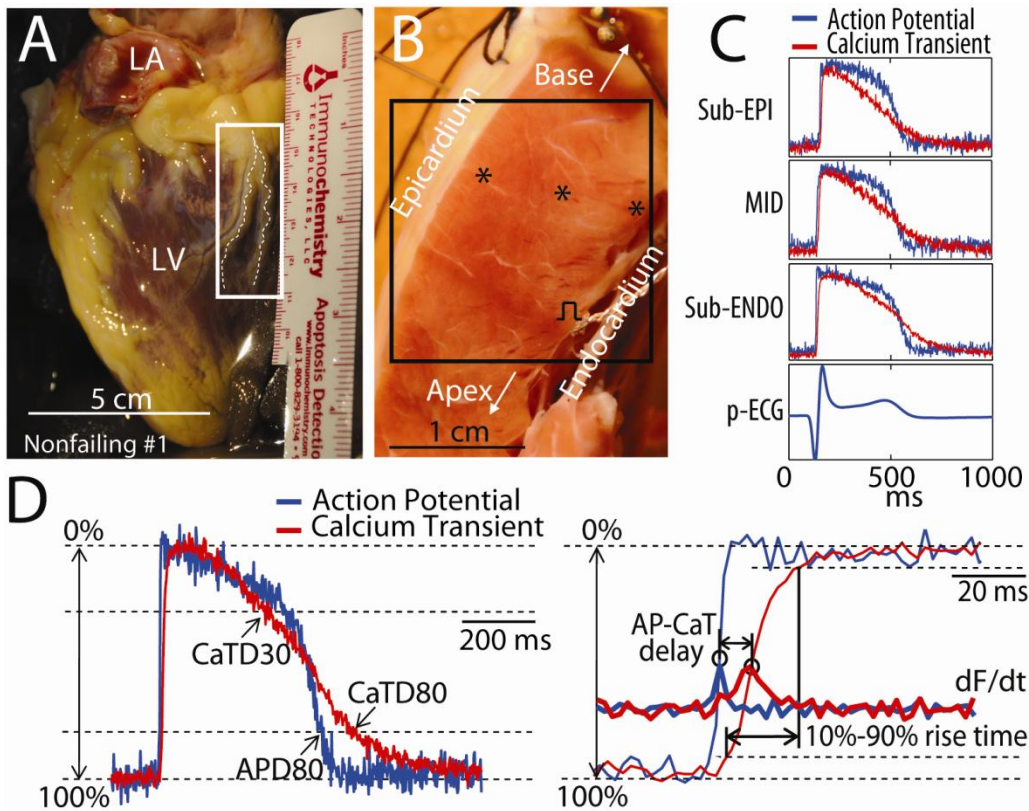
Figure 33. Left ventricular wedge preparation and optical recordings of action potentials (AP) and calcium transients (CaT). (A) An explanted nonfailing human heart. The region indicated by white rectangle was dissected and cannulated for wedge preparation. (B) The left ventricular wedge preparation from the same heart. (C) Pseudo-ECG (p-ECG) and representative optical recordings of AP and CaT from locations within sub-endocardium (sub-ENDO), midmyocardium (MID), and sub-epicardium (sub-EPI), which are indicated by the black stars shown in the panel B. (D) Terminology. Left: superimposed AP and CaT with illustrations of AP duration at 80% repolarization (APD80), CaT duration at 30% and 80% recovery (CaTD30 and CaTD80). Right: Close-up view of upstrokes (thin lines), and the derivatives (thick lines, labeled as dF/dt) with illustrations of AP-CaT delay and 10%-90% rise time of CaT.
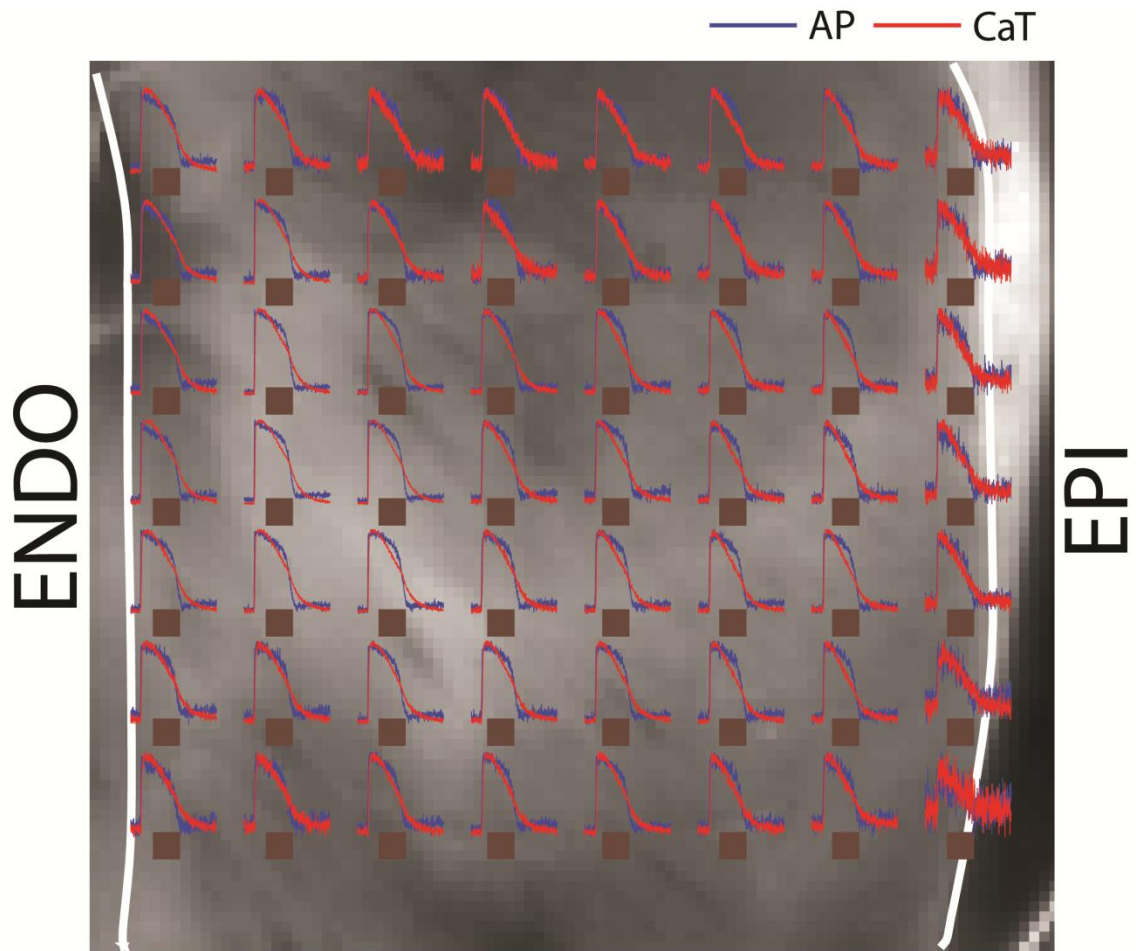
Figure 34. Representative simultaneous optical recordings of action potential (AP, blue) and calcium transient (CaT, red). Signals are taken from the evenly spaced local regions (labeled by the brown squares) which span the entire mapping field of view of a left ventricular wedge preparation. The endocardium (ENDO) and epicardium (EPI) are labeled by the white lines.

The LV wedge preparations were paced at the ENDO at twice the diastolic pacing threshold. Dynamic restitution protocol was conducted in which pacing was started at a basic cycle length (BCL) of 1500 ms and it was gradually decreased until the ventricular functional refractory period was reached. Two Ag/AgCl electrodes were placed near the ENDO and EPI surfaces respectively to measure the pseudo-ECG. For more details of the Methods (tissue preparation, optical mapping system, and Western blot).

7.3.2 Western Blot

Immediately after the delivery of the heart to our research lab, tissue samples at sub-endocardium (sub-ENDO, 2 mm to the endocardium) and sub-epicardium (sub-EPI, 2 mm to the epicardium) were dissected from LV, frozen in liquid nitrogen, and stored at -80°C until use. Standard Western blot procedures were used. We used the anti-SERCA2a monoclonal antibody and an anti-phospholamban monoclonal antibody (Affinity BioReagent, Golden, CO) as well as anti-GAPDH monoclonal antibody (Sigma, St. Louis, MO). Chemiluminescence was measured by luminescent image analyzer LAS-4000 (Fujifilm, Tokyo, Japan). Protein bands were quantified by software Multi-Gauge 3.0 (Fujifilm, Tokyo, Japan). Protein expression was analyzed in three groups of hearts (Table 2): nonfailing hearts (n=6), and failing hearts due to different etiologies: nonischemic/idiopathic cardiomyopathy (n=6) and ischemic cardiomyopathy (n=6).

7.3.3 Data Analysis

All signals were low-pass filtered at 60Hz. The voltage-calcium delay was defined as the delay between the upstrokes of AP and CaT (Figure 33D). Each upstroke was defined at $(dF/dt)_{max}$, where F is the voltage or calcium fluorescent signal (42). AP duration (APD) was measured as the time from the upstroke to 80% repolarization (i.e., APD80, Figure 33D). Similarly, the CaT duration (CaTD) was measured as the time from the upstroke to 30% and 80% recovery (i.e., CaTD30 and CaTD80, Figure 33D). The 10-90% rise time of CaT was measured as the time from 10% CaT (close to the baseline) to 90% CaT (close to the peak, Figure 33D). Relaxation of CaT was quantified by the time constant (τ) of a single exponential fit of the CaT tail, i.e., the time from the minimum of $d(CaT)/dt$ to the resting level of CaT. Sub-EPI was defined as the region within 2mm from the epicardial surface (See

Figure 2B on the right); midmyocardium (MID) was the 2mm-wide midmyocardial layer; and sub-ENDO was the region within 2mm from the endocardial surface.

7.3.4 Statistical Analysis

For statistical analysis, we used ANOVA. Specifically, we fit a linear mixed effects repeated measures model, where the patient was a random effect and other factors (failing/nonfailing, tissue layers, and basic cycle lengths [BCL]) were fixed effects. Models contained parameters that allow heterogeneous variance among levels of the failing/nonfailing by tissue-layer interaction and repeated measures correlation among tissue layers. We compared models by the small-sample-size−corrected version of Akaike information criterion. Contrasts were used to test the significance of differences between the failing and nonfailing groups within different tissue layers (sub-ENDO/MID/sub-EPI). Bonferroni adjustment was used to account for multiple comparisons. Detailed specifications of statistical analysis for individual figure are provided in the Online Data Supplement. *P* value less than 0.05 was considered statistically significant. Values were given as means ± S.D.

7.4 Results

7.4.1 Voltage-Calcium Delay (AP-CaT Delay)

To quantify the EC coupling, the delay between the AP upstroke and CaT rise was measured. As expected, the upstroke of the AP was always followed by the rise of CaT (Figure 33D). To quantify the transmural heterogeneity, this delay was measured and averaged at all three tissue layers (sub-ENDO, MID, and sub-EPI). Figure 35A&B is a representative example displaying AP and CaT activation maps as well as the voltage-calcium delay. This delay is summarized in Figure 35C for the BCL of 1500 ms. We observed a transmural gradient of

this delay within the failing group. That is, the delay was significantly larger at sub-ENDO than sub-EPI (*P* = 0.015, see Figure 35B as an example).
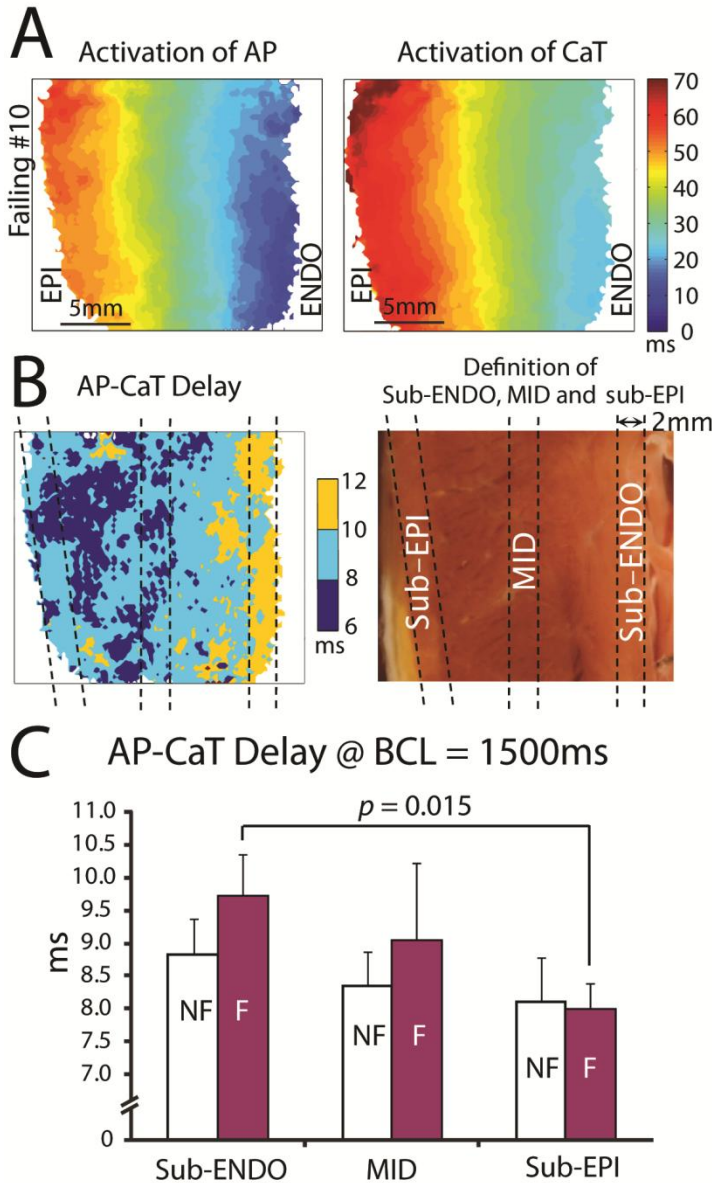
Figure 35. Voltage-calcium (AP-CaT) delay. (A) Activation maps for AP and CaT from a failing human heart (#10). (B) Map for AP-CaT delay and the anatomic definition of sub-ENDO, MID and sub-EPI from the same heart. (C) Summarized results for AP-CaT delay at the sub-ENDO, MID, and sub-EPI at a basic cycle length (BCL) of 1500ms in failing (F, n=5) and nonfailing (NF, n=6) hearts.

7.4.2 APD and CaTD

We quantified APD, CaTD, and the difference between the two (i.e., CaTD - APD). Figure 3 shows one example from a nonfailing heart (Figure 36A) and one from a failing (Figure 36B) heart. Maps of APD80 and CaTD80 are shown for both hearts. It should be noted that

the color scales for APD and CaTD maps are different. It can be seen that APD80 mildly

increased in this failing heart compared with that in the nonfailing heart, while CaTD80 was

increased in a more substantial manner. Because of the disproportionate prolongation of
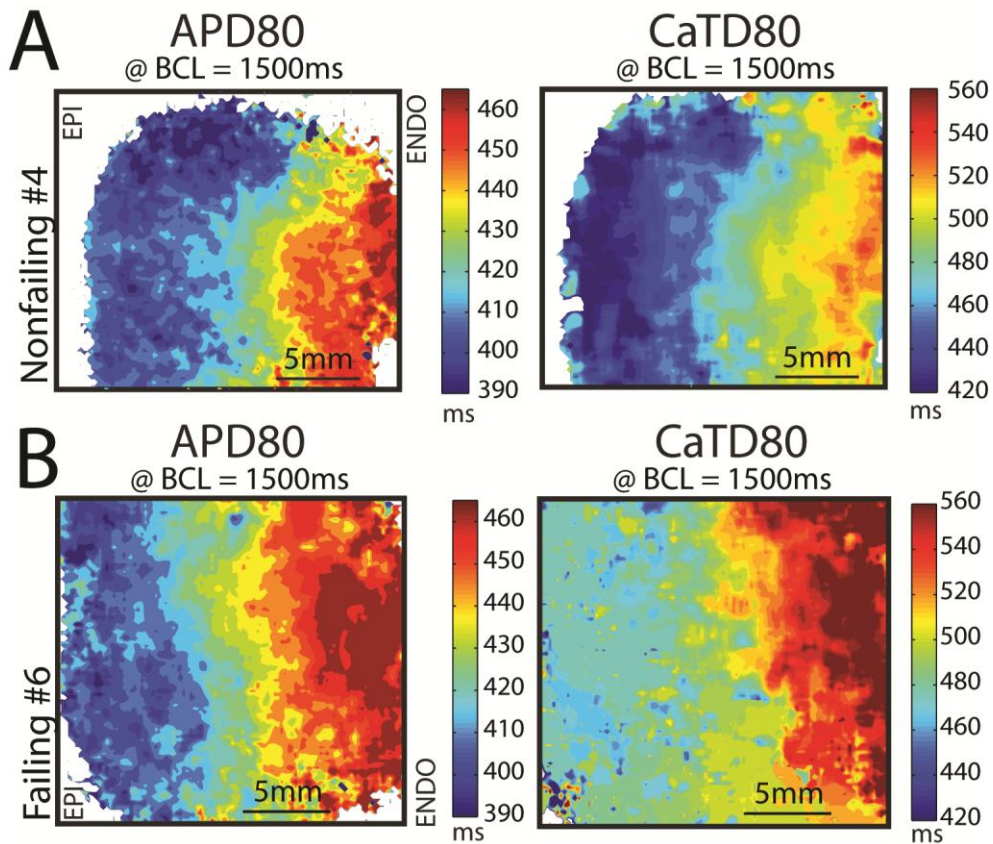
Figure 36. Representative maps of APD80 and CaTD80 at the basic cycle length (BCL) of 1500ms. (A) APD and CaTD maps from a nonfailing human heart. (B) APD and CaTD maps from a failing human heart. ENDO indicates endocardium, EPI, epicardium.
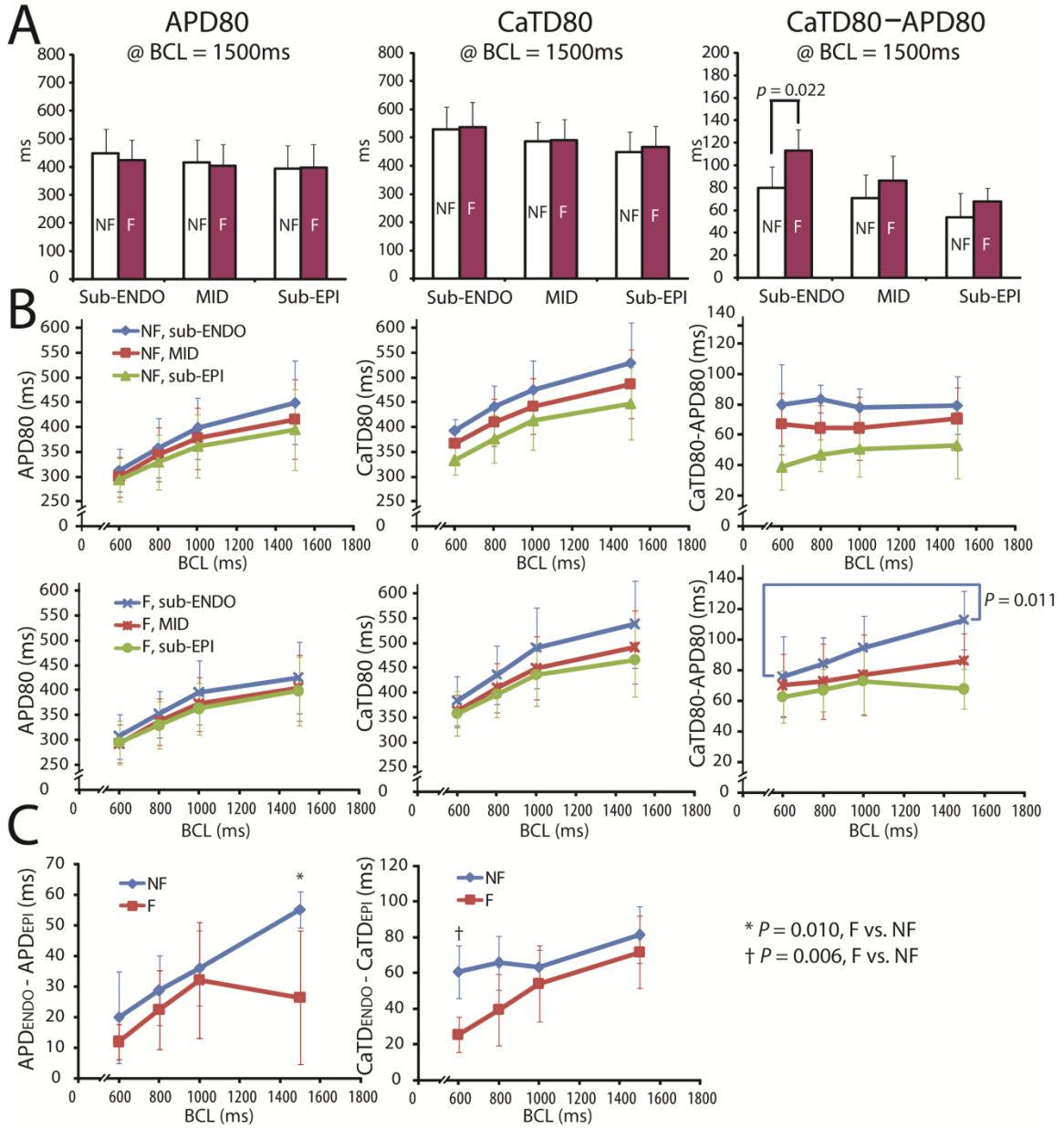
Figure 37. APD, CaTD and the duration difference (APD-CaTD). (A) APD80, CaTD80 and the duration difference at the basic cycle length (BCL) of 1500ms in failing (F, n=5) and nonfailing (NF, n=6) hearts at sub-ENDO, MID, and sub-EPI. (B) Dynamics of APD80, CaTD80 and the duration difference at various cycle lengths at sub-ENDO, MID and sub-EPI. The top row in panel B is for nonfailing hearts, and the bottom row in panel B is for failing hearts. (C) Transmural APD and CaTD gradients. The gradient is calculated as the difference between the values of sub-ENDO and sub-EPI.

CaTD relative to APD, (CaTD80 - APD80) in the failing heart was larger than that in the nonfailing heart.

APD80, CaTD80, and (CaTD80-APD80) for both failing and nonfailing groups are shown in Figure 37A for the BCL of 1500 ms and are summarized in Figure 37B for multiple BCLs. The transmural APD and CaTD gradient represented by the sub-ENDO and sub-EPI duration differences are shown in Figure 37C. Transmural APD gradients are present in both failing and nonfailing human hearts. Similar to our previous study (90), at slow heart rates, this gradient was less pronounced in the failing group compared with the nonfailing group (Figure 37A&C-left). CaTD80 (Figure 37A-middle) also exhibited gradients from the endocardium to the epicardium. Interestingly, this gradient (Figure 37C) was significantly smaller in the failing group compared with the nonfailing group at fast heart rates (e.g., 100 beats/min [bpm] or BCL=600 ms) but not at slow heart rates (e.g., 40 bpm or BCL=1500 ms).

The duration difference (CaTD80 - APD80) was significantly increased at sub-ENDO in the failing hearts during bradycardia ($P = 0.022$, Figure 37A-right). As the BCL decreased, the duration difference was significantly decreased within the failing group, while it remained unchanged in the nonfailing group (Figure 37B-right). Both APD80 and CaTD80 were decreased as the BCL was decreased (Figure 37B-left and middle).

M cell islands, which contain prolonged APDs and are surrounded by large APD gradients, were observed previously in nonfailing human hearts (90). In the majority of the hearts in this study, APD decreased gradually from ENDO to EPI without the presence of M cells. However, M cells were observed in one nonfailing heart, where we specifically

searched for them (Figure 38). As shown in the map of APD80 (Figure 38B), the M-cell area

was in the form of an isolated island rather than a continuous layer. This region exhibited a

delayed repolarization (Figure 38E) and was surrounded by steep local APD gradients

(Figure 38C). As shown in Figure 38D and 38E, the M-cell island had longer CaTD

compared with neighboring regions. Other M-cell island parameters (AP-CaT delay, CaTD-

APD, CaT rise time, CaTD30/CaTD80, and τ) were not different from neighboring mid-

myocardium regions (Figure 39).
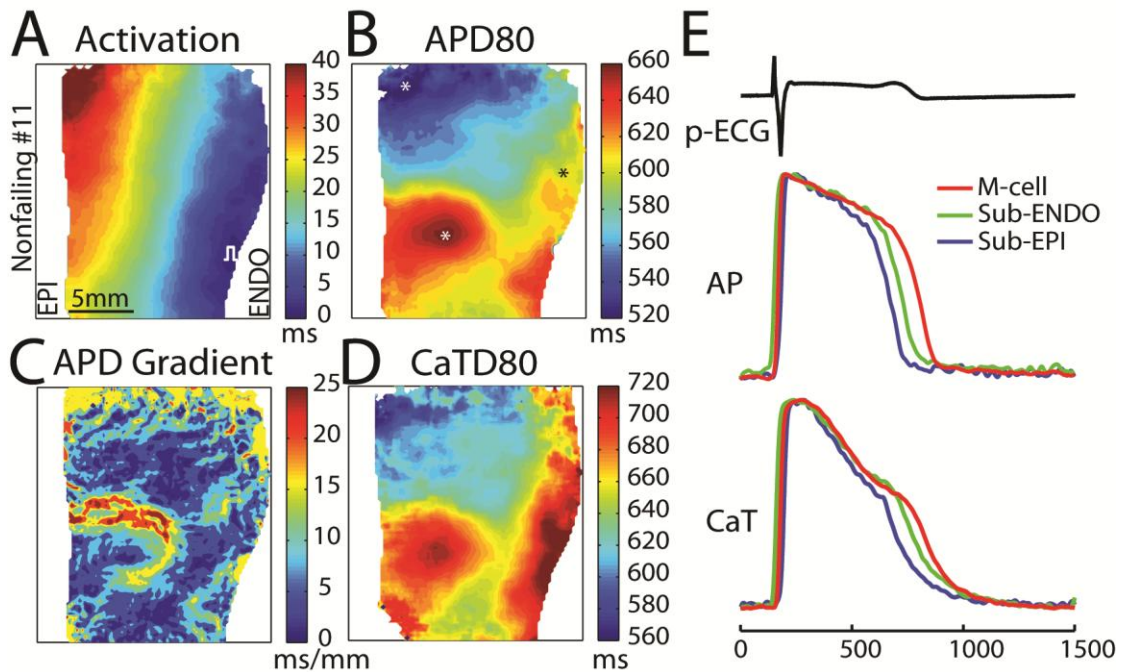
Figure 38. M cell island. (A) Activation propagation from ENDO to EPI. (B) APD map at the basic cycle length (BCL) of 1500 ms. An island of prolonged APD is evident in this map. (C) Map of APD gradient at the BCL of 1500 ms. This shows that the region of prolonged APD is surrounded by steeper APD gradients. (D) Map of CaTD at the BCL of 1500 ms. (E) From top to bottom: psudo-EKG (p-ECG), action potential (AP), and calcium transient (CaT) from locations (marked by asterisks in panel B) at sub-ENDO, sub-EPI and M-cell island.
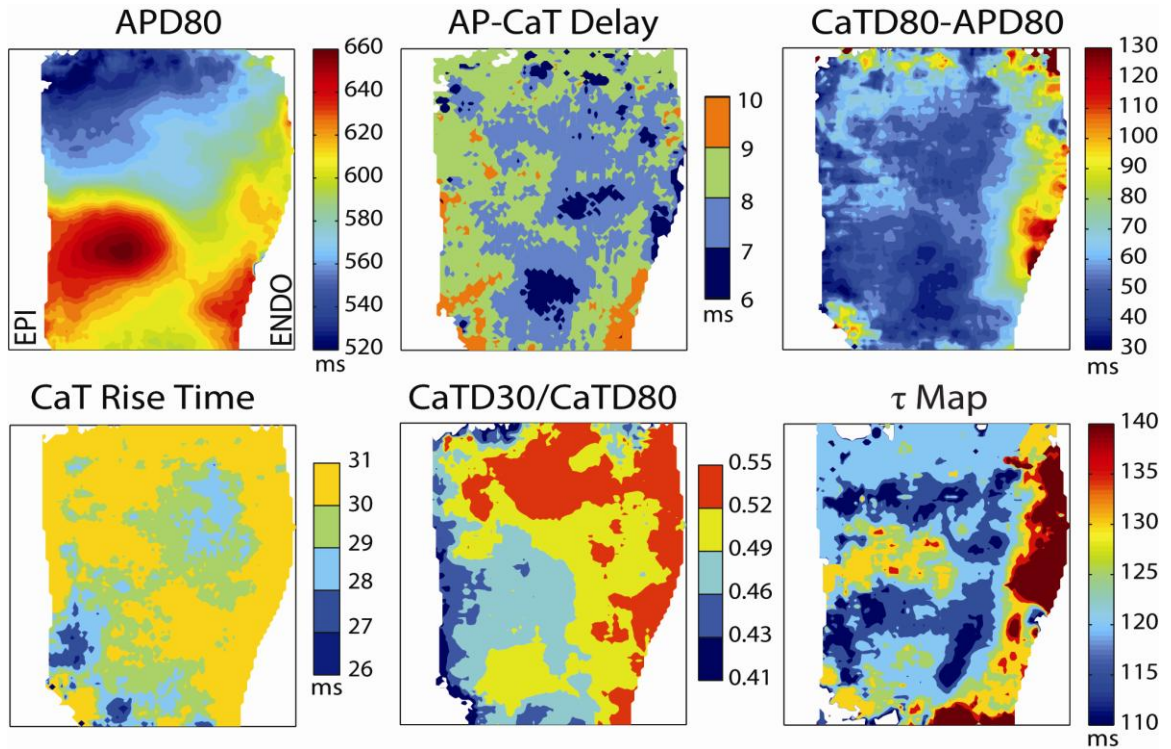
Figure 39. Quantifications of nonfailing heart #11 with an M-cell island. Here shows the maps for APD80, AP-CaT delay, CaTD80-APD80, rise time of CaT, CaTD30/CaTD80, and the CaT relaxation time constant (τ).

7.4.3 Morphological Changes of CaT

There were two morphological changes in CaT in the failing hearts compared with that in the nonfailing hearts. Figure 40A shows two representative examples of CaT recorded at the sub-ENDO of a failing (top) and a nonfailing heart (bottom). The first change was a "two-component" rising phase, including an initial fast rising phase (labeled by I in Figure 40A) and a subsequent second slow rising phase (labeled by II in Figure 40A). This was observed in 3 out of 5 failing hearts but not in any of the nonfailing hearts; and it was only present at sub-ENDO. The second slow component resulted in a significant increase of the rise time of CaT ($P < 0.001$) from 26 ± 3 ms (nonfailing and two failing) to 49 ± 12 ms (three failing)

111

at sub-ENDO. However, if a comparison is made between nonfailing and failing groups, this increase would not be statistically significant (See Figure 40B). The second morphological difference was a more flattened plateau of CaT within the failing group, which is reflected by an increased ratio of CaTD30 to CaTD80. Figure 40C shows that this ratio was significantly increased in failing hearts compared with nonfailing hearts at MID.
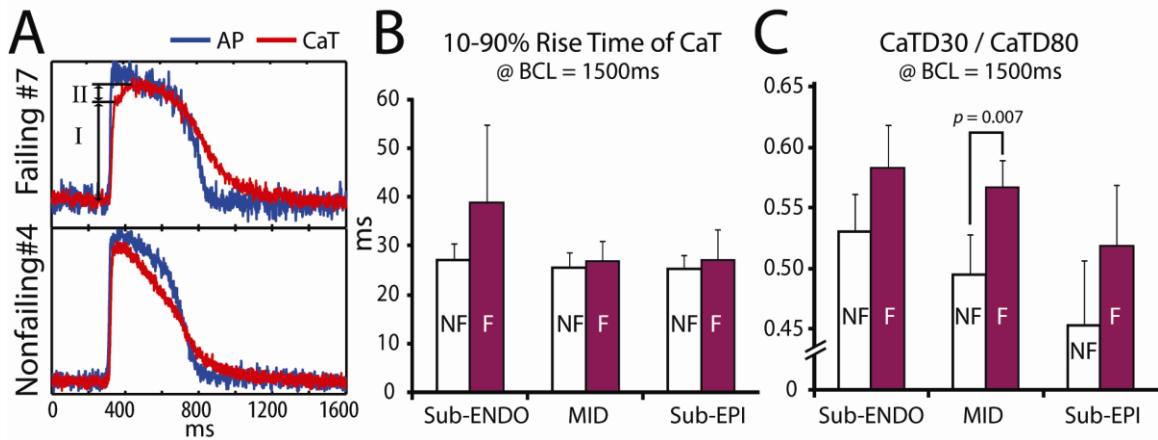
Figure 40. Remodeling of CaT due to heart failure. (A) Representative traces of action potential (AP) and calcium transient (CaT) from a failing heart and a nonfailing heart. (B) 10-90% rise time of CaT at a BCL of 1500ms in failing (F, n=5) and nonfailing (NF, n=6) hearts at sub-ENDO, MID and sub-EPI. (C) Ratio of CaTD30 and CaTD80 at a BCL of 1500ms at sub-ENDO, MID, and sub-EPI.

7.4.4 Relaxation of CaT

The time constant of CaT relaxation reflects the rate of Ca^{2+} reuptake from the cytoplasm by SERCA2a and Na^+/Ca^{2+} exchanger. We observed a gradient of the relaxation time constant of CaT from ENDO to EPI in both failing and nonfailing hearts. Figure 41A&B shows representative examples of the time constant measurement (τ) in a failing human heart. It is evident that τ at sub-ENDO was larger than that at sub-EPI. The difference between failing

and nonfailing groups was not statistically significant although there was a trend of an increase in τ within the failing group (Figure 41C).
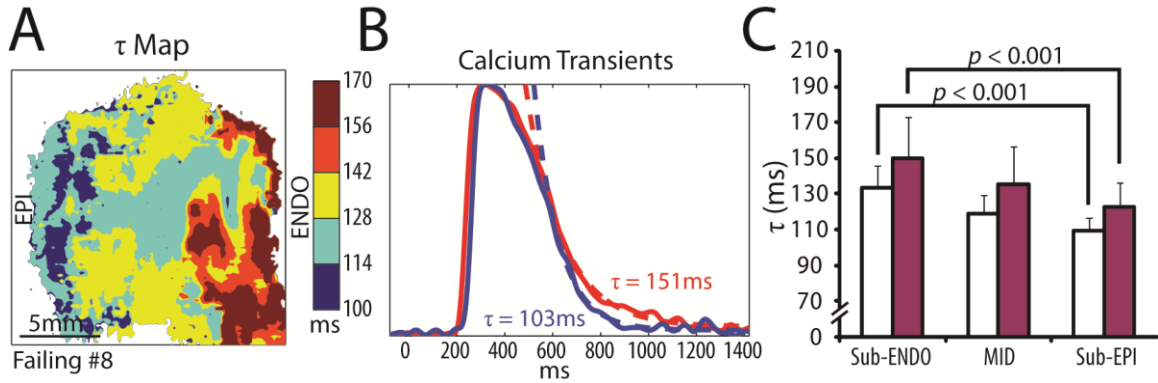
Figure 41. Relaxation of calcium transient (CaT). (A) Map of CaT relaxation time constant (□) from a failing human heart. (B) Representative traces of CaT (solid lines) from sub-ENDO (red) and sub-EPI (blue) and their corresponding single exponential fittings (dashed lines). (B) Summary of time constant (□□□ of CaT relaxation in failing (F, n=5) and nonfailing (NF, n=6) hearts at sub-ENDO, MID, sub-EPI at a BCL of 1500ms.

7.4.5 Protein Expression of SERCA2a and Phospholamban

To determine the molecular mechanism of the observed gradient of τ presented above, we quantified the protein expressions of SERCA2a and phospholamban. In Figure 42, representative bands and the statistical summary are shown for SERCA2a (Figure 42A) and phospholamban (Figure 42B). We divided our samples into three groups (See Table 2) including nonfailing, failing with ischemic cardiomyopathy, and failing with nonischemic/idiopathic cardiomyopathy. Each group was subdivided into sub-ENDO and sub-EPI. For SERCA2a, there was a significant difference between sub-ENDO and sub-EPI ($p < 0.001$, Figure 42A; interaction between tissue layers and patient groups was not significant [$P = 0.295$]). SERCA2a expression at sub-ENDO in the ischemic group was

significantly lower as compared to that in the nonischemic group (*P* = 0.023, Figure 42A).

For phospholamban, we did not observe any differences between sub-ENDO and sub-EPI,

nor among any of the three groups (Figure 42B).
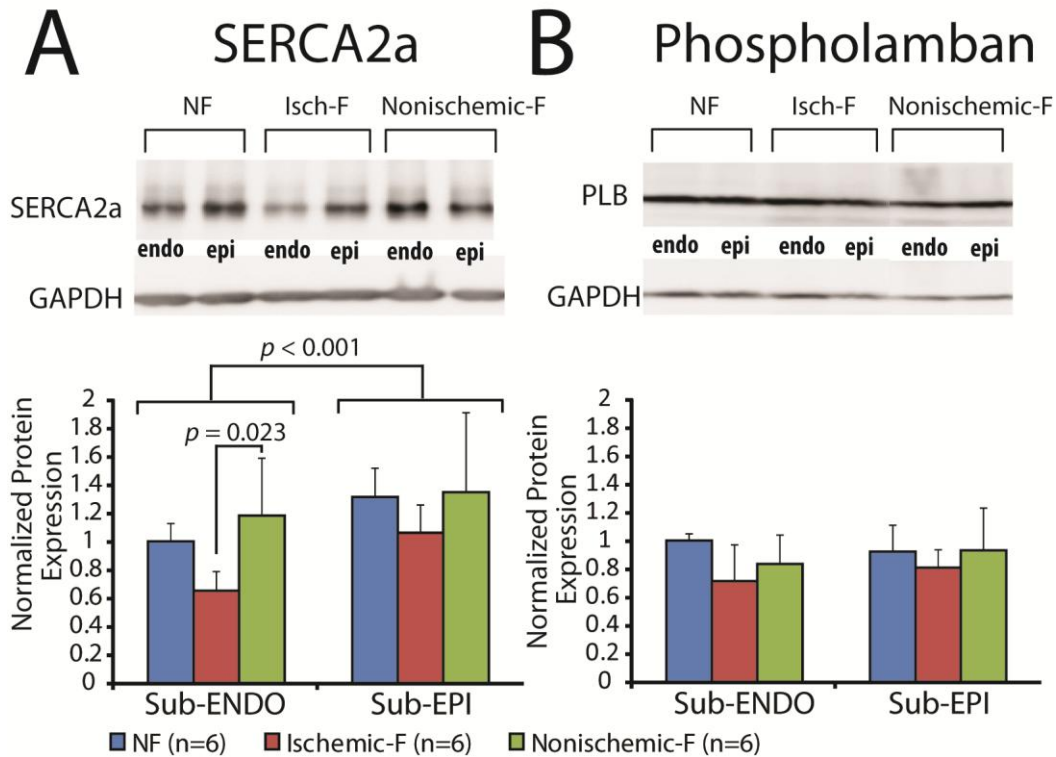
Figure 42. Protein expressions of SERCA2a and phospholamban. Representative examples of Western blots (top) and normalized protein expression (bottom) are shown for SERCA2a (A) and phospholamban (B). NF (n=6) represents the group of nonfailing hearts; Ischemic-F (n=6) represents the group of failing hearts with ischemic cardiomyopathy; Nonischemic-F (n=6) represents the group of failing hearts with nonischemic/idiopathic cardiomyopathy.

7.5 Discussions

In the present study, we conducted for the first time the simultaneous mapping of both

voltage and calcium in LV wedge preparations from failing and nonfailing human hearts. We

found that HF-induced remodeling consists of (1) increased differences of AP and CaT

durations at sub-ENDO during bradycardia (40 bpm), (2) decreased transmural CaTD gradients at fast pacing rates (100 bpm), (3) a slow component of rise and a dome-shaped plateau in CaT, and (4) a lowered level of SERCA2a expression at sub-ENDO in failing human hearts with ischemic cardiomyopathy. We also found that there existed transmural gradients of CaTD80, CaT relaxation time constant (τ), and protein expression of SERCA2a in both failing and nonfailing human hearts.

7.5.1 Implications from CaT Morphology Changes

There was a two-component rise of CaT at sub-ENDO in three of the failing hearts, with an initial fast component followed by a slow second component. This was previously observed in isolated myocytes from failing human and canine hearts (194, 203). Piacentino et al. suggested that this might result from increased Ca^{2+} entry during the AP plateau due to less calcium-mediated inactivation of L-type calcium currents and increased activity of the Na^+/Ca^{2+} exchanger in the reverse mode (Ca^{2+} influx) (203). The same mechanism could also explain the apparent dome shape of CaT observed in the failing hearts.

The morphological changes of CaT could also result from dyssynchronous Ca^{2+} release within a cell. The delayed release of Ca^{2+} in defective regions might be responsible for the slow component of rise and subsequent dome shape of CaT observed in the failing human hearts. Confocal line scan recordings in whole failing rat hearts revealed that the release of Ca^{2+} at some part within a cell does not occur at the time of initial depolarization but a short time after the depolarization (254). It is possible that the normal Ca^{2+} release corresponds to the first fast rising phase of CaT; and delayed Ca^{2+} release corresponds to the second slow component of CaT.

Interestingly, this slow secondary rise of CaT was observed only in sub-ENDO region in 60% of failing hearts. Further studies will be required to investigate the mechanisms of this remodeling at both molecular and tissue structural levels.

7.5.2 APD, CaTD, and (CaTD − APD)

The decay of CaT was markedly prolonged in isolated cells from failing human hearts (21). In contrast, CaTD in failing hearts was not statistically different from nonfailing hearts in our study. This is likely due to differences between isolated cell and tissue preparations as well as differences in the pacing cycle length. O'Rourke et al. showed that CaTD was 3-fold longer in myocytes from failing hearts at BCL of 6 seconds, but was not significantly different at 1-second interval when compared with myocytes from nonfailing hearts (194). Another possible explanation for this discrepancy is the afterload dependence of CaT, which indicates that mechanical work and metabolic demand is crucial for inducing the pathological regulation and morphological changes of CaT (246). Since mechanical work was inhibited in our study by blebbistatin to eliminate motion artifacts, changes of CaT therefore might not be as evident.

(CaTD - APD) was significantly increased at the sub-ENDO at a slow heart rate (40 bpm) in failing hearts as compared to nonfailing hearts (Figure 4A-right). That is, CaT significantly outlasts AP and is elevated during phase 3 of the AP. This difference in duration was previously proposed to promote late phase 3 early afterdepolarization (EAD) by the strong recruitment of electrogenic Na^+/Ca^{2+} exchanger currents (35, 195). Though EAD was not observed in this study, we speculate that this might contribute to the enhanced arrhythmogenesis in HF by promoting EADs under conditions such as metabolic inhibition.

116

7.5.3 Transmural CaTD Gradient

The transmural gradient of CaTD at fast heart rates (100 bpm) was significantly smaller in the failing group as compared to the nonfailing group. This might have important physiological implications relevant to the mechanical dysfunction of failing human hearts.

The transmural gradient of CaTD was 72 ± 20 ms and 81 ± 16 ms at a slow rate (40 bpm) for failing and nonfailing groups during ENDO pacing, respectively (Figure 4C-right). The corresponding conduction time from the ENDO to EPI was 49 ± 13 ms and 30 ± 5 ms (40 bpm). Therefore, the transmural gradient of the time at 80% of CaT relaxation from ENDO to EPI (ENDO to EPI CaTD80 difference minus conduction time) was 23 ± 15 ms and 51 ± 19 ms. The positivity of these values indicates that the sequence of relaxation of CaT was from EPI to ENDO for both failing and nonfailing groups at 40 bpm. This sequence is the same as the transmural sequence of myofiber relaxation measured in vivo in normal canine hearts during sinus rhythm (6).

At fast heart rates this sequence was maintained in nonfailing human hearts (as expected) but was reversed in failing human hearts. At 100 bpm in the failing group, the transmural gradient of CaTD was 25 ± 11 ms and conduction time increased to 57 ± 13 ms at (Figure 4C-right). Therefore, the transmural gradient of the time at 80% of CaT relaxation was -29 ± 15 ms, the negativity of which indicates that the sequence of CaT relaxation for the failing group was from ENDO to EPI. This reversed sequence of relaxation at fast heart rates could be associated with poor mechanical function and might be one of the mechanisms underlying the higher risk for primary composite endpoint in HF patients with higher heart rates (25).

7.5.4 Heterogeneous Calcium Handling

The protein expression of SERCA2a was significantly lower in ischemic failing hearts than the nonischemic failing hearts, at sub-ENDO but not at sub-EPI. This indicates that the protein level of SERCA2a is dependent on both the etiology of HF and the anatomic location of the myocardium. Previously, SERCA2a was found to be significantly down-regulated in failing human hearts in some studies (50, 109, 173, 240), while it was not in other studies (57, 82, 84, 152, 183, 185, 229). According to our results, the inconsistent observations might be related to the anatomic inconsistency within and across studies, and due to the etiology dependence of down-regulation.

In both failing and nonfailing hearts, the protein level of SERCA2a was less abundant at sub-ENDO than that at sub-EPI (Figure 8A). This difference was consistent with previous observations in canine and human hearts (140, 211). The lower expression of SERCA2a was suggested to lead to the larger relaxation time constant of CaT in canine hearts (140). Our results suggest that this causal relationship might also exist in human hearts.

No significant increase of the relaxation time constant was observed in failing human hearts in this study. Since our failing group consisted of two hearts with ischemic cardiomyopathy and three hearts with nonischemic/idiopathic cardiomyopathy for the functional part of this study, the lack of statistical significance could be explained by different etiologies of HF. Indeed, the time constant in hearts with ischemic cardiomyopathy was longer than in hearts with nonischemic/idiopathic cardiomyopathy (i.e., sub-ENDO: 170 ms vs. 136 ms; MID: 152 ms vs. 124 ms; sub-EPI: 137 ms vs. 114 ms). Due to limited samples, future studies are needed to test this hypothesis. Nevertheless, this hypothesis is supported by a study in isolated myocytes from human hearts with end-stage HF, which

showed that relaxation of CaT and contraction was significantly slower in hearts with ischemic cardiomyopathy than that with dilated cardiomyopathy (232). This difference might be explained by the significant down-regulation of SERCA2a protein expression in ischemic failing group but no change within the nonischemic failing group as shown in this study.

7.5.5 M Cell Island

We have recently reported (90) that the M cells were present in the form of spatially discrete and isolated islands rather than a continuous layer in 3 out of 5 nonfailing human hearts. Moreover, M cells were not observed in failing human hearts due to nonhomogeneous APD prolongation and decreased transmural APD gradient (90). In order to compare failing and nonfailing hearts under the same pattern of APD distribution, we did not concentrate on searching for M cell islands in nonfailing hearts. This explains why we only present M cells in one nonfailing heart (Figure 5). In this experiment, we specifically searched for M cells which were in the form of isolated islands rather than a continuous layer, as was previously described (90). The regions above and below the M cell island had continuous APD gradient from ENDO to EPI (similar to Figure 3). To compare failing and nonfailing hearts under the same pattern of APD distribution, data only in the region without M cells (e.g., upper part of Figure 5B) were used in the statistical analysis.

As shown in Figure 5D, CaTD within the M cell island was prominently longer compared to the neighboring region. However, CaTD within the M cell island (698±9 ms) was comparable to that at the sub-ENDO (711±15 ms, also see Figure 5D), while APD within the M cell island (649±7 ms) was longer than that at sub-ENDO (618±13 ms, also see Figure 5B). This difference is similar to the observation made in the canine study by Cordeiro et al.(45) Interestingly, other parameters related to EC coupling and calcium

handling (such as AP-CaT delay, CaT rise time and CaT relaxation time constant) were not distinctly different from the surrounding region (Supplemental Figure 2). The role of M cell islands in the contraction and their nature in nonfailing hearts remains unclear.

7.6 Limitations

This study has several limiations. First, nonfailing donor hearts are not necessarily representative of healthy hearts (190). However, none of the donors have a history of HF, and were thus the best controls available for this functional study. Second, due to technical limitations, only a limited transmural surface of LV with good perfusion was mapped. Due to the anatomical heterogeneity of the heart itself, caution should be taken to extrapolate the results to the whole heart. Third, due to the limited access to functional human hearts, the number of hearts for each group is small, and might compromise the statistical significance of potential differences. Because all of the failing hearts with different cardiomyopathy were grouped together for the functional data analysis, only changes common to different etiologies of cardiomyopathy could be revealed. Changes unique to individual cardiomyopathy could be masked. Fourth, several other important aspects of EC coupling were not examined in this study, such as the SR calcium content and the EC coupling gain. Regional differences of these parameters need to be resolved in future studies. Fifth, application of blebbistatin in our study liberated ATP from mechanical contraction and thus allowed ample supply of ATP to electrophysiological processes. Pathological changes could thus be less evident in the absence of metabolic disturbance that could be unmasked by mechanical work. Finally, as shown in neonatal rat myocyte cultures, the use of high-affinity dyes including Rhod-2 may overestimate CaTD, which was about twice as large as APD (71, 72). This was not likely the case in our measurements because CaTD in normal human

120

hearts was comparable to APD. Also, the main focus of the present study was on regional

differences of CaTDs rather than on their absolute values. Thus, potential systematic errors,

if they existed, were likely to be subtracted or minimized.

8. Summary and Future Directions

The panoramic imaging system has demonstrated its use in studying the dynamics of reentrant arrhythmias (149). The limitation of the current system is its relatively low spatially resolution due to the use of PDA (16 by 16). Incorporation of the high spatial resolution CMOS cameras into this system could significantly improve the performance and extend its application to large hearts (e.g. dog and human heart).

The dual imaging system has also proved its use in mouse, rabbit and human heart tissues. The current limitation of this system is the relative small size of the field of view, which can be improved by using the tandem lens configuration as showed by Laurita et al. (142).

We demonstrated that healed myocardial infarction could enhance the susceptibility to electrical alternans. This hypothesis will be tested in the failing human heart targeting the regions containing scars tissue. Histology of the tissue should follow the functional study to determine the correlation between the heterogeneous functional remodeling and structural remodeling.

As remodeling of repolarization on the RV endocardium was observed in the failing human heart, the next step of this study will be examination of the molecular mechanism by investigating the gene and protein expression of key ionic channels in tissue isolated from different regions of RV. Furthermore, functional, molecular and structural remodeling at the RV outflow tract will be quantified. And hypothesis regarding the distinctively high arrhythmogenesis at the RV outflow tract should be tested.

Regarding the study of EC coupling remodeling in failing human heart, we have established the "baseline remodeling". The next step is to first determine how the adrenergic stimulation would change the substrate and trigger for the ventricular arrhythmia, and then to simulate other conditions in vivo such as the loss of metabolic capability using metabolic inhibition. If optical mapping of beating heart without motion artifact could be achieved, electrical function and arrhythmia vulnerability should be tested before and after the application of EC uncoupler to determine whether the mechanical loading has an impact on the abnormal electrical function. It remains a question that under what conditions the DAD and EAD could occur in the failing human heart. Answering this question could potentially shed light to the prevention of arrhythmia triggers in human heart failure.

In summary, I think the continuing technical development and ongoing animal and human projects in the lab carry great promise in advancing the understanding of human cardiac electrophysiology and in opening the door for successful clinical translations to help combat the cardiovascular diseases such as heart failure.

Appendix A. Sketch of the Panoramic Imaging System

A sketch of the panoramic imaging system is shown in Figure 43.
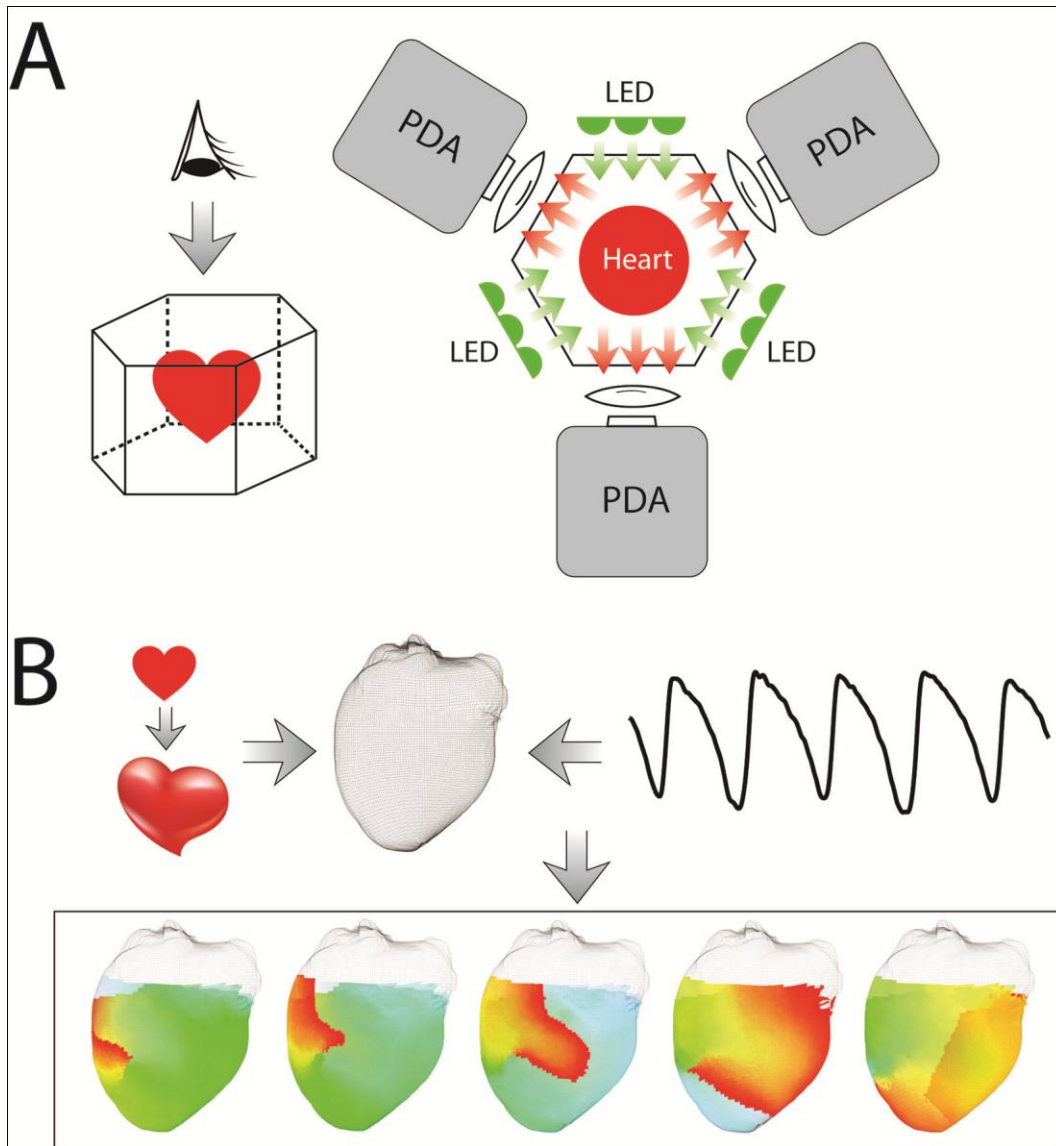
Figure 43. An overview sketch of the panoramic imaging system. (A) The hardware. The heart is placed in a hexagon-shaped chamber. Three photo-diode arrays (PDAs) are placed around the chamber. (B) The software. The geometry of the heart is first reconstructed. Then the optical signals from three PDAs are registered and textured onto the reconstructed surface. Reentrant arrhythmia can thus be easily visualized on the realistic single geometry.

Appendix B. Dual Imaging System for Simultaneous Measurement of Action Potential and Calcium Transient

The tissue is co-stained via coronary perfusion with voltage sensitive dye RH237 (30μL of 1.25mg/ml solution in DMSO, Invitrogen, Carlsbad, CA) and calcium indicator Rhod-2 AM (0.4-0.6mL of 1mg/ml solution in DMSO, Invitrogen, Carlsbad, CA).

   Two halogen lamps (Newport Oriel Instruments, Stratford, CT; SciMedia, Costa Mesa, CA) equipped with 520 ± 45nm bandpass filters are used for excitation. Fluorescent voltage and calcium signals are simultaneously collected from the same field of view. Fluorescence emission are separated by a dichroic mirror (635nm cutoff, Omega Optical, Brattleboro, VT), and filtered by a 700nm longpass filter (Thorlabs, Newton, New Jersey) for voltage signals and by a 590 ± 15nm bandpass filter (Omega Optical, Brattleboro, VT) for calcium signals. The two signals are then recorded by a dual CMOS camera system (ULTIMA-L, SciMedia, Costa Mesa, CA).

   A sketch of the dual imaging system is shown in Figure 44. Representative recordings of this system from a rabbit heart is shown in Figure 45.
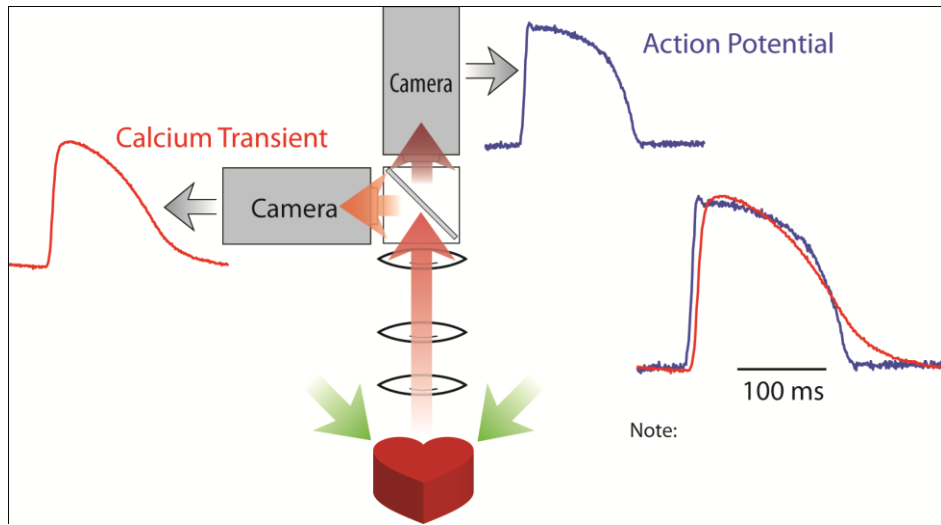
Figure 44. A sketch of the dual imaging system. The sample recordings are from a rabbit heart.
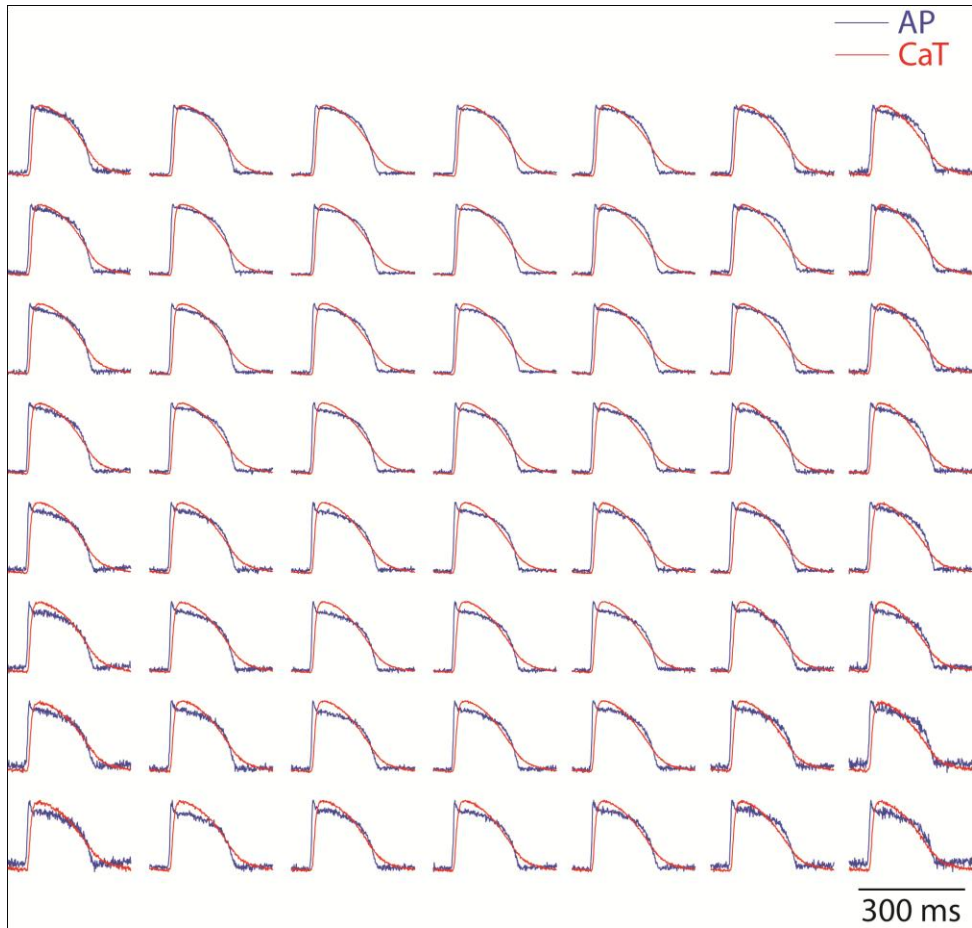
Figure 45. Sample recordings by an array of pixels from a rabbit heart.

126

References

1.   **Ai X, Curran JW, Shannon TR, Bers DM, and Pogwizd SM**. Ca2+/calmodulin-dependent protein kinase modulates cardiac ryanodine receptor phosphorylation and sarcoplasmic reticulum Ca2+ leak in heart failure. *Circ Res* 97: 1314-1322, 2005.

2.   **Aiba T, and Tomaselli GF**. Electrical remodeling in the failing heart. *Curr Opin Cardiol* 25: 29-36, 2010.

3.   **Akar FG, and Rosenbaum DS**. Transmural electrophysiological heterogeneities underlying arrhythmogenesis in heart failure. *Circ Res* 93: 638-645, 2003.

4.   **Allen DG, and Blinks JR**. Calcium transients in aequorin-injected frog cardiac muscle. *Nature* 273: 509-513, 1978.

5.   **Antzelevitch C**. Role of spatial dispersion of repolarization in inherited and acquired sudden cardiac death syndromes. *Am J Physiol Heart Circ Physiol* 293: H2024-2038, 2007.

6.   **Ashikaga H, Coppola BA, Hopenfeld B, Leifer ES, McVeigh ER, and Omens JH**. Transmural dispersion of myofiber mechanics: implications for electrical heterogeneity in vivo. *J Am Coll Cardiol* 49: 909-916, 2007.

7.   **Association AH**. Heart Disease and Stroke Statistics—2009 Update. *Circulation* 119: e21-e181, 2009.

8.   **Baker LC, Wolk R, Choi BR, Watkins S, Plan P, Shah A, and Salama G**. Effects of mechanical uncouplers, diacetyl monoxime, and cytochalasin-D on the electrophysiology of perfused mouse hearts. *Am J Physiol Heart Circ Physiol* 287: H1771-1779, 2004.

9.   **Barr CS, Naas A, Freeman M, Lang CC, and Struthers AD**. QT dispersion and sudden unexpected death in chronic heart failure. *Lancet* 343: 327-329, 1994.

10.   **Baudenbacher F, Schober T, Pinto JR, Sidorov VY, Hilliard F, Solaro RJ, Potter JD, and Knollmann BC**. Myofilament Ca2+ sensitization causes susceptibility to cardiac arrhythmia in mice. *J Clin Invest* 118: 3893-3903, 2008.

11.   **Bayly PV, KenKnight BH, Rogers JM, Hillsley RE, Ideker RE, and Smith WM**. Estimation of conduction velocity vector fields from epicardial mapping data. *IEEE Trans Biomed Eng* 45: 563-571, 1998.

12.   **Behrens S, Li C, and Franz MR**. Effects of myocardial ischemia on ventricular fibrillation inducibility and defibrillation efficacy. *J Am Coll Cardiol* 29: 817-824, 1997.

13.   **Belevych AE, Terentyev D, Viatchenko-Karpinski S, Terentyeva R, Sridhar A, Nishijima Y, Wilson LD, Cardounel AJ, Laurita KR, Carnes CA, Billman GE, and Gyorke S**. Redox modification of ryanodine receptors underlies calcium alternans in a canine model of sudden cardiac death. *Cardiovasc Res* 84: 387-395, 2009.

14.   **Benitah JP, Kerfant BG, Vassort G, Richard S, and Gomez AM**. Altered communication between L-type calcium channels and ryanodine receptors in heart failure. *Front Biosci* 7: e263-275, 2002.

15.   **Berridge MJ, Bootman MD, and Roderick HL**. Calcium signalling: dynamics, homeostasis and remodelling. *Nat Rev Mol Cell Biol* 4: 517-529, 2003.

16.   **Bers DM**. Calcium cycling and signaling in cardiac myocytes. *Annu Rev Physiol* 70: 23-49, 2008.

17.   **Bers DM**. Cardiac excitation-contraction coupling. *Nature* 415: 198-205, 2002.

18.   **Bers DM**. *Excitation-contraction coupling and cardiac contractile force*. Springer Netherlands, 2001.

19.   **Beuckelmann DJ, Nabauer M, and Erdmann E**. Alterations of K+ currents in isolated human ventricular myocytes from patients with terminal heart failure. *Circ Res* 73: 379-385, 1993.

20.   **Beuckelmann DJ, Nabauer M, and Erdmann E**. Characteristics of calcium-current in isolated human ventricular myocytes from patients with terminal heart failure. *J Mol Cell Cardiol* 23: 929-937, 1991.

21.   **Beuckelmann DJ, Nabauer M, and Erdmann E**. Intracellular calcium handling in isolated ventricular myocytes from patients with terminal heart failure. *Circulation* 85: 1046-1055, 1992.

22.   **Biermann M, Rubart M, Moreno A, Wu J, Josiah-Durant A, and Zipes DP**. Differential effects of cytochalasin D and 2,3 butanedione monoxime on isometric twitch force and transmembrane action potential in isolated ventricular muscle: implications for optical measurements of cardiac repolarization. *J Cardiovasc Electrophysiol* 9: 1348-1357, 1998.

23.   **Blinks JR, Wier WG, Hess P, and Prendergast FG**. Measurement of Ca2+ concentrations in living cells. *Prog Biophys Mol Biol* 40: 1-114, 1982.

24.   **Bohm M, Reiger B, Schwinger RH, and Erdmann E**. cAMP concentrations, cAMP dependent protein kinase activity, and phospholamban in non-failing and failing myocardium. *Cardiovasc Res* 28: 1713-1719, 1994.

25.   **Bohm M, Swedberg K, Komajda M, Borer JS, Ford I, Dubost-Brama A, Lerebours G, and Tavazzi L**. Heart rate as a risk factor in chronic heart failure (SHIFT): the association between heart rate and outcomes in a randomised placebo-controlled trial. *Lancet* 376: 886-894, 2010.

26.   **Bonatti V, Rolli A, and Botti G**. Recording of monophasic action potentials of the right ventricle in long QT syndromes complicated by severe ventricular arrhythmias. *Eur Heart J* 4: 168-179, 1983.

27.   **Bowling N, Walsh RA, Song G, Estridge T, Sandusky GE, Fouts RL, Mintze K, Pickard T, Roden R, Bristow MR, Sabbah HN, Mizrahi JL, Gromo G, King GL, and Vlahos CJ**. Increased protein kinase C activity and expression of Ca2+-sensitive isoforms in the failing human heart. *Circulation* 99: 384-391, 1999.

28.   **Bray MA, Lin SF, and Wikswo JP**. Three-dimensional surface reconstruction and fluorescent visualization of cardiac activation. *IEEE Trans Biomed Eng* 47: 1382-1391, 2000.

29.   **Bray MA, and Wikswo JP**. Considerations in phase plane analysis for nonstationary reentrant cardiac behavior. *Phys Rev E* 65: 051902, 2002.

30.   **Bray MA, and Wikswo JP**. Considerations in phase plane analysis for nonstationary reentrant cardiac behavior. *Phys Rev E Stat Nonlin Soft Matter Phys* 65: 051902, 2002.

31.   **Bray MA, and Wikswo JP**. Use of topological charge to determine filament location and dynamics in a numerical model of scroll wave activity. *IEEE Trans Biomed Eng* 49: 1086-1093, 2002.

32.   **Braz JC, Gregory K, Pathak A, Zhao W, Sahin B, Klevitsky R, Kimball TF, Lorenz JN, Nairn AC, Liggett SB, Bodi I, Wang S, Schwartz A, Lakatta EG, DePaoli-Roach AA, Robbins J, Hewett TE, Bibb JA, Westfall MV, Kranias EG, and Molkentin JD**. PKC-alpha regulates cardiac contractility and propensity toward heart failure. *Nat Med* 10: 248-254, 2004.

33.   **Bui AL, Horwich TB, and Fonarow GC**. Epidemiology and risk profile of heart failure. *Nat Rev Cardiol* 8: 30-41, 2011.

34.   **Burashnikov A, and Antzelevitch C**. Reinduction of atrial fibrillation immediately after termination of the arrhythmia is mediated by late phase 3 early afterdepolarization-induced triggered activity. *Circulation* 107: 2355-2360, 2003.

35.   **Burashnikov A, and Antzelevitch C**. Reinduction of atrial fibrillation immediately after termination of the arrhythmia is mediated by late phase 3 early afterdepolarization-induced triggered activity. *Circulation* 107: 2355-2360, 2003.

36.   **Cao JM, Qu Z, Kim YH, Wu TJ, Garfinkel A, Weiss JN, Karagueuzian HS, and Chen PS**. Spatiotemporal heterogeneity in the induction of ventricular fibrillation by rapid pacing: importance of cardiac restitution properties. *Circ Res* 84: 1318-1331, 1999.

37.   **Chaudhary KW, Rossman EI, Piacentino V, 3rd, Kenessey A, Weber C, Gaughan JP, Ojamaa K, Klein I, Bers DM, Houser SR, and Margulies KB**. Altered myocardial Ca2+ cycling after left ventricular assist device support in the failing human heart. *J Am Coll Cardiol* 44: 837-845, 2004.

38.   **Chauhan VS, Downar E, Nanthakumar K, Parker JD, Ross HJ, Chan W, and Picton P**. Increased ventricular repolarization heterogeneity in patients with ventricular arrhythmia vulnerability and cardiomyopathy: a human in vivo study. *Am J Physiol Heart Circ Physiol* 290: H79-86, 2006.

39.   **Cheng Y, Li L, Nikolski V, Wallick DW, and Efimov IR**. Shock-induced arrhythmogenesis is enhanced by 2,3-butanedione monoxime compared with cytochalasin D. *Am J Physiol Heart Circ Physiol* 286: H310-318, 2004.

40.   **Cheng Y, Mowrey KA, Wagoner DRV, Tchou PJ, and Efimov IR**. Virtual electrode-induced reexcitation : a mechanism of defibrillation. *Circ Res* 85: 1056-1066, 1999.

41.   **Cherry EM, and Fenton FH**. Suppression of alternans and conduction blocks despite steep APD restitution: electrotonic, memory, and conduction velocity restitution effects. *Am J Physiol Heart Circ Physiol* 286: H2332-2341, 2004.

42.   **Choi BR, and Salama G**. Simultaneous maps of optical action potentials and calcium transients in guinea-pig hearts: mechanisms underlying concordant alternans. *J Physiol* 529 Pt 1: 171-188, 2000.

43.   **Chudin E, Goldhaber J, Garfinkel A, Weiss J, and Kogan B**. Intracellular Ca(2+) dynamics and the stability of ventricular tachycardia. *Biophys J* 77: 2930-2941, 1999.

44.   **Clusin WT**. Mechanisms of calcium transient and action potential alternans in cardiac cells and tissues. *Am J Physiol Heart Circ Physiol* 294: H1-H10, 2008.

45.   **Cordeiro JM, Greene L, Heilmann C, Antzelevitch D, and Antzelevitch C**. Transmural heterogeneity of calcium activity and mechanical function in the canine left ventricle. *Am J Physiol Heart Circ Physiol* 286: H1471-1479, 2004.

46.   **Coulombe A, Lefevre IA, Deroubaix E, Thuringer D, and Coraboeuf E**. Effect of 2,3-butanedione 2-monoxime on slow inward and transient outward currents in rat ventricular myocytes. *J Mol Cell Cardiol* 22: 921-932, 1990.

47.   **Crossman DJ, Ruygrok PR, Soeller C, and Cannell MB**. Changes in the organization of excitation-contraction coupling structures in failing human heart. *PLoS One* 6: e17901, 2011.

48.   **Currie S, Loughrey CM, Craig MA, and Smith GL**. Calcium/calmodulin-dependent protein kinase IIdelta associates with the ryanodine receptor complex and regulates channel function in rabbit heart. *Biochem J* 377: 357-366, 2004.

49.   **Dash R, Frank KF, Carr AN, Moravec CS, and Kranias EG**. Gender influences on sarcoplasmic reticulum Ca2+-handling in failing human myocardium. *J Mol Cell Cardiol* 33: 1345-1353, 2001.

50.   **Dash R, Frank KF, Carr AN, Moravec CS, and Kranias EG**. Gender influences on sarcoplasmic reticulum Ca2+-handling in failing human myocardium. *J Mol Cell Cardiol* 33: 1345-1353, 2001.

51.   **de Bakker JM, van Capelle FJ, Janse MJ, Wilde AA, Coronel R, Becker AE, Dingemans KP, van Hemel NM, and Hauer RN**. Reentry as a cause of ventricular tachycardia in patients with chronic ischemic heart disease: electrophysiologic and anatomic correlation. *Circulation* 77: 589-606, 1988.

52.   **de Diego C, Chen F, Xie LH, Dave AS, Thu M, Rongey C, Weiss JN, and Valderrabano M**. Cardiac alternans in embryonic mouse ventricles. *Am J Physiol Heart Circ Physiol* 294: H433-440, 2008.

53.   **de Diego C, Pai RK, Dave AS, Lynch A, Thu M, Chen F, Xie LH, Weiss JN, and Valderrabano M**. Spatially discordant alternans in cardiomyocyte monolayers. *Am J Physiol Heart Circ Physiol* 294: H1417-1425, 2008.

54.   **De Koninck P, and Schulman H**. Sensitivity of CaM kinase II to the frequency of Ca2+ oscillations. *Science* 279: 227-230, 1998.

55.   **De Sousa E, Veksler V, Minajeva A, Kaasik A, Mateo P, Mayoux E, Hoerter J, Bigard X, Serrurier B, and Ventura-Clapier R**. Subcellular creatine kinase alterations. Implications in heart failure. *Circ Res* 85: 68-76, 1999.

56.   **del Monte F, Harding SE, Dec GW, Gwathmey JK, and Hajjar RJ**. Targeting phospholamban by gene transfer in human heart failure. *Circulation* 105: 904-907, 2002.

57.   **del Monte F, Harding SE, Schmidt U, Matsui T, Kang ZB, Dec GW, Gwathmey JK, Rosenzweig A, and Hajjar RJ**. Restoration of contractile function in isolated cardiomyocytes from failing human hearts by gene transfer of SERCA2a. *Circulation* 100: 2308-2311, 1999.

58.   **del Monte F, Williams E, Lebeche D, Schmidt U, Rosenzweig A, Gwathmey JK, Lewandowski ED, and Hajjar RJ**. Improvement in survival and cardiac metabolism after gene transfer of sarcoplasmic reticulum Ca(2+)-ATPase in a rat model of heart failure. *Circulation* 104: 1424-1429, 2001.

59.   **Derksen R, van Rijen HV, Wilders R, Tasseron S, Hauer RN, Rutten WL, and de Bakker JM**. Tissue discontinuities affect conduction velocity restitution: a mechanism by which structural barriers may promote wave break. *Circulation* 108: 882-888, 2003.

60.   **Dipla K, Mattiello JA, Margulies KB, Jeevanandam V, and Houser SR**. The sarcoplasmic reticulum and the Na+/Ca2+ exchanger both contribute to the Ca2+ transient of failing human ventricular myocytes. *Circ Res* 84: 435-444, 1999.

61.   **Dou Y, Arlock P, and Arner A**. Blebbistatin specifically inhibits actin-myosin interaction in mouse cardiac muscle. *Am J Physiol Cell Physiol* 293: C1148-1153, 2007.

62.   **Du YP, McVeigh ER, Bluemke DA, Silber HA, and Foo TK**. A comparison of prospective and retrospective respiratory navigator gating in 3D MR coronary angiography. *Int J Cardiovasc Imaging* 17: 287-294; discussion 295-286, 2001.

63.   **Efimov IR, Aguel F, Cheng Y, Wollenzier B, and Trayanova N**. Virtual electrode polarization in the far field: implications for external defibrillation. *Am J Physiol Heart Circ Physiol* 279: H1055-1070, 2000.

64.   **Efimov IR, Aguel F, Cheng Y, Wollenzier B, and Trayanova N**. Virtual electrode polarization in the far field: implications for external field. *Am J Physiol Heart Circ Physiol* 279: H1055-H1070, 2000.

65.   **Efimov IR, Cheng Y, Van Wagoner DR, Mazgalev T, and Tchou PJ**. Virtual electrode-induced phase singularity: a basic mechanism of defibrillation failure. *Circ Res* 82: 918-925, 1998.

66.   **Efimov IR, Cheng Y, Wagoner DRV, Mazgalev T, and Tchou PJ**. Virtual electrode-induced phase singularity : a basic mechanism of defibrillation failure. *Circ Res* 82: 918-925, 1998.

67.   **Efimov IR, Fedorov VV, Glukhov A, Lou Q, Ambrosi C, Janks D, Hucker WJ, Kurian T, Schuessler RB, and Moazami N**. Multiscale imaging of the human heart: Building the foundation for human systems physiology and translational medicine. *Conf Proc IEEE Eng Med Biol Soc* 2010: 5177-5180, 2010.

68.   **Efimov IR, Nikolski VP, and Salama G**. Optical imaging of the heart. *Circ Res* 95: 21-33, 2004.

69.   **el-Sherif N, Gough WB, and Restivo M**. Reentrant ventricular arrhythmias in the late myocardial infarction period: mechanism by which a short-long-short cardiac sequence facilitates the induction of reentry. *Circulation* 83: 268-278, 1991.

70.   **Fabritz CL, Kirchhof PF, Behrens S, Zabel M, and Franz MR**. Myocardial vulnerability to T wave shocks: relation to shock strength, shock coupling interval, and dispersion of ventricular repolarization. *J Cardiovasc Electrophysiol* 7: 231-242, 1996.

71.   **Fast VG**. Simultaneous optical imaging of membrane potential and intracellular calcium. *J Electrocardiol* 38: 107-112, 2005.

72.   **Fast VG, Cheek ER, Pollard AE, and Ideker RE**. Effects of electrical shocks on Ca_i^{2+} and V_m in myocyte cultures. *Circ Res* 94: 1589-1597, 2004.

73.   **Fedorov VV, Glukhov AV, Ambrosi CM, Kostecki G, Chang R, Janks D, Schuessler RB, Moazami N, Nichols CG, and Efimov IR**. Effects of K(ATP) channel openers diazoxide and pinacidil in coronary-perfused atria and ventricles from failing and non-failing human hearts. *J Mol Cell Cardiol* 2011.

74.   **Fedorov VV, Glukhov AV, Chang R, Kostecki G, Aferol H, Hucker WJ, Wuskell JP, Loew LM, Schuessler RB, Moazami N, and Efimov IR**. Optical mapping of the isolated coronary-perfused human sinus node. *J Am Coll Cardiol* 56: 1386-1394, 2010.

75.   **Fedorov VV, Lozinsky IT, Sosunov EA, Anyukhovsky EP, Rosen MR, Balke CW, and Efimov IR**. Application of blebbistatin as an excitation-contraction uncoupler for electrophysiologic study of rat and rabbit heart. *Heart rhythm* 4: 619-626, 2007.

76.   **Fedorov VV, Lozinsky IT, Sosunov EA, Anyukhovsky EP, Rosen MR, Balke CW, and Efimov IR**. Application of blebbistatin as an excitation-contraction uncoupler for electrophysiologic study of rat and rabbit hearts. *Heart rhythm* 4: 619-626, 2007.

77.   **Fedorov VV, Lozinsky IT, Sosunov EA, Anyukhovsky EP, Rosen MR, Balke CW, and Efimov IR**. Application of blebbistatin as an excitation-contraction uncoupler for electrophysiologic study of rat and rabbit hearts. *Heart Rhythm* 4: 619-626, 2007.

78.   **Fedorov VV, Schuessler RB, Hemphill M, Ambrosi CM, Chang R, Voloshina AS, Brown K, Hucker WJ, and Efimov IR**. Structural and functional evidence for discrete exit pathways that connect the canine sinoatrial node and atria. *Circ Res* 104: 915-923, 2009.

79.   **Feldman MD, Alderman JD, Aroesty JM, Royal HD, Ferguson JJ, Owen RM, Grossman W, and McKay RG**. Depression of systolic and diastolic myocardial reserve

during atrial pacing tachycardia in patients with dilated cardiomyopathy. *J Clin Invest* 82: 1661-1669, 1988.

80.   **Fenton FH, Cherry EM, and Kornreich BG**. Termination of equine atrial fibrillation by quinidine: an optical mapping study. *J Vet Cardiol* 10: 87-103, 2008.

81.   **Figueredo VM, Brandes R, Weiner MW, Massie BM, and Camacho SA**. Endocardial versus epicardial differences of intracellular free calcium under normal and ischemic conditions in perfused rat hearts. *Circ Res* 72: 1082-1090, 1993.

82.   **Flesch M, Schwinger RH, Schnabel P, Schiffer F, van Gelder I, Bavendiek U, Sudkamp M, Kuhn-Regnier F, and Bohm M**. Sarcoplasmic reticulum Ca2+ATPase and phospholamban mRNA and protein levels in end-stage heart failure due to ischemic or dilated cardiomyopathy. *J Mol Med* 74: 321-332, 1996.

83.   **Francis GS**. Development of arrhythmias in the patient with congestive heart failure: pathophysiology, prevalence and prognosis. *Am J Cardiol* 57: 3B-7B, 1986.

84.   **Frank K, Bolck B, Bavendiek U, and Schwinger RH**. Frequency dependent force generation correlates with sarcoplasmic calcium ATPase activity in human myocardium. *Basic Res Cardiol* 93: 405-411, 1998.

85.   **Frank KF, Bolck B, Brixius K, Kranias EG, and Schwinger RH**. Modulation of SERCA: implications for the failing human heart. *Basic Res Cardiol* 97 Suppl 1: I72-78, 2002.

86.   **Fu GS, Meissner A, and Simon R**. Repolarization dispersion and sudden cardiac death in patients with impaired left ventricular function. *Eur Heart J* 18: 281-289, 1997.

87.   **Garcia-Dorado D, Theroux P, Duran JM, Solares J, Alonso J, Sanz E, Munoz R, Elizaga J, Botas J, Fernandez-Aviles F, and et al.** Selective inhibition of the contractile apparatus. A new approach to modification of infarct size, infarct composition, and infarct geometry during coronary artery occlusion and reperfusion. *Circulation* 85: 1160-1174, 1992.

88.   **Garrey WE**. The nature of fibrillary contraction of the heart.—Its relation to tissue mass and form. *American Journal of Physiology--Legacy Content* 33: 397, 1914.

89.   **Glukhov AV, Fedorov VV, Lou Q, Ravikumar VK, Kalish PW, Schuessler RB, Moazami N, and Efimov IR**. Transmural dispersion of repolarization in failing and nonfailing human ventricle. *Circ Res* 106: 981-991, 2010.

90.   **Glukhov AV, Fedorov VV, Lou Q, Ravikumar VK, Kalish PW, Schuessler RB, Moazami N, and Efimov IR**. Transmural dispersion of repolarization in failing and nonfailing human ventricle. *Circ Res* 106: 981-991, 2010.

91.   **Goldhaber JI, Xie LH, Duong T, Motter C, Khuu K, and Weiss JN**. Action potential duration restitution and alternans in rabbit ventricular myocytes: the key role of intracellular calcium cycling. *Circ Res* 96: 459-466, 2005.

92.   **Gomez AM, Valdivia HH, Cheng H, Lederer MR, Santana LF, Cannell MB, McCune SA, Altschuld RA, and Lederer WJ**. Defective excitation-contraction coupling in experimental cardiac hypertrophy and heart failure. *Science* 276: 800-806, 1997.

93.   **Gough WB, Mehra R, Restivo M, Zeiler RH, and el-Sherif N**. Reentrant ventricular arrhythmias in the late myocardial infarction period in the dog. 13. Correlation of activation and refractory maps. *Circ Res* 57: 432-442, 1985.

94.   **Gwathmey JK, Copelas L, MacKinnon R, Schoen FJ, Feldman MD, Grossman W, and Morgan JP**. Abnormal intracellular calcium handling in myocardium from patients with end-stage heart failure. *Circ Res* 61: 70-76, 1987.

95.   **Gwathmey JK, Copelas L, MacKinnon R, Schoen FJ, Feldman MD, Grossman W, and Morgan JP**. Abnormal intracellular calcium handling in myocardium from patients with end-stage heart failure. *Circ Res* 61: 70-76, 1987.

96.   **Gwathmey JK, Slawsky MT, Hajjar RJ, Briggs GM, and Morgan JP**. Role of intracellular calcium handling in force-interval relationships of human ventricular myocardium. *J Clin Invest* 85: 1599-1613, 1990.

97.   **Gwathmey JK, Warren SE, Briggs GM, Copelas L, Feldman MD, Phillips PJ, Callahan M, Jr., Schoen FJ, Grossman W, and Morgan JP**. Diastolic dysfunction in hypertrophic cardiomyopathy. Effect on active force generation during systole. *J Clin Invest* 87: 1023-1031, 1991.

98.   **Hain J, Onoue H, Mayrleitner M, Fleischer S, and Schindler H**. Phosphorylation modulates the function of the calcium release channel of sarcoplasmic reticulum from cardiac muscle. *J Biol Chem* 270: 2074-2081, 1995.

99.   **Hambleton M, Hahn H, Pleger ST, Kuhn MC, Klevitsky R, Carr AN, Kimball TF, Hewett TE, Dorn GW, 2nd, Koch WJ, and Molkentin JD**. Pharmacological- and gene therapy-based inhibition of protein kinase Calpha/beta enhances cardiac contractility and attenuates heart failure. *Circulation* 114: 574-582, 2006.

100.   **Han J, and Moe GK**. Nonuniform Recovery of Excitability in Ventricular Muscle. *Circ Res* 14: 44-60, 1964.

101.   **Hao SC, Christini DJ, Stein KM, Jordan PN, Iwai S, Bramwell O, Markowitz SM, Mittal S, and Lerman BB**. Effect of beta-adrenergic blockade on dynamic electrical restitution in vivo. *Am J Physiol Heart Circ Physiol* 287: H390-394, 2004.

102.   **Harada M, Honjo H, Yamazaki M, Nakagawa H, Ishiguro YS, Okuno Y, Ashihara T, Sakuma I, Kamiya K, and Kodama I**. Moderate hypothermia increases the chance of spiral wave collision in favor of self-termination of ventricular tachycardia/fibrillation. *Am J Physiol Heart Circ Physiol* 294: H1896-1905, 2008.

103.   **Hasenfuss G, Maier LS, Hermann HP, Luers C, Hunlich M, Zeitz O, Janssen PM, and Pieske B**. Influence of pyruvate on contractile performance and Ca(2+) cycling in isolated failing human myocardium. *Circulation* 105: 194-199, 2002.

104.   **Hasenfuss G, Mulieri LA, Leavitt BJ, Allen PD, Haeberle JR, and Alpert NR**. Alteration of contractile function and excitation-contraction coupling in dilated cardiomyopathy. *Circ Res* 70: 1225-1232, 1992.

105.   **Hasenfuss G, Mulieri LA, Leavitt BJ, Allen PD, Haeberle JR, and Alpert NR**. Alteration of contractile function and excitation-contraction coupling in dilated cardiomyopathy. *Circ Res* 70: 1225-1232, 1992.

106.   **Hasenfuss G, and Pieske B**. Calcium cycling in congestive heart failure. *J Mol Cell Cardiol* 34: 951-969, 2002.

107.   **Hasenfuss G, Pieske B, Holubarsch C, Alpert NR, and Just H**. Excitation-contraction coupling and contractile protein function in failing and nonfailing human myocardium. *Adv Exp Med Biol* 346: 91-100, 1993.

108.   **Hasenfuss G, Reinecke H, Studer R, Meyer M, Pieske B, Holtz J, Holubarsch C, Posival H, Just H, and Drexler H**. Relation between myocardial function and expression of sarcoplasmic reticulum Ca(2+)-ATPase in failing and nonfailing human myocardium. *Circ Res* 75: 434-442, 1994.

109.   **Hasenfuss G, Reinecke H, Studer R, Meyer M, Pieske B, Holtz J, Holubarsch C, Posival H, Just H, and Drexler H**. Relation between myocardial function and

expression of sarcoplasmic reticulum Ca(2+)-ATPase in failing and nonfailing human myocardium. *Circ Res* 75: 434-442, 1994.

110.   **Hayashi H, Miyauchi Y, Chou CC, Karagueuzian HS, Chen PS, and Lin SF**. Effects of cytochalasin D on electrical restitution and the dynamics of ventricular fibrillation in isolated rabbit heart. *J Cardiovasc Electrophysiol* 14: 1077-1084, 2003.

111.   **Hayashi H, Shiferaw Y, Sato D, Nihei M, Lin SF, Chen PS, Garfinkel A, Weiss JN, and Qu Z**. Dynamic origin of spatially discordant alternans in cardiac tissue. *Biophys J* 92: 448-460, 2007.

112.   **Hobai IA, and O'Rourke B**. Decreased sarcoplasmic reticulum calcium content is responsible for defective excitation-contraction coupling in canine heart failure. *Circulation* 103: 1577-1584, 2001.

113.   **Holmberg SR, and Williams AJ**. Single channel recordings from human cardiac sarcoplasmic reticulum. *Circ Res* 65: 1445-1449, 1989.

114.   **Houser SR**. Reduced abundance of transverse tubules and L-type calcium channels: another cause of defective contractility in failing ventricular myocytes. *Cardiovasc Res* 49: 253-256, 2001.

115.   **Ikeda T, Saito H, Tanno K, Shimizu H, Watanabe J, Ohnishi Y, Kasamaki Y, and Ozawa Y**. T-wave alternans as a predictor for sudden cardiac death after myocardial infarction. *Am J Cardiol* 89: 79-82, 2002.

116.   **Inserte J, Garcia-Dorado D, Hernando V, and Soler-Soler J**. Calpain-mediated impairment of Na+/K+-ATPase activity during early reperfusion contributes to cell death after myocardial ischemia. *Circ Res* 97: 465-473, 2005.

117.   **Jantunen E, and Collan Y**. Transmural differences in ischaemic heart disease: a quantitative histologic study. *Appl Pathol* 7: 179-187, 1989.

118.   **Jaski BE, Jessup ML, Mancini DM, Cappola TP, Pauly DF, Greenberg B, Borow K, Dittrich H, Zsebo KM, and Hajjar RJ**. Calcium upregulation by percutaneous administration of gene therapy in cardiac disease (CUPID Trial), a first-in-human phase 1/2 clinical trial. *J Card Fail* 15: 171-181, 2009.

119.   **Jiang MT, Lokuta AJ, Farrell EF, Wolff MR, Haworth RA, and Valdivia HH**. Abnormal Ca2+ release, but normal ryanodine receptors, in canine and human heart failure. *Circ Res* 91: 1015-1022, 2002.

120.   **Jou CJ, Spitzer KW, and Tristani-Firouzi M**. Blebbistatin effectively uncouples the excitation-contraction process in zebrafish embryonic heart. *Cell Physiol Biochem* 25: 419-424, 2010.

121.   **Kalb SS, Dobrovolny HM, Tolkacheva EG, Idriss SF, Krassowska W, and Gauthier DJ**. The restitution portrait: a new method for investigating rate-dependent restitution. *J Cardiovasc Electrophysiol* 15: 698-709, 2004.

122.   **Katz AM**. Cardiomyopathy of overload. A major determinant of prognosis in congestive heart failure. *N Engl J Med* 322: 100-110, 1990.

123.   **Kawara T, Derksen R, de Groot JR, Coronel R, Tasseron S, Linnenbank AC, Hauer RN, Kirkels H, Janse MJ, and de Bakker JM**. Activation delay after premature stimulation in chronically diseased human myocardium relates to the architecture of interstitial fibrosis. *Circulation* 104: 3069-3075, 2001.

124.   **Kay MW, Amison PM, and Rogers JM**. Three-dimensional surface reconstruction and panoramic optical mapping of large hearts. *IEEE Trans Biomed Eng* 51: 1219-1229, 2004.

125.	**Kelly A, Kemi OJ, Ghouri IA, Burton FL, Myles RC, and Smith GL**. Comparison of Action Potential Characteristics from Intact Rabbit Myocardium Using 2-Photon Excitation, Widefield Epifluorescence and Microelectrode Recordings. *Biophysical Journal* 100: 576a, 2011.

126.	**Kikuchi K, Holdway JE, Werdich AA, Anderson RM, Fang Y, Egnaczyk GF, Evans T, Macrae CA, Stainier DY, and Poss KD**. Primary contribution to zebrafish heart regeneration by gata4(+) cardiomyocytes. *Nature* 464: 601-605, 2010.

127.	**Kirchhefer U, Schmitz W, Scholz H, and Neumann J**. Activity of cAMP-dependent protein kinase and Ca2+/calmodulin-dependent protein kinase in failing and nonfailing human hearts. *Cardiovasc Res* 42: 254-261, 1999.

128.	**Koller ML, Maier SK, Gelzer AR, Bauer WR, Meesmann M, and Gilmour RF, Jr.** Altered dynamics of action potential restitution and alternans in humans with structural heart disease. *Circulation* 112: 1542-1548, 2005.

129.	**Kong W, Ideker RE, and Fast VG**. Transmural optical measurements of Vm dynamics during long-duration ventricular fibrillation in canine hearts. *Heart rhythm* 6: 796-802, 2009.

130.	**Konta T, Ikeda K, Yamaki M, Nakamura K, Honma K, Kubota I, and Yasui S**. Significance of discordant ST alternans in ventricular fibrillation. *Circulation* 82: 2185-2189, 1990.

131.	**Koumi S, Backer CL, and Arentzen CE**. Characterization of inwardly rectifying K+ channel in human cardiac myocytes. Alterations in channel behavior in myocytes isolated from patients with idiopathic dilated cardiomyopathy. *Circulation* 92: 164-174, 1995.

132.	**Kubalova Z, Terentyev D, Viatchenko-Karpinski S, Nishijima Y, Gyorke I, Terentyeva R, da Cunha DN, Sridhar A, Feldman DS, Hamlin RL, Carnes CA, and Gyorke S**. Abnormal intrastore calcium signaling in chronic heart failure. *Proc Natl Acad Sci U S A* 102: 14104-14109, 2005.

133.	**Kubo H, Margulies KB, Piacentino V, 3rd, Gaughan JP, and Houser SR**. Patients with end-stage congestive heart failure treated with beta-adrenergic receptor antagonists have improved ventricular myocyte calcium regulatory protein abundance. *Circulation* 104: 1012-1018, 2001.

134.	**Kuo CS, Munakata K, Reddy CP, and Surawicz B**. Characteristics and possible mechanism of ventricular arrhythmia dependent on the dispersion of action potential durations. *Circulation* 67: 1356-1367, 1983.

135.	**Kurita T, Shimizu W, Inagaki M, Suyama K, Taguchi A, Satomi K, Aihara N, Kamakura S, Kobayashi J, and Kosakai Y**. The electrophysiologic mechanism of ST-segment elevation in Brugada syndrome. *J Am Coll Cardiol* 40: 330-334, 2002.

136.	**Kushnir A, Shan J, Betzenhauser MJ, Reiken S, and Marks AR**. Role of CaMKIIdelta phosphorylation of the cardiac ryanodine receptor in the force frequency relationship and heart failure. *Proc Natl Acad Sci U S A* 107: 10274-10279, 2010.

137.	**Lab MJ, and Lee JA**. Changes in intracellular calcium during mechanical alternans in isolated ferret ventricular muscle. *Circ Res* 66: 585-595, 1990.

138.	**Laurita KR, Girouard SD, Akar FG, and Rosenbaum DS**. Modulated dispersion explains changes in arrhythmia vulnerability during premature stimulation of the heart. *Circulation* 98: 2774-2780, 1998.

139.	**Laurita KR, Girouard SD, and Rosenbaum DS**. Modulation of ventricular repolarization by a premature stimulus. Role of epicardial dispersion of repolarization

kinetics demonstrated by optical mapping of the intact guinea pig heart. *Circ Res* 79: 493-503, 1996.

140.   **Laurita KR, Katra R, Wible B, Wan X, and Koo MH**. Transmural heterogeneity of calcium handling in canine. *Circ Res* 92: 668-675, 2003.

141.   **Laurita KR, and Katra RP**. Delayed after depolarization-mediated triggered activity associated with slow calcium sequestration near the endocardium. *J Cardiovasc Electrophysiol* 16: 418-424, 2005.

142.   **Laurita KR, and Singal A**. Mapping action potentials and calcium transients simultaneously from the intact heart. *Am J Physiol Heart Circ Physiol* 280: H2053-2060, 2001.

143.   **Lee MH, Lin SF, Ohara T, Omichi C, Okuyama Y, Chudin E, Garfinkel A, Weiss JN, Karagueuzian HS, and Chen PS**. Effects of diacetyl monoxime and cytochalasin D on ventricular fibrillation in swine right ventricles. *Am J Physiol Heart Circ Physiol* 280: H2689-2696, 2001.

144.   **Lehnart SE, Wehrens XH, Reiken S, Warrier S, Belevych AE, Harvey RD, Richter W, Jin SL, Conti M, and Marks AR**. Phosphodiesterase 4D deficiency in the ryanodine-receptor complex promotes heart failure and arrhythmias. *Cell* 123: 25-35, 2005.

145.   **Leuthardt EC, Wippold FJ, 2nd, Oswood MC, and Rich KM**. Diffusion-weighted MR imaging in the preoperative assessment of brain abscesses. *Surg Neurol* 58: 395-402; discussion 402, 2002.

146.   **Li GR, Lau CP, Ducharme A, Tardif JC, and Nattel S**. Transmural action potential and ionic current remodeling in ventricles of failing canine hearts. *Am J Physiol Heart Circ Physiol* 283: H1031-1041, 2002.

147.   **Li GR, Lau CP, Leung TK, and Nattel S**. Ionic current abnormalities associated with prolonged action potentials in cardiomyocytes from diseased human right ventricles. *Heart Rhythm* 1: 460-468, 2004.

148.   **Li L, Nikolski V, Wallick DW, Efimov IR, and Cheng Y**. Mechanisms of enhanced shock-induced arrhythmogenesis in the rabbit heart with healed myocardial infarction. *Am J Physiol Heart Circ Physiol* 289: H1054-1068, 2005.

149.   **Li W, Ripplinger CM, Lou Q, and Efimov IR**. Multiple monophasic shocks improve electrotherapy of ventricular tachycardia in a rabbit model of chronic infarction. *Heart rhythm* 6: 1020-1027, 2009.

150.   **Li Y, Kranias EG, Mignery GA, and Bers DM**. Protein kinase A phosphorylation of the ryanodine receptor does not affect calcium sparks in mouse ventricular myocytes. *Circ Res* 90: 309-316, 2002.

151.   **Lin SF, and Wikswo JP**. Panoramic optical imaging of electrical propagation in isolated heart. *J Biomed Optic* 4: 200-207, 1999.

152.   **Linck B, Boknik P, Eschenhagen T, Muller FU, Neumann J, Nose M, Jones LR, Schmitz W, and Scholz H**. Messenger RNA expression and immunological quantification of phospholamban and SR-Ca(2+)-ATPase in failing and nonfailing human hearts. *Cardiovasc Res* 31: 625-632, 1996.

153.   **Lindner M, Brandt MC, Sauer H, Hescheler J, Bohle T, and Beuckelmann DJ**. Calcium sparks in human ventricular cardiomyocytes from patients with terminal heart failure. *Cell Calcium* 31: 175-182, 2002.

154.   **Lindner M, Erdmann E, and Beuckelmann DJ**. Calcium content of the sarcoplasmic reticulum in isolated ventricular myocytes from patients with terminal heart failure. *J Mol Cell Cardiol* 30: 743-749, 1998.

155. **Litwin SE, and Morgan JP**. Captopril enhances intracellular calcium handling and beta-adrenergic responsiveness of myocardium from rats with postinfarction failure. *Circ Res* 71: 797-807, 1992.

156. **Liu Q, Chen X, Macdonnell SM, Kranias EG, Lorenz JN, Leitges M, Houser SR, and Molkentin JD**. Protein kinase C{alpha}, but not PKC{beta} or PKC{gamma}, regulates contractility and heart failure susceptibility: implications for ruboxistaurin as a novel therapeutic approach. *Circ Res* 105: 194-200, 2009.

157. **Lloyd-Jones D, Adams RJ, Brown TM, Carnethon M, Dai S, De Simone G, Ferguson TB, Ford E, Furie K, and Gillespie C**. Heart disease and stroke statistics--2010 update: a report from the American Heart Association. *Circulation* 121: e46, 2010.

158. **Lopatin AN, and Nichols CG**. 2,3-Butanedione monoxime (BDM) inhibition of delayed rectifier DRK1 (Kv2.1) potassium channels expressed in Xenopus oocytes. *J Pharmacol Exp Ther* 265: 1011-1016, 1993.

159. **Lou Q, Fedorov VV, Glukhov AV, Moazami N, Fast VG, and Efimov IR**. Transmural heterogeneity and remodeling of ventricular excitation-contraction coupling in human heart failure. *Circulation* 123: 1881-1890, 2011.

160. **Lou Q, Fedorov VV, Glukhov AV, Moazami N, Fast VG, and Efimov IR**. Transmural heterogeneity and remodeling of ventricular excitation-contraction coupling in human heart failure. *Circulation* 123: 1881-1890, 2011.

161. **Lou Q, Li W, and Efimov IR**. Multiparametric Optical Mapping of the Langendorff-perfused Rabbit Heart. *J Vis Exp* e3160, 2011.

162. **Lou Q, Ripplinger CM, Bayly PV, and Efimov IR**. Quantitative panoramic imaging of epicardial electrical activity. *Ann Biomed Eng* 36: 1649-1658, 2008.

163. **Louch WE, Bito V, Heinzel FR, Macianskiene R, Vanhaecke J, Flameng W, Mubagwa K, and Sipido KR**. Reduced synchrony of Ca2+ release with loss of T-tubules-a comparison to Ca2+ release in human failing cardiomyocytes. *Cardiovasc Res* 62: 63-73, 2004.

164. **Lyon AR, MacLeod KT, Zhang Y, Garcia E, Kanda GK, Lab MJ, Korchev YE, Harding SE, and Gorelik J**. Loss of T-tubules and other changes to surface topography in ventricular myocytes from failing human and rat heart. *Proc Natl Acad Sci U S A* 106: 6854-6859, 2009.

165. **Mackiewicz U, Maczewski M, Konior A, Tellez JO, Nowis D, Dobrzynski H, Boyett MR, and Lewartowski B**. Sarcolemmal Ca2+-ATPase ability to transport Ca2+ gradually diminishes after myocardial infarction in the rat. *Cardiovasc Res* 81: 546-554, 2009.

166. **Maier LS, and Bers DM**. Role of Ca2+/calmodulin-dependent protein kinase (CaMK) in excitation-contraction coupling in the heart. *Cardiovasc Res* 73: 631-640, 2007.

167. **Manoach M, Netz H, Erez M, and Weinstock M**. Ventricular self-defibrillation in mammals: age and drug dependence. *Age Ageing* 9: 112-116, 1980.

168. **Mantravadi R, Gabris B, Liu T, Choi BR, de Groat WC, Ng GA, and Salama G**. Autonomic nerve stimulation reverses ventricular repolarization sequence in rabbit hearts. *Circ Res* 100: e72-80, 2007.

169. **Marx SO, Reiken S, Hisamatsu Y, Jayaraman T, Burkhoff D, Rosemblit N, and Marks AR**. PKA phosphorylation dissociates FKBP12.6 from the calcium release channel (ryanodine receptor): defective regulation in failing hearts. *Cell* 101: 365-376, 2000.

170. **Mazzanti M, Assandri R, Ferroni A, and DiFrancesco D**. Cytoskeletal control of rectification and expression of four substates in cardiac inward rectifier K+ channels. *FASEB J* 10: 357-361, 1996.

171.   **Meinertz T, Hofmann T, Kasper W, Treese N, Bechtold H, Stienen U, Pop T, Leitner ER, Andresen D, and Meyer J**. Significance of ventricular arrhythmias in idiopathic dilated cardiomyopathy. *Am J Cardiol* 53: 902-907, 1984.
172.   **Mewes T, and Ravens U**. L-type calcium currents of human myocytes from ventricle of non-failing and failing hearts and from atrium. *J Mol Cell Cardiol* 26: 1307-1320, 1994.
173.   **Meyer M, Schillinger W, Pieske B, Holubarsch C, Heilmann C, Posival H, Kuwajima G, Mikoshiba K, Just H, and Hasenfuss G**. Alterations of sarcoplasmic reticulum proteins in failing human dilated cardiomyopathy. *Circulation* 92: 778-784, 1995.
174.   **Minamisawa S, Hoshijima M, Chu G, Ward CA, Frank K, Gu Y, Martone ME, Wang Y, Ross J, Jr., Kranias EG, Giles WR, and Chien KR**. Chronic phospholamban-sarcoplasmic reticulum calcium ATPase interaction is the critical calcium cycling defect in dilated cardiomyopathy. *Cell* 99: 313-322, 1999.
175.   **Mines GR**. On circulating excitations in heart muscles and their possible relations to tachycardia and fibrillation. 1914.
176.   **Mironov S, Jalife J, and Tolkacheva EG**. Role of conduction velocity restitution and short-term memory in the development of action potential duration alternans in isolated rabbit hearts. *Circulation* 118: 17-25, 2008.
177.   **Mishra S, Gupta RC, Tiwari N, Sharov VG, and Sabbah HN**. Molecular mechanisms of reduced sarcoplasmic reticulum Ca(2+) uptake in human failing left ventricular myocardium. *J Heart Lung Transplant* 21: 366-373, 2002.
178.   **Morad M, and Salama G**. Optical probes of membrane potential in heart muscle. *J Physiol* 292: 267-295, 1979.
179.   **Morgan JM, Cunningham D, and Rowland E**. Dispersion of monophasic action potential duration: demonstrable in humans after premature ventricular extrastimulation but not in steady state. *J Am Coll Cardiol* 19: 1244-1253, 1992.
180.   **Morgan JP**. Abnormal intracellular modulation of calcium as a major cause of cardiac contractile dysfunction. *N Engl J Med* 325: 625-632, 1991.
181.   **Morgan JP**. Abnormal intracellular modulation of calcium as a major cause of cardiac contractile dysfunction. *N Engl J Med* 325: 625-632, 1991.
182.   **Morgan JP, Erny RE, Allen PD, Grossman W, and Gwathmey JK**. Abnormal intracellular calcium handling, a major cause of systolic and diastolic dysfunction in ventricular myocardium from patients with heart failure. *Circulation* 81: III21-32, 1990.
183.   **Movsesian MA, Karimi M, Green K, and Jones LR**. Ca(2+)-transporting ATPase, phospholamban, and calsequestrin levels in nonfailing and failing human myocardium. *Circulation* 90: 653-657, 1994.
184.   **Mulieri LA, Hasenfuss G, Leavitt B, Allen PD, and Alpert NR**. Altered myocardial force-frequency relation in human heart failure. *Circulation* 85: 1743-1750, 1992.
185.   **Munch G, Bolck B, Hoischen S, Brixius K, Bloch W, Reuter H, and Schwinger RH**. Unchanged protein expression of sarcoplasmic reticulum Ca2+-ATPase, phospholamban, and calsequestrin in terminally failing human myocardium. *J Mol Med* 76: 434-441, 1998.
186.   **Munch G, Bolck B, Karczewski P, and Schwinger RH**. Evidence for calcineurin-mediated regulation of SERCA 2a activity in human myocardium. *J Mol Cell Cardiol* 34: 321-334, 2002.

187.   **Nabauer M, Beuckelmann DJ, Uberfuhr P, and Steinbeck G**. Regional differences in current density and rate-dependent properties of the transient outward current in subepicardial and subendocardial myocytes of human left ventricle. *Circulation* 93: 168-177, 1996.

188.   **Nakamura M, Sunagawa M, Kosugi T, and Sperelakis N**. Actin filament disruption inhibits L-type Ca(2+) channel current in cultured vascular smooth muscle cells. *Am J Physiol Cell Physiol* 279: C480-487, 2000.

189.   **Narayan SM, Smith JM, Lindsay BD, Cain ME, and Davila-Roman VG**. Relation of T-wave alternans to regional left ventricular dysfunction and eccentric hypertrophy secondary to coronary heart disease. *Am J Cardiol* 97: 775-780, 2006.

190.   **Nef HM, Mollmann H, Akashi YJ, and Hamm CW**. Mechanisms of stress (Takotsubo) cardiomyopathy. *Nat Rev Cardiol* 7: 187-193, 2010.

191.   **Nemec J, Kim JJ, Gabris B, and Salama G**. Calcium oscillations and T-wave lability precede ventricular arrhythmias in acquired long QT type 2. *Heart rhythm* 7: 1686-1694, 2010.

192.   **Niem W**. Robust and fast modeling of 3D natual objects from multiple views. *Proceedings of SPIE* 2182: 388-397 1994.

193.   **Nolasco JB, and Dahlen RW**. A graphic method for the study of alternation in cardiac action potentials. *J Appl Physiol* 25: 191-196, 1968.

194.   **O'Rourke B, Kass DA, Tomaselli GF, Kaab S, Tunin R, and Marban E**. Mechanisms of altered excitation-contraction coupling in canine tachycardia-induced heart failure, I: experimental studies. *Circ Res* 84: 562-570, 1999.

195.   **Ogawa M, Morita N, Tang L, Karagueuzian HS, Weiss JN, Lin SF, and Chen PS**. Mechanisms of recurrent ventricular fibrillation in a rabbit model of pacing-induced heart failure. *Heart rhythm* 6: 784-792, 2009.

196.   **Ohara T, Ohara K, Cao JM, Lee MH, Fishbein MC, Mandel WJ, Chen PS, and Karagueuzian HS**. Increased wave break during ventricular fibrillation in the epicardial border zone of hearts with healed myocardial infarction. *Circulation* 103: 1465-1472, 2001.

197.   **Ohler A, Weisser-Thomas J, Piacentino V, Houser SR, Tomaselli GF, and O'Rourke B**. Two-photon laser scanning microscopy of the transverse-axial tubule system in ventricular cardiomyocytes from failing and non-failing human hearts. *Cardiol Res Pract* 2009: 802373, 2009.

198.   **Pak PH, Nuss HB, Tunin RS, Kaab S, Tomaselli GF, Marban E, and Kass DA**. Repolarization abnormalities, arrhythmia and sudden death in canine tachycardia-induced cardiomyopathy. *J Am Coll Cardiol* 30: 576-584, 1997.

199.   **Park CJ, Arevalo HJ, and Trayanova NA**. Arrhythmogenesis in Brugada Syndrome: Role of Ventricular Structure. *Biophysical Journal* 100: 435a, 2011.

200.   **Pastore JM, Girouard SD, Laurita KR, Akar FG, and Rosenbaum DS**. Mechanism linking T-wave alternans to the genesis of cardiac fibrillation. *Circulation* 99: 1385-1394, 1999.

201.   **Pastore JM, and Rosenbaum DS**. Role of structural barriers in the mechanism of alternans-induced reentry. *Circ Res* 87: 1157-1163, 2000.

202.   **Peters NS, Green CR, Poole-Wilson PA, and Severs NJ**. Reduced content of connexin43 gap junctions in ventricular myocardium from hypertrophied and ischemic human hearts. *Circulation* 88: 864-875, 1993.

203.   **Piacentino V, 3rd, Weber CR, Chen X, Weisser-Thomas J, Margulies KB, Bers DM, and Houser SR**. Cellular basis of abnormal calcium transients of failing human ventricular myocytes. *Circ Res* 92: 651-658, 2003.

204.   **Piacentino V, 3rd, Weber CR, Chen X, Weisser-Thomas J, Margulies KB, Bers DM, and Houser SR**. Cellular basis of abnormal calcium transients of failing human ventricular myocytes. *Circ Res* 92: 651-658, 2003.

205.   **Pieske B, Kretschmann B, Meyer M, Holubarsch C, Weirich J, Posival H, Minami K, Just H, and Hasenfuss G**. Alterations in intracellular calcium handling associated with the inverse force-frequency relation in human dilated cardiomyopathy. *Circulation* 92: 1169-1178, 1995.

206.   **Pieske B, Kretschmann B, Meyer M, Holubarsch C, Weirich J, Posival H, Minami K, Just H, and Hasenfuss G**. Alterations in intracellular calcium handling associated with the inverse force-frequency relation in human dilated cardiomyopathy. *Circulation* 92: 1169-1178, 1995.

207.   **Pieske B, Maier LS, Bers DM, and Hasenfuss G**. Ca2+ handling and sarcoplasmic reticulum Ca2+ content in isolated failing and nonfailing human myocardium. *Circ Res* 85: 38-46, 1999.

208.   **Pieske B, Maier LS, Piacentino V, 3rd, Weisser J, Hasenfuss G, and Houser S**. Rate dependence of [Na+]i and contractility in nonfailing and failing human myocardium. *Circulation* 106: 447-453, 2002.

209.   **Pinsky DJ, Sciacca RR, and Steinberg JS**. QT dispersion as a marker of risk in patients awaiting heart transplantation. *J Am Coll Cardiol* 29: 1576-1584, 1997.

210.   **Pitt B**. Evaluation of the patient with congestive heart failure and ventricular arrhythmias. *Am J Cardiol* 57: 19B-24B, 1986.

211.   **Prestle J, Dieterich S, Preuss M, Bieligk U, and Hasenfuss G**. Heterogeneous transmural gene expression of calcium-handling proteins and natriuretic peptides in the failing human heart. *Cardiovasc Res* 43: 323-331, 1999.

212.   **Pruvot EJ, Katra RP, Rosenbaum DS, and Laurita KR**. Role of calcium cycling versus restitution in the mechanism of repolarization alternans. *Circ Res* 94: 1083-1090, 2004.

213.   **Qu F, Ripplinger CM, Nikolski VP, Grimm C, and Efimov IR**. Three-dimensional panoramic imaging of cardiac arrhythmias in rabbit heart. *J Biomed Optic* 12: 044019, 2007.

214.   **Qu F, Ripplinger CM, Nikolski VP, Grimm C, and Efimov IR**. Three-dimensional panoramic imaging of cardiac arrhythmias in rabbit heart. *J Biomed Opt* 12: 044019, 2007.

215.   **Qu Z**. Critical mass hypothesis revisited: role of dynamical wave stability in spontaneous termination of cardiac fibrillation. *Am J Physiol Heart Circ Physiol* 290: H255-263, 2006.

216.   **Qu Z, Garfinkel A, Chen PS, and Weiss JN**. Mechanisms of discordant alternans and induction of reentry in simulated cardiac tissue. *Circulation* 102: 1664-1670, 2000.

217.   **Qu Z, Garfinkel A, and Weiss JN**. Vulnerable window for conduction block in a one-dimensional cable of cardiac cells, 1: single extrasystoles. *Biophys J* 91: 793-804, 2006.

218.   **Qu Z, Weiss JN, and Garfinkel A**. Cardiac electrical restitution properties and stability of reentrant spiral waves: a simulation study. *Am J Physiol* 276: H269-283, 1999.

219.   **Reeves JP, Condrescu M, Chernaya G, and Gardner JP**. Na+/Ca2+ antiport in the mammalian heart. *J Exp Biol* 196: 375-388, 1994.

220. **Reiken S, Wehrens XH, Vest JA, Barbone A, Klotz S, Mancini D, Burkhoff D, and Marks AR**. Beta-blockers restore calcium release channel function and improve cardiac muscle performance in human heart failure. *Circulation* 107: 2459-2466, 2003.

221. **Riccio ML, Koller ML, and Gilmour RF, Jr.** Electrical restitution and spatiotemporal organization during ventricular fibrillation. *Circ Res* 84: 955-963, 1999.

222. **Ripplinger CM, Lou Q, Li W, Hadley J, and Efimov IR**. Panoramic imaging reveals basic mechanisms of induction and termination of ventricular tachycardia in rabbit heart with chronic infarction: implications for low-voltage cardioversion. *Heart rhythm* 6: 87-97, 2009.

223. **Rogers JM**. Combined phase singularity and wavefront analysis for optical maps of ventricular fibrillation. *IEEE Trans Biomed Eng* 51: 56-65, 2004.

224. **Rogers JM, Walcott GP, Gladden JD, Melnick SB, and Kay MW**. Panoramic optical mapping reveals continuations epicardial reentry during ventricular fibrillation in the isolated swine heart. *Biophys J* 92: 1090-1095, 2007.

225. **Rubart M, and Zipes DP**. Mechanisms of sudden cardiac death. *J Clin Invest* 115: 2305-2315, 2005.

226. **Sada H, Sada S, and Sperelakis N**. Effects of diacetyl monoxime (DAM) on slow and fast action potentials of young and old embryonic chick hearts and rabbit hearts. *Eur J Pharmacol* 112: 145-152, 1985.

227. **Sasano T, McDonald AD, Kikuchi K, and Donahue JK**. Molecular ablation of ventricular tachycardia after myocardial infarction. *Nat Med* 12: 1256-1258, 2006.

228. **Saumarez RC, Slade AK, Grace AA, Sadoul N, Camm AJ, and McKenna WJ**. The significance of paced electrogram fractionation in hypertrophic cardiomyopathy. A prospective study. *Circulation* 91: 2762-2768, 1995.

229. **Schwinger RH, Bohm M, Schmidt U, Karczewski P, Bavendiek U, Flesch M, Krause EG, and Erdmann E**. Unchanged protein levels of SERCA II and phospholamban but reduced Ca2+ uptake and Ca(2+)-ATPase activity of cardiac sarcoplasmic reticulum from dilated cardiomyopathy patients compared with patients with nonfailing hearts. *Circulation* 92: 3220-3228, 1995.

230. **Schwinger RH, Bohm M, Schmidt U, Karczewski P, Bavendiek U, Flesch M, Krause EG, and Erdmann E**. Unchanged protein levels of SERCA II and phospholamban but reduced Ca2+ uptake and Ca(2+)-ATPase activity of cardiac sarcoplasmic reticulum from dilated cardiomyopathy patients compared with patients with nonfailing hearts. *Circulation* 92: 3220-3228, 1995.

231. **Schwinger RH, Munch G, Bolck B, Karczewski P, Krause EG, and Erdmann E**. Reduced Ca(2+)-sensitivity of SERCA 2a in failing human myocardium due to reduced serin-16 phospholamban phosphorylation. *J Mol Cell Cardiol* 31: 479-491, 1999.

232. **Sen L, Cui G, Fonarow GC, and Laks H**. Differences in mechanisms of SR dysfunction in ischemic vs. idiopathic dilated cardiomyopathy. *Am J Physiol Heart Circ Physiol* 279: H709-718, 2000.

233. **Simonis G, Briem SK, Schoen SP, Bock M, Marquetant R, and Strasser RH**. Protein kinase C in the human heart: differential regulation of the isoforms in aortic stenosis or dilated cardiomyopathy. *Mol Cell Biochem* 305: 103-111, 2007.

234. **Sipido KR, Stankovicova T, Flameng W, Vanhaecke J, and Verdonck F**. Frequency dependence of Ca2+ release from the sarcoplasmic reticulum in human ventricular myocytes from end-stage heart failure. *Cardiovasc Res* 37: 478-488, 1998.

235.   **Sjaastad I, Wasserstrom JA, and Sejersted OM**. Heart failure -- a challenge to our current concepts of excitation-contraction coupling. *J Physiol* 546: 33-47, 2003.
236.   **Sobie EA, Guatimosim S, Song LS, and Lederer WJ**. The challenge of molecular medicine: complexity versus Occam's razor. *J Clin Invest* 111: 801-803, 2003.
237.   **Song LS, Sobie EA, McCulle S, Lederer WJ, Balke CW, and Cheng H**. Orphaned ryanodine receptors in the failing heart. *Proc Natl Acad Sci U S A* 103: 4305-4310, 2006.
238.   **Soo LH, Gray D, and Hampton JR**. Pathological features of witnessed out-of-hospital cardiac arrest presenting with ventricular fibrillation. *Resuscitation* 51: 257-264, 2001.
239.   **Sossalla S, Fluschnik N, Schotola H, Ort KR, Neef S, Schulte T, Wittkopper K, Renner A, Schmitto JD, Gummert J, El-Armouche A, Hasenfuss G, and Maier LS**. Inhibition of elevated Ca2+/calmodulin-dependent protein kinase II improves contractility in human failing myocardium. *Circ Res* 107: 1150-1161, 2010.
240.   **Studer R, Reinecke H, Bilger J, Eschenhagen T, Bohm M, Hasenfuss G, Just H, Holtz J, and Drexler H**. Gene expression of the cardiac Na(+)-Ca2+ exchanger in end-stage human heart failure. *Circ Res* 75: 443-453, 1994.
241.   **Swedberg K, Komajda M, Bohm M, Borer JS, Ford I, Dubost-Brama A, Lerebours G, and Tavazzi L**. Ivabradine and outcomes in chronic heart failure (SHIFT): a randomised placebo-controlled study. *Lancet* 376: 875-885, 2010.
242.   **Tolkacheva EG, Anumonwo JM, and Jalife J**. Action potential duration restitution portraits of mammalian ventricular myocytes: role of calcium current. *Biophys J* 91: 2735-2745, 2006.
243.   **Tomaselli GF, and Marban E**. Electrophysiological remodeling in hypertrophy and heart failure. *Cardiovasc Res* 42: 270-283, 1999.
244.   **Undrovinas AI, Shander GS, and Makielski JC**. Cytoskeleton modulates gating of voltage-dependent sodium channel in heart. *Am J Physiol* 269: H203-214, 1995.
245.   **Vahl CF, Bonz A, Timek T, and Hagl S**. Intracellular calcium transient of working human myocardium of seven patients transplanted for congestive heart failure. *Circ Res* 74: 952-958, 1994.
246.   **Vahl CF, Bonz A, Timek T, and Hagl S**. Intracellular calcium transient of working human myocardium of seven patients transplanted for congestive heart failure. *Circ Res* 74: 952-958, 1994.
247.   **Vanderheyden M, Mullens W, Delrue L, Goethals M, de Bruyne B, Wijns W, Geelen P, Verstreken S, Wellens F, and Bartunek J**. Myocardial gene expression in heart failure patients treated with cardiac resynchronization therapy responders versus nonresponders. *J Am Coll Cardiol* 51: 129-136, 2008.
248.   **Vassallo JA, Cassidy DM, Kindwall KE, Marchlinski FE, and Josephson ME**. Nonuniform recovery of excitability in the left ventricle. *Circulation* 78: 1365-1372, 1988.
249.   **Ventura-Clapier R, Garnier A, and Veksler V**. Energy metabolism in heart failure. *J Physiol* 555: 1-13, 2004.
250.   **Vermeulen JT, McGuire MA, Opthof T, Coronel R, de Bakker JM, Klopping C, and Janse MJ**. Triggered activity and automaticity in ventricular trabeculae of failing human and rabbit hearts. *Cardiovasc Res* 28: 1547-1554, 1994.
251.   **Verrecchia F, and Herve JC**. Reversible blockade of gap junctional communication by 2,3-butanedione monoxime in rat cardiac myocytes. *Am J Physiol* 272: C875-885, 1997.

252.   **Wang J, Liu X, Sentex E, Takeda N, and Dhalla NS**. Increased expression of protein kinase C isoforms in heart failure due to myocardial infarction. *Am J Physiol Heart Circ Physiol* 284: H2277-2287, 2003.

253.   **Wang Y, Cheng J, Joyner RW, Wagner MB, and Hill JA**. Remodeling of early-phase repolarization: a mechanism of abnormal impulse conduction in heart failure. *Circulation* 113: 1849-1856, 2006.

254.   **Wasserstrom JA, Sharma R, Kapur S, Kelly JE, Kadish AH, Balke CW, and Aistrup GL**. Multiple defects in intracellular calcium cycling in whole failing rat heart. *Circ Heart Fail* 2: 223-232, 2009.

255.   **Wasserstrom JA, Sharma R, Kapur S, Kelly JE, Kadish AH, Balke CW, and Aistrup GL**. Multiple defects in intracellular calcium cycling in whole failing rat heart. *Circ Heart Fail* 2: 223-232, 2009.

256.   **Watanabe E, Yasui K, Kamiya K, Yamaguchi T, Sakuma I, Honjo H, Ozaki Y, Morimoto S, Hishida H, and Kodama I**. Upregulation of KCNE1 induces QT interval prolongation in patients with chronic heart failure. *Circ J* 71: 471-478, 2007.

257.   **Watanabe MA, Fenton FH, Evans SJ, Hastings HM, and Karma A**. Mechanisms for discordant alternans. *J Cardiovasc Electrophysiol* 12: 196-206, 2001.

258.   **Watanabe Y, Iwamoto T, Matsuoka I, Ohkubo S, Ono T, Watano T, Shigekawa M, and Kimura J**. Inhibitory effect of 2,3-butanedione monoxime (BDM) on Na(+)/Ca(2+) exchange current in guinea-pig cardiac ventricular myocytes. *Br J Pharmacol* 132: 1317-1325, 2001.

259.   **Weber CR, Piacentino V, 3rd, Houser SR, and Bers DM**. Dynamic regulation of sodium/calcium exchange function in human heart failure. *Circulation* 108: 2224-2229, 2003.

260.   **Wehrens XH, Lehnart SE, Reiken SR, and Marks AR**. Ca2+/calmodulin-dependent protein kinase II phosphorylation regulates the cardiac ryanodine receptor. *Circ Res* 94: e61-70, 2004.

261.   **Wellens HJ, Duren DR, and Lie KI**. Observations on mechanisms of ventricular tachycardia in man. *Circulation* 54: 237-244, 1976.

262.   **Wellens HJ, Lie KI, and Durrer D**. Further observations on ventricular tachycardia as studied by electrical stimulation of the heart. Chronic recurrent ventricular tachycardia and ventricular tachycardia during acute myocardial infarction. *Circulation* 49: 647-653, 1974.

263.   **Wettwer E, Amos GJ, Posival H, and Ravens U**. Transient outward current in human ventricular myocytes of subepicardial and subendocardial origin. *Circ Res* 75: 473-482, 1994.

264.   **Wilson LD, Jeyaraj D, Wan X, Hoeker GS, Said TH, Gittinger M, Laurita KR, and Rosenbaum DS**. Heart failure enhances susceptibility to arrhythmogenic cardiac alternans. *Heart rhythm* 6: 251-259, 2009.

265.   **Wu Y, and Clusin WT**. Calcium transient alternans in blood-perfused ischemic hearts: observations with fluorescent indicator fura red. *Am J Physiol* 273: H2161-2169, 1997.

266.   **Xie Y, Garfinkel A, Weiss JN, and Qu Z**. Cardiac alternans induced by fibroblast-myocyte coupling: mechanistic insights from computational models. *Am J Physiol Heart Circ Physiol* 297: H775-784, 2009.

267.   **Xu KY, Zweier JL, and Becker LC**. Hydroxyl radical inhibits sarcoplasmic reticulum Ca(2+)-ATPase function by direct attack on the ATP binding site. *Circ Res* 80: 76-81, 1997.

268.   **Yano M, Ikeda Y, and Matsuzaki M**. Altered intracellular Ca2+ handling in heart failure. *J Clin Invest* 115: 556-564, 2005.

269.   **Yue DT, Marban E, and Wier WG**. Relationship between force and intracellular [Ca2+] in tetanized mammalian heart muscle. *J Gen Physiol* 87: 223-242, 1986.

270.   **Zabel M, Portnoy S, and Franz MR**. Electrocardiographic indexes of dispersion of ventricular repolarization: an isolated heart validation study. *J Am Coll Cardiol* 25: 746-752, 1995.

271.   **Zhao W, Uehara Y, Chu G, Song Q, Qian J, Young K, and Kranias EG**. Threonine-17 phosphorylation of phospholamban: a key determinant of frequency-dependent increase of cardiac contractility. *J Mol Cell Cardiol* 37: 607-612, 2004.